TECHNISCHE UNIVERSITÄT WIEN

DISSERTATION

Laboratory work on plasma-wall-interaction processes relevant for fusion experiments

Ausgeführt zum Zwecke der Erlangung des akademischen Grades eines Doktors der technischen Wissenschaften unter der Leitung von

Univ.-Prof. Dr. Friedrich Aumayr
E134
Institut für Angewandte Physik

eingereicht an der Technischen Universität Wien
Fakultät für Physik

von

Dipl.-Ing. Bernhard Maximilian Berger
Matrikelnummer.: 0725747
Barichgasse 5a/2, 1030 Wien

Wien, März 2017   (Bernhard M. Berger)

Kurzfassung

Um den Weg für ein zukünftiges Fusionskraftwerk zu ebnen, ist es nicht nur notwendig, Netto-Energie zu produzieren, sondern auch entscheidend, eine erste Wand zu haben, die den hohen Hitzeflüssen und energiereichen Teilchenbeschuss lange genug standhalten, kann um den Fusionsreaktor wirtschaftlich zu betreiben. Daher wurde mit Hilfe einer hochempfindlichen Quarzkristall-Mikrowaagen (QCM) Technik fusionsrelevante Plasma-Wand-Wechselwirkungsprozesse unter kontrollierten Laborbedingungen untersucht.

Eine dieser fusionsrelevanten Projektil-Wandmaterial-Kombinationen, die im Rahmen dieser Arbeit untersucht wurde, ist die Erosion von Wolframnitridschichten (WN) beim Beschuss mit Deuterium-Ionen. Um den Leistungsfluss zum Divertor in einem zukünftigen Fusionsreaktor zu reduzieren, ist die Beigabe strahlender Verunreinigungen in das Plasma erforderlich. Dabei erweist sich Stickstoff (N) als ein sehr wirksames "Kühlmittel" im Bereich des Plasmarands, bei dem jedoch in Kombination mit einem Wolfram-(W)-Divertor, die Bildung von WN Oberflächenschichten beobachtet werden können.

In dieser Arbeit wurde die Erosion von gut vorbereiteten WN- und W-Schichten unter D-Ionen Beschuss bei 500 und $1000\,\text{eV/D}$ untersucht und verglichen. Dabei wurde für W eine konstante Erosionsrate mit zunehmender D-Fluenz gemessen. Hingegen zeigt WN zu Beginn bei niedrigen Fluenzen eine erhöhte Erosionsrate, die sich dann im stationären Zustand dem Wert von reinem W annähert. Vergleiche mit SDTrimSP Simulationen weisen darauf hin, dass diese anfänglich höhere Erosionsrate für WN mit einer erhöhten N-Erosion zusammen hängen könnte. Dazu wurde als möglicher Mechanismus bestrahlungsinduzierte Diffusion in Betracht gezogen.

Eine weitere untersuchte fusionsrelevante Festkörperoberfläche ist Eisen-Wolfram (FeW). FeW ist ein Modellsystem für Stähle wie EUROFER, die schwere Elemente beinhalten und als mögliches Material für abgelegene Bereiche in einem zukünftigen Fusionsreaktor in Betracht gezogen werden. Dazu wurden an dünnen FeW-Schichten mit $1.5\,\text{at\%}$ W fluenzabhängige Zerstäubungsexperiemente unter Beschuss mit D-Ionen bei 250 und $1000\,\text{eV/D}$ durchgeführt. Für den Beschuss bei $250\,\text{eV/D}$ ist zusätzlich der Einfallswinkel des Ionenstrahls gegenüber der Oberfläche variiert worden. Weiters wurde die Topographie und die Rauigkeit der Probe vor und nach der Exposition mit einer Gesamtfluenz von $3 \cdot 10^{23}\,\text{D/m}^2$ untersucht. Für beide kinetischen Energien wurde eine abnehmende Zerstäubungsausbeute mit zunehmen-

der D-Fluenz beobachtet, welche mit einer mit Rutherford-Rückstreu-Spektrometrie (RBS) gemessenen W-Oberflächenanreicherung korreliert. Die anfänglich stärkere Reduktion der Erosionsrate für schrägen Ionenbeschuss verschwindet mit zunehmender Fluenz und erreicht den Wert für normalen Einfall. Dieser Effekt wird mit einer deutlichen Erhöhung der Oberflächenrauhigkeit und (abhängig vom Ionenaufprallwinkel) der Ausbildung von Nanodots oder Rippels in Zusammenhang gebracht.

Zusätzlich zu den Experimenten mit fusionsrelevanten Oberflächen wurde ein neuer experimenteller Aufbau entwickelt, bei dem eine QCM neben dem Probenhalter als Auffänger für das an der Probe zerstäubtes Material diente. Das neue Setup soll dabei Beschränkungen der bestehenden QCM-Technik auf dünne Schichten, welche direkt auf den Quarz aufgebracht werden müssen, überwinden. Nach der Beschreibung wie die Zerstäubungsrate des Ziels aus dem gemessene (Auffänger-) QCM Signal rekonstruiert werden kann, werden Messungen mit einer zweiten (Ziel-) QCM anstelle einer Standard Zerstäubungsprobe durchgeführt, um die prinzipielle Machbarkeit dieser indirekten Zerstäubungsratebestimmung zu beweisen. Die gleichzeitige Verwendung von zwei QCMs erlaubt es, den Massenverlust an der Ziel-QCM (verursacht durch zerstäubte Partikel) und die Massenerhöhung an der Auffänger-QCM (aufgrund der gefangenen Partikel) simultan zu messen und damit die rekonstruierte Zerstäubungsrate mit der direkt gemessenen zu vergleichen. Das Ergebnis dieser Messungen zeigte, dass es möglich ist, mit der neuen Auffänger-Methode absolute Zerstäubungsraten der Probe zu bestimmen.

Abstract

To pave the way towards a future fusion power plant it is not only necessary to produce net energy. It is also crucial to have a first wall that can withstand the high heat fluxes and energetic particle bombardment long enough to operate the fusion reactor economically. Therefore fusion relevant plasma-wall-interaction processes are studied under controlled laboratory conditions using a highly sensitive quartz crystal microbalance (QCM) technique.

One of the fusion relevant projectile-target combinations, investigated within the framework of this thesis, is the erosion of tungsten-nitride (WN) by deuterium (D) ions. In a future fusion device, impurity seeding into the plasma is required to reduce the power flux to the divertor. Nitrogen (N) seeding is an effective coolant at the plasma edge. In combination with a tungsten (W) divertor, the formation of WN surface layers is observed. In this work the erosion of well prepared WN and W (for comparison) films were studied under D ion bombardment at 500 and $1000\,\mathrm{eV/D}$. For W a constant erosion rate was measured with increasing D fluence, while for WN an initially enhanced erosion rate was observed, until steady state conditions are reached where the erosion rate of WN approaches that of pure W. Comparisons to SDTrimSP simulations indicate that this initially higher erosion rate for WN is linked to an enhanced N erosion. As a possible mechanism irradiation-induced diffusion was considered.

Another investigated fusion relevant target surface is iron-tungesten (FeW), because it is a model system for heavy element containing steels, like EUROFER, which are considered as possible material for recessed areas in a future fusion reactor. In particular, fluence dependent sputter experiments were carried out for thin FeW films, containing $1.5\,\mathrm{at\%}$ W, under 250 and $1000\,\mathrm{eV/D}$ ion bombardment. The incident angle of the ion beam was additionally varied for $250\,\mathrm{eV}$ and the sample's topography and roughness was investigated before and after the exposure to a total fluence of $3 \cdot 10^{23}\,\mathrm{D/m^2}$. For both kinetic energies a decreasing sputtering yield with increasing D fluence was observed, which is correlated to a W surface enrichment measured with Rutherford backscattering analysis (RBS). The initially more pronounced reduction of the erosion yield for oblique ion impact, vanishes with increasing fluence and reaches the value for normal incidence. This effect is related to a significant surface roughening and (depending on ion impact angle) formation of nanodots or nano-ripples.

In addition to the experiments on fusion relevant surfaces a new experimental setup was developed, where a QCM is placed beside the target holder acting as a catcher for material that is sputtered at the target surface. The new setup is supposed to overcome the limitations of the existing QCM technique to thin film targets directly deposited on the quartz crystal. After describing how the sputtering yield can be reconstructed from the measured (catcher-)QCM signal, proof of principle measurements using a second (target-)QCM instead of a regular sputter target were conducted. The use of two QCMs allows to measure the mass loss at the target-QCM (caused by sputtered particles) and the mass increase (due to the caught particles) at the catcher-QCM simultaneously and thus to compare the reconstructed target sputtering yield with the directly measured. The result obtained by these measurements demonstrate the feasibility of determining absolute sputtering yield with the new catcher setup.

List of Publications

- **Berger, B. M.**, Stadlmayr, R., Meisl, G., Čekada, M., Eisenmenger-Sittner, C., Schwarz-Selinger, T. and Aumayr, F.
  Transient effects during erosion of WN by deuterium ions studied with the quartz crystal microbalance technique
  Nucl. Instr. Meth. B (**2016**), 382, 82-85, URL `http://dx.doi.org/10.1016/j.nimb.2016.04.060`

- **Berger, B. M.**, Stadlmayr, R., Blöch, D., Gruber, E., Sugiyama, K., Schwarz-Selinger, T. and Aumayr, F.
  Erosion of Fe-W model system under normal and oblige D ion irradiation
  Nuclear Materials and Energy (**2017**), in print, URL `http://dx.doi.org/10.1016/j.nme.2017.03.030`

- **Berger, B. M.**, Szabo, P. S., Stadlmayr, R. and Aumayr, F.
  Sputtering measurements unsing a quartz crystal microbalance as a catcher
  Nucl. Instr. Meth. B (**2017**), in print, URL `http://dx.doi.org/10.1016/j.nimb.2016.11.039`

Conference Participation and Talks

- **Berger, B. M.**
  Impact of Surface Roughness on erosion and retention
  Talk: EUROFusion "Plasma Facing Components" mid-year monitoring meeting, Garching/Germany; 11.10.2016

- Aumayr, F., **Berger, B. M.**, Stadlmayr, R., Blöch, D., Sugiyama, K., Scharz-Selinger, T.
  Sputtering measurements with a new catcher QCM setup
  Poster: 27th International Conference Atomic Collisions in Solids (ICACS 2016), Lanzhou/China; 25.07.2016

- **Berger, B. M.**, Stadlmayr, R.
  Erosion of Fe-W model systems by D ions for different angles of incidence
  Poster: XXII Plasma Surface Interactions in Controlled Fusion Devices (22. PSI), Rome/Italy; 30.05.2016

- **Berger, B. M.**
  Erosion of fusion-relevant wall materials under ion bombardment
  Talk: Seminar - Institut für Allgemeine Physik (IAP), TU Wien; 24.05.2016

- **Berger, B. M.**
  Erosion of Fusion Relevant Surfaces by Ion Impact
  Talk: 2. Fusionstag, TU Wien; 20.11.2015

- **Berger, B. M.**
  Erosion of Fusion-Relevant Wall Materials under Ion Bombardment studied with a Quartz Crystal Microbalance Technique
  Invited talk: 21th International Workshop on Inelastic Ion-Surface Collisions (IISC-21), Donostia-San Sebastián/Spain; 22.10.2015

- **Berger, B. M.**
  Transient mass changes of fusion-relevant materials under ion irradiation, measured with a quartz crystal microbalance
  Talk: Forschungszentrum Jülich, Jülich/Germany; 29.09.2015

- **Berger, B. M.**
  Erosion studies of Fe/FeW and Be/Be+N films under D irradiation
  Talk: EUROFusion "Plasma Facing Components" mid-year monitoring meeting, Garching/Germany; 14.09.2015

- **Berger, B. M.**, Stadlmayr, R., Meisl, G., Čekada, M., Sugiyama, K., Oberkofler, M., Schwarz-Selinger, T., Aumayr, F.
  Transient effects during erosion of WN and FeW films by deuterium ions studied with the quartz crystal microbalance technique
  Poster: 15th International Conference on Plasma-Facing Materials and Components for Fusion Applications (PFMC-15), Aix-en-Provence/France; 18.05.2015 - 22.05.2015

- **Berger, B. M.**, Stadlmayr, R., Aumayr, F.
  Quantification of erosion rates of nitrogen saturated tungsten surfaces under deuterium ion impact
  Poster: Sokendai Asian Winter School 2014, Toki/Japan; 03.12.2014

- **Berger, B. M.**, Dobes, K., Aumayr, F.
  Interaction of deuterium ions with tungsten and nitrogen saturated tungsten surfaces
  Poster: 26th International Conference on Atomic Collisions in Solids (ICACS-26), Debrecen/Hungary; 17.07.2014

- Dobes, K., **Berger, B. M.**, Smejkal, V., Aumayr, F.
  Interaction of nitrogen ions with tungsten and nitrogen saturated tungsten surfaces Poster: Symposium on Surface Science 2014 (3S*14), St. Christoph am Arlberg/A; 12.03.2014; in: "Conference Proceedings 3S*14 Symposium on Surface Science 2014", (2014), S. 95 - 96.

Supervised Students

- **Paul Szabo**
  Development of a Beam Current Monitor
  Bachelor Thesis 2015

- **Reinhard Stadlmayr**
  Setup for High-Fluence Sputter Yield Measurements
  Project Work 2015

- **Reinhard Stadlmayr**
  Erosion of Tungsten-Nitride and Iron-Tungsten under Deuterium Ion Impact
  Diploma Thesis 2016

- **Paul Szabo**
  Sputtering Measurements with a Catcher QCM
  Project Work 2016

- **Daniel Mayer**
  Roughness-Investigation of thin Fe- and Au layers under Ar ion bombardment
  Bachelor Thesis 2016

- **Dominic Blöch**
  Sputter yield measurements with deuterium an iron-tungsten alloys under different angles of incidence
  Project Work 2016

- **Paul Szabo**
  Diploma Thesis in progress

- **Thomas Steiner**
  Duplizierung einer Elektronik für die Quarzkristall-Mikrowaage Bachelor Thesis in progress

Contents

1 **Introduction**

Sputtering due to ion impact represents a very important topic in the field of ion-surface interaction with multiple applications, like thin layer deposition, surface etching or surface analytic techniques. It is also of major concern regarding the erosion of wall material of nuclear fusion devices, or in space weathering where lunar or planetary surfaces get eroded by solar wind ion impact. When energetic particle hit a solid surface a variety of effects occur, like erosion (i.e. sputtering), roughening or smoothing of the surface, changing of the surface composition, reflection or implantation of the projectile, emission of electrons, photons and other secondary particles etc.

Especially with regard to a future fusion power plant the investigation of erosion processes by energetic particles is of great importance. Carefully selected first wall materials facing the ultra hot magnetically confined fusion plasma have to withstand the bombardment with energetic particles in order to be able to operate the reactor in a save and economic way. A large part of the investigations described in this thesis focus on fusion relevant projectile-target combinations. These experiments where carried out under laboratory conditions by the use of a quartz crystal microbalance (QCM) technique. The target layer of interest is deposited onto one side of the quartz crystal and bombarded with a well defined ion beam. The mass change of the target film caused by the ion bombardment is then determined by a measurement of the resonance frequency change of the QCM. The QCM represents an ideal tool, to study these ion surface interaction processes in situ and in real time.

In chapter 2 a brief introduction into nuclear fusion is given highlighting the primary motivation of the research conducted in this thesis, furthermore a short overview on the physics behind the plasma-wall interaction processes in general and sputtering by particle bombardment in particular is included. Chapter 3 introduces the experimental and numerical methods used throughout the thesis and presents a newly developed quartz crystal microbalance catcher setup. In contrast to the existing QCM technique where typically a mass loss of the thin target layer due to the ion bombardment is observed, the QCM in the catcher configuration measures a mass increase. To this purpose a QCM is placed beside the target holder acting as a catcher for sputtered

particles. This configuration has the advantage that sputter experiments are no longer restricted to thin film targets deposited on a QCM. However, data evaluation heavily relies on input from numerical simulations of the sputter process as explained in section 3.3. The results of this thesis are presented and discussed in chapter 4. In the first section the results obtained for fusion relevant projectile-surface combinations are presented while the second section contains the proof of principle measurements, which demonstrate the feasibility of the QCM catcher method.

2 Background

This chapter gives a brief introduction into nuclear fusion and its current status, followed by a short resume on plasma-wall interaction and sputtering by particle bombardment, highlighting the main motivation of the research conducted in this thesis.
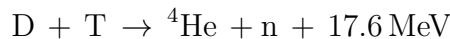
Contents

2.1 Why Fusion Research?

Currently 80% of our energy production is dependent on fast-depleting fossil fuels. Since the global energy consumption as well as the CO_2 emission is steadily increasing, it is crucial to change this dependency. According to a scenario published by the International Energy Agency (IEA) in 2014, we are faced with an increase in the energy demand by 37% until 2040 [1]. In order to satisfy this hunger for energy, renewable energy sources and new concepts for energy production are both required.

While the usage and efficiency of renewable energy sources like solar- or wind power is increasing, there are other new technologies that require further research and development. One very promising technique for energy production would be nuclear fusion. Compared to nuclear fission, where tons of long-lived, highly radioactive waste are produced and the population is faced with the problem of waste storage, nuclear fusion is free of long-lived, radioactive waste [2]. In addition a nuclear disaster like at the Fukushima Daiichi Nuclear Power Plant in 2011 in Japan can not happen with a fusion reactor, since there is no chain reaction involved in a fusion process. The fusion reaction is achieved by getting the fuel hot ($\approx 150,000,000\,°C$) and contained long enough so that the reaction partners can collide often with each other and fuse. At these high temperatures, the electrons are separated from nuclei and the fuel is in an ionized state of matter, a so called plasma. The total amount of fuel needed in the reactor (only a few grams) is added continuously to the reaction, if there is any disturbance the reaction stops automatically [2–4].

In order to make nuclear fusion possible, it is necessary to bring the fusing nuclei sufficiently close (about $10^{-15}\,m$) together so that they can overcome the Coulomb barrier or tunnel through it and to fuse into a nucleus due to the strong interaction force. When light nuclei fuse into a heavier nucleus the mass of the resulting nucleus is smaller than the sum of the initial nuclei. This "mass defect" is transformed into a large amount of kinetic energy, according to Einstein's famous energy-mass relation $E = m \cdot c^2$. One way to bring the fusing particles sufficiently close, is to heat them to very high temperatures[1], as already mentioned above. Figure 2.1, shows the reaction rate for different fusion reactions as a function of the ion temperature. The reaction with the highest fusion efficiency at low temperatures is the deuterium-tritium (D-T) reaction:

$$D + T \rightarrow {}^4He + n + 17.6\,MeV$$

where the two heavier hydrogen isotopes D and T fuse to a helium nucleus and a fast neutron and release a net energy of 17.58 MeV [5].

---

[1]For a Maxwellian particle distribution the mean particle energy W is equal to $(\frac{3}{2}k_B T)$, with the Boltzmann constant k_B. In discussions of fusion reactions it is convenient to speak of temperatures in terms of kilo electron volts (keV). $1\,keV \approx 1.16 \cdot 10^7\,°C$.
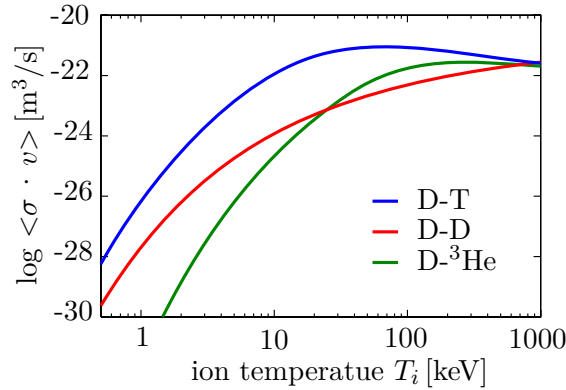
Figure 2.1: Reaction rate coefficient $<\sigma \cdot v>$ as a function of the ion temperature T_i for different fusion reactions. Data taken from [7].

Another great advantage of the D-T reaction for a future nuclear fusion reactor, is the nearly inexhaustible availability of the fuels. The stable hydrogen isotope D occurs with a weight fraction of $3.3 \cdot 10^{-5}$ in water [6]. With the water from the oceans and the current energy consumption, the amount of D available would last for a few billion years. T itself is not directly available since it is an unstable radioactive isotope with a half-life of 12.3 years, but T can be produced directly on-site in transmutation reactions with neutrons from the D-T reaction bombarding a lithium (Li) containing blanket. Ultimately D and Li will be used as fuel for a fusion reactor, where Li is also a very abundant and widespread element in the earth's crust and in the oceans water (average concentration of 0.15 ppm).

In order to produce net energy by fusing light nuclei three conditions must be fulfilled (Lawson criteria). ① A very high plasma temperature T_i to have high energetic collisions, ② a sufficient plasma particle density n_i to increase the possibility that collisions occur and ③ a sufficiently long energy confinement time τ_E of the plasma in order to keep the energy losses low [8]. The currently most promising method to ensure these conditions is magnetically confined fusion, where the fusion plasma (charged particles) is confined by magnetic fields. Two different concepts for generating the magnetic fields have been invented in the '50s, and they are still under investigation worldwide.

The widely-used concept is called tokamak, derived from the Russian words for toroidal chamber with magnetic field. The concept of a tokamak is shown in figure 2.2. A toroidal vacuum vessel is surrounded by toroidal field coils generating a toroidal magnetic field, with a curvature and a gradient in radial direction, resulting in a vertical drift for ions and electrons in the opposite direction. This charge separation causes an electric field, which adds an $E \times B$ drift in outward direction to the charged particles. In order to avoid this charge separation, a twist of the magnetic field lines is
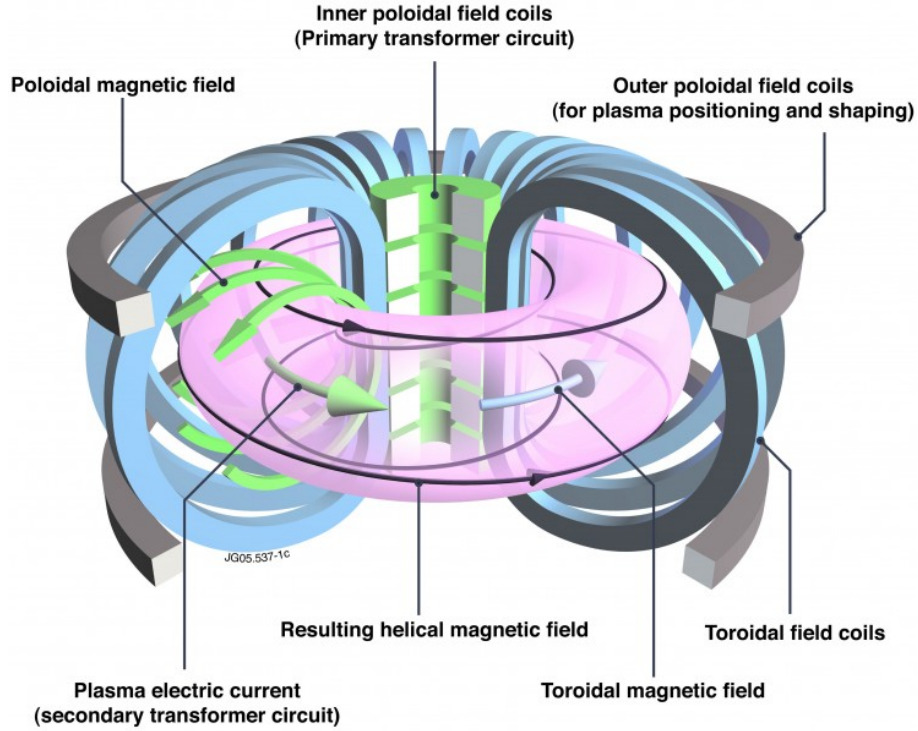
Figure 2.2: Tokamak principle, a helical magnetic field confines the plasma. The field is generated by a combination of toroidal field coils and a poloidal magnetic field due to the toroidal plasma current. The plasma current is induced by the inner poloidal field coils. Figure taken from [3].

necessary by superimposing the toroidal field with an additional poloidal field. This poloidal field is generated by a toroidal current induced in the plasma by the inner poloidal field coils of a transformer [9]. This concept is currently the most advanced and promising one. However, a drawback of this concept is that the tokamak has to be operated in pulsed mode in order to induce the plasma current.

The second concept being pursued is called stellarator, the name is derived form the possibility of harnessing the power source of the sun, a stellar object. Similar to the tokamak the plasma is also confined in a toroidal vacuum vessel surrounded by magnetic field coils. But in contrast to the tokamak design the twist in the magnetic field lines is created by external coils wound around the plasma torus. Also a modular coil design is possible with complex 3-D shaped coils, as shown in figure 2.3. The advantage of this design is that there is no induced plasma current necessary to produce the poloidal magnetic field, with the drawback of a much more complex shape of the magnetic field coils. The currently, largest and most optimized stellarator Wendelstein 7-X (W7-X), has recently (2016) been put into operation by the Max Planck Institute for Plasma Physics (IPP) in Greifswald Germany [10–12].
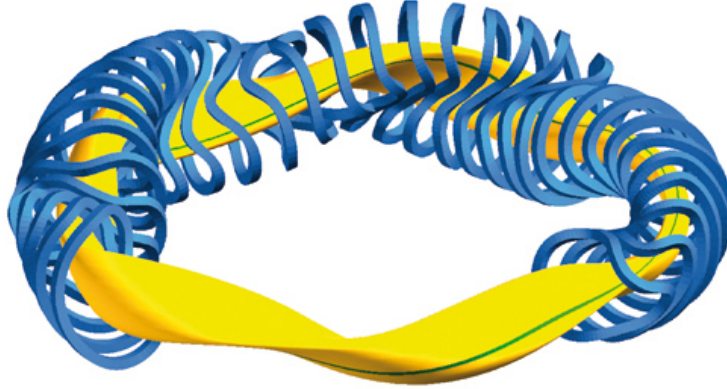
Figure 2.3: Modular design of a stellarator (Wendelstein 7-X). The shape of the plasma (yellow) is governed by an optimized magnetic field, resulting in complex 3-D shaped magnetic coils (blue). Figure taken from [12].

On the way towards a fusion power plant, several experimental fusion reactors are under operation. Most of them are tokamaks, due to the simplicity in the design compared to the stellarator. The largest fusion reactor in Europe is the joint European torus (JET) in Culham, UK. Medium size tokamaks are the axial symmetric divertor experiment upgrade (ASDEX Upgrade) in Garching, Germany and the tungsten (W) environment in steady-state tokamak (WEST) in Cadarache, France.

2.1.1 ITER Project

The world's largest fusion reactor, ITER (cut-away sketch shown in figure 2.4) is currently being built in the south of France [3] by the international thermonuclear experimental reactor (ITER) Members[2] China, the European Union, India, Japan, Korea, Russia and the United States. The aim of this enormous project is to demonstrate the potential and the feasibility of nuclear fusion as an energy source.
The world record for energy production from controlled thermonuclear fusion is held by JET, the currently largest machine operating, with a fusion power of 16 MW, which corresponds to 62% of the input power ($Q = P_{fusion}/P_{input} = 0.62$ [13]). The plasma volume of ITER will be ten times larger than the plasma volume of JET and should be capable of producing 500 MW of fusion power from 50 MW of input power ($Q = 10$). It is not foreseen that ITER will produce any electrical power, but it will

---

[2]representing three continents, over 40 languages, half of the world's population and 85 percent of the global gross domestic product [2].
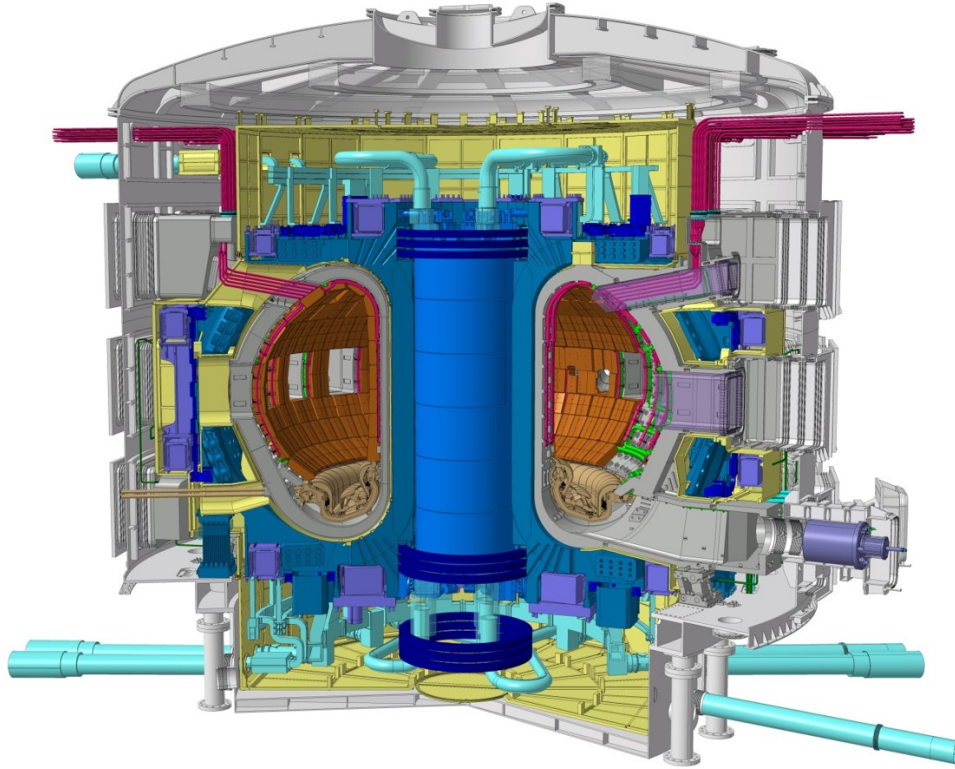
Figure 2.4: Cut-away sketch of ITER, showing the 29 meters high cryostat (outer grey structure), the superconducting magnets (blue) and the vacuum vessel (inner grey structure) with the Be (orange) and W (light brown) first wall. Figure taken from [2].

be the first nuclear fusion reactor producing net energy. The step after ITER on the roadmap to a fusion power plant, will be the DEMOnstration power station (DEMO), which should be the first fusion reactor to produce electrical power to the grid. First conceptional studies for a future fusion power plant expect a net electrical power output of $\approx 1.5\,\text{GW}$ [14]. Depending on the results, achieved by ITER the construction of DEMO is foreseen to start in the 2030s [2].

The main goals of ITER are,

(a) to show the feasibility of producing energy ($Q = 10$) for long pulses ($400\ldots600\,\text{s}$),

(b) to close the gap between the today's smaller-scale experiments and a future fusion power plant,

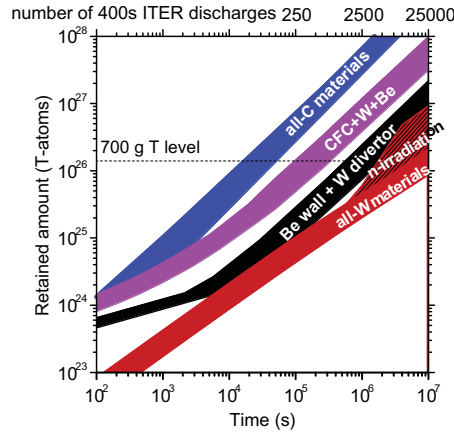(c) to test the technologies needed for heating, plasma diagnostics, control, cryogenics and remote maintenance,

Figure 2.5: T inventory in ITER for different first wall materials. The band width of the different predictions reflects uncertainties in the expected particle flux. Figure taken form [15].

(d) to achieve a D-T plasma where a large part of the required heating is provided by the α-particles from the fusion reaction,

(e) to test the efficiency of the tritium breeding in order to produce the fuel needed on site, (six different breeding concepts will be tested in ITER),

(f) and to demonstrate the safety characteristics of a fusion device [2, 3].

In order to realize this, the selection and design of the plasma facing components (PFCs) are of major concern. As already mentioned above a fusion plasma with a temperature of more than 100 million °C (with a particle density of $\approx 10^{20}$ per m^3 and a confinement time of some seconds) is necessary to realize magnetically confined nuclear fusion [2]. These extreme conditions result in an intense heat and particle flux to the first wall facing the plasma, since the plasma confinement will never be perfect. The lifetime of the PFCs will limit the economics and availability of a future power plant. Therefore it is necessary to avoid high erosion rates or too high heat loads. In addition the selection of the PFC is also crucial for some safety aspects, like the formation of explosive dust or the retention of radioactive T [16]. In the initial design of ITER carbon fiber-reinforced composites (CFC) were a strongly favoured material as PFC since C based materials show an intrinsic impurity level reducing high heat loads at the divertor, by radiation cooling. But in order to full-fill safety and environmental reasons a T limit of 700 g was set for ITER [17], with the consequence that the initially planned divertor made out of CFC (problem with high T retention in hydrocarbon layers) had to be replaced by a full W divertor [18]. The predicted T inventory in ITER for different first wall materials is shown in figure 2.5. It can be seen that the initially planed material choice CFC+W+Be, would reach the T limit within $100 - 300$ full 400 s $Q = 10$ discharges [15].
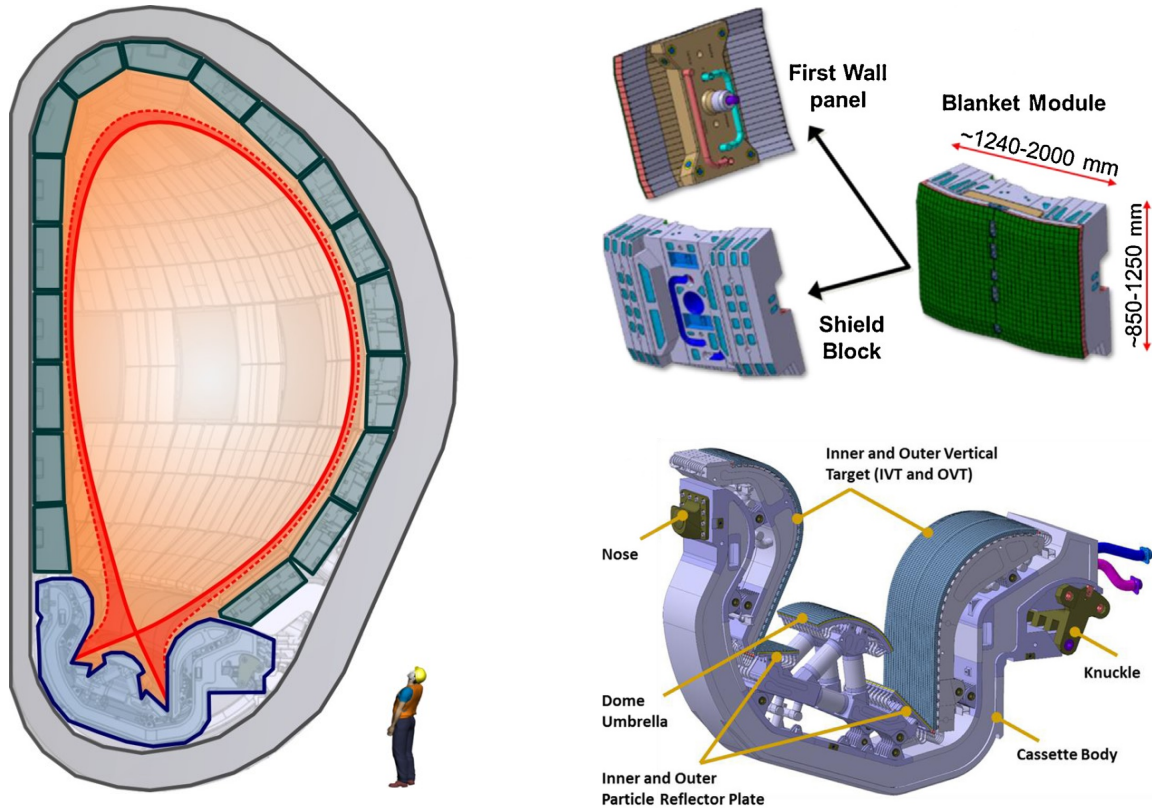
Figure 2.6: left: Cut-away view of the ITER vacuum vessel. Showing the D-T plasma (orange), the blanket modules with the Be first wall panel (green) and the W divertor (blue). Figure taken from [2]; The blanket module consisting of two major components, a plasma facing first wall panel and a shield block. Figure taken from [21]; The divertor provides the main plasma-surface interaction zone, consisting of inner and outer target plates, the dome in the centre and the inner and outer particle reflection plates. Figure taken from [22].

2.2 Plasma Facing Components (PFCs)

In the actual design, the first wall of ITER (facing the hot plasma) will be a full metallic wall consisting of beryllium in the main chamber and a full tungsten divertor [18–20]. Since there is only little experience with these first wall materials, the ITER like wall project at JET for testing the ITER material mix (Be/W) was introduced. Also ASDEX Upgrade is operating with a full W wall to investigate plasma wall interaction (PWI) processes and its implications in an all-W divertor tokamak [19].

A cut-away view of the vacuum vessel of ITER is shown in figure 2.6. The $600\,\text{m}^2$ of the main chamber is covered with 440 so called blanket modules consisting of two major

components, a plasma facing first wall panel and a shield block, shown in figure 2.6 top right. These blanked modules protect the steel structure and the superconducting magnets from the heat and the neutrons produced by the fusion reactions. While the first wall panel has to withstand an incoming heat flux of $1-2\,\mathrm{MW/m^2}$ (selected rows are capable of accommodating up to $5\,\mathrm{MW/m^2}$ during the plasma start up in the limiter configuration) it is the main function of the shield blocks to provide a nuclear shield and to supply the first wall panel with cooling water [23]. Later, in a future fusion power plant the heat caused by the stopping of the neutrons in the shield block will be used for the production of electricity.

The divertor, in the bottom of the vacuum vessel provides the main plasma-surface interaction zone, shown in figure 2.6 bottom right. It will be assembled out of 54 cassettes and is designed to cope with a heat flux of $10\,\mathrm{MW/m^2}$ for steady state and up to $20\,\mathrm{MW/m^2}$ for up to $10\,\mathrm{s}$ [24]. The main function of the divertor is to extract the fusion ash (α-particles) produced by the fusion reactions, to minimize plasma contaminations, and to protect the surrounding walls from the intense heat and neutron loads. The inner and outer target plates will intersect with the magnetic field lines and have to withstand an intense particle bombardment. Therefore the armour of the divertor is made out of W, which is the metal with the highest melting point ($3422\,°\mathrm{C}$) and a very low sputtering yield for D and T ions.

In order not the exceed the heat flux that can be managed by the divertor an active control of the divertor heat flux is necessary. For instance a future fusion reactor will have to emit radiation of several $100\,\mathrm{MW}$ in the plasma edge [25]. This will be achieved by the controlled injection of radiating impurities (noble gases or N - are considered), which spread the power flux onto a larger area of the vessel surface [26]. These impurities emit line radiation while being subsequently ionised to higher charge states. These seeding impurities should be selected in a way that they only radiate in the surface near region to remove unwanted high peak power loads, while core radiation should be avoided in order to have good energy confinement. Figure 2.7 shows the radiative loss factor for different seeding impurities for typical divertor conditions. It can be seen from figure 2.7 that N and Ar are closest to C, which is known as an effective intrinsic coolant in devices with carbon PFCs for T_e below $10\,\mathrm{eV}$ [27, 28]. The general behaviour is that low-Z impurities are best suited for radiative cooling at the plasma edge in the $10\,\mathrm{eV}$ range, while they are fully ionized in the plasma core. Heavier species are more efficient seed species for core radiation, since the cause less fuel dilution [28]. However, excessive core radiation should be generally limited, with regard to energy confinement. Therefore, low W concentrations in the order of 10^{-5} are required in ITER, which make high density divertor operation necessary to confine the impurities in the divertor region [19, 29].
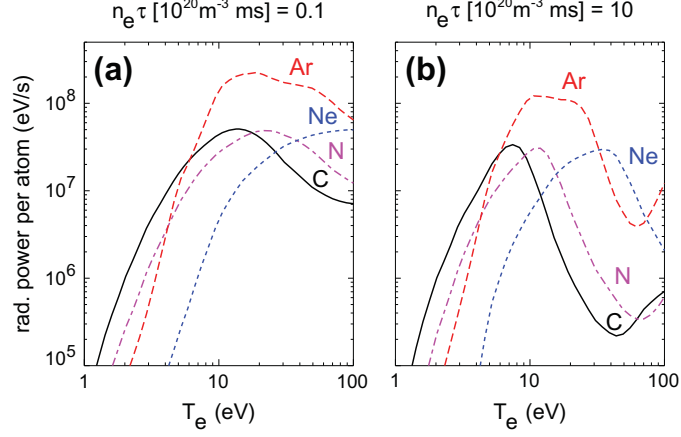
Figure 2.7: Radiative loss factor for different seed impurities for typical divertor conditions. $n_e \cdot \tau = 0.1$ corresponds to typical ASDEX Upgrade conditions, $n_e \cdot \tau = 10$ to high density reactor divertor conditions. Figure taken from [28].
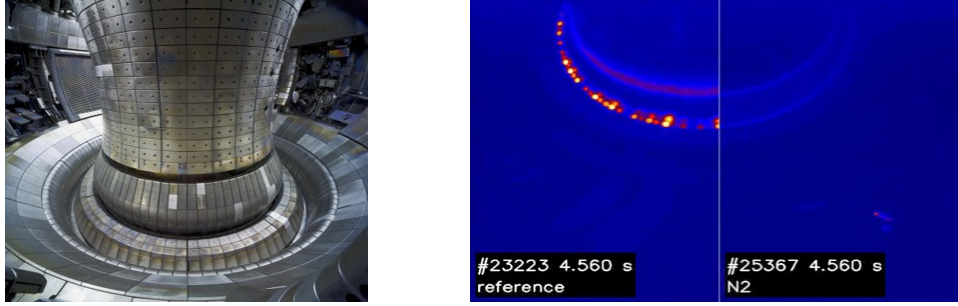

Figure 2.8: Thermographic image of the ASDEX Upgrade interior during a plasma discharge without (left) and with (right) N seeding. Figure taken from [30].

At tokamaks like ASDEX Upgrade or JET with a full metal wall N impurity seeding was able to reduce the power flux to the divertor and to increase the overall plasma performance [30]. Figure 2.8 shows a thermographic image of the ASDEX Upgrade interior during a plasma discharge without (left) and with (right) N seeding. Due to the radiative cooling (N seeding) a reduction of local hot spots can be observed.

However, the use of N as seeding gas for divertor cooling in combination with a W divertor will lead to the formation of tungsten nitride (WN) layers. While the sputtering of W and WN is well investigated and processes like N retention, N codeposition or the implantation of N are well described [31–33], little is known about the interaction of WN with D plasmas. This represents the main motivation for the performed measurements with D ions bombarding WN films, presented in section 4.1.
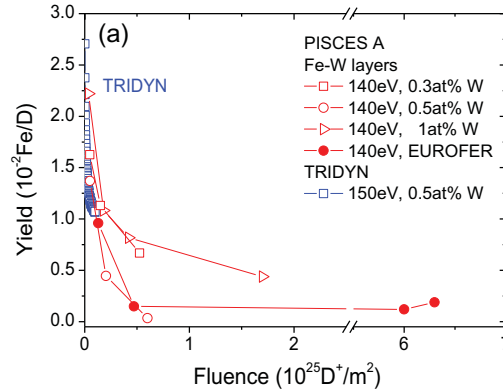
Figure 2.9: Sputtering yield of EUROFER (solid points) and FeW layers with different W concentrations (open points) as a function of the D fluence (provided by a D linear plasma column with a bias voltage of $-150\,\mathrm{V}$). Figure taken from [37].

The first wall selection for DEMO or a future commercial fusion power might be different than in ITER or currently operating tokamaks which have to face transient power loads due to ELMs (edge localised mode) or plasma disruptions [16]. For a future fusion power reactor a stable and quiescent plasma is presumed, where the lifetime of the PFCs will be dominated by plasma induced erosion due to sputtering. The erosion of high-Z materials is considerably lower than the erosion of low-Z materials at the expected low ion energies in the near surface region [34]. Therefore the use of thin W armours as PFCs is foreseen in some DEMO design studies [34, 35]. In addition, the steady-state operation brings new demands to the heat removal from the PFC. A directly bonding of the armour to the cooled component is necessary which is expensive and technologically challenging. One attractive alternative to a full tungsten armour for recessed areas would be the use of W containing steels (e.g. EUROFER [36]). For EUROFER a strong decrease in the sputtering yield for low energetic D plasma bombardment is observed with fluence, as shown in figure 2.9. Also a tungsten surface enrichment is observed due to preferential sputtering of the lighter elements and correlates with the change of the erosion yield [37, 38]. A profound understanding of these W surface enrichment process due to the interaction of D ions with W-containing steels is hence highly desirable and the motivation for the investigations under laboratory conditions using a D ion beam and well defined FeW model films presented in section 4.2.1.

2.2.1 Sputtering

The ejection of target atoms from a surface due to the impact of energetic particles is called sputtering. The sputtering yield Y is defined as, the mean number of emitted
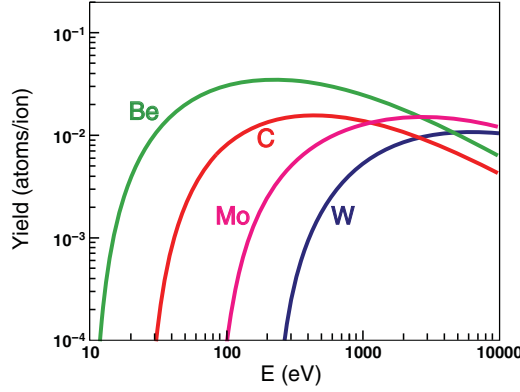
Figure 2.10: Different physical sputtering yields for fusion relevant surfaces under D ion impact. Figure adapted from [47].

atoms per impinging particle and can be influenced by a large number of parameters like the kinetic or potential particle energy, the mass of the projectile and the target atoms, the angle of incidence, the chemical environment or the surface structure (roughness). Depending on the projectile-target combination, the surface erosion process can also be dominated by chemical reactions between the impinging particle and the target surface, called chemical sputtering. Chemical effects can increase the surface erosion rates, which is for example the case for the erosion of the C surface by H isotopes. Especially for low ion energies and elevated temperatures, the erosion is dominated by the formation of CH_3 radicals and other higher order hydrocarbons [39–41]. For some materials, typically insulating or semi-conducting materials, also the charge state of the impinging ion can influence the sputtering yield. This behaviour is commonly called potential sputtering [42, 43]. A multiply charged ion, which impinges on a surface, is generally neutralized. This neutralization process starts already before the ion penetrates the target. Target electrons are captured quasi-resonantly in highly excited projectile states while some inner shells remain transiently empty. The so-formed hollow atom begins then to decay by a series of de-excitation processes, whereby a large part of the potential energy is deposited in a short time (typically $100\,\text{fs}$) within a small area (typically less than $1\,\text{nm}^2$). The potential energy of the projectile may be released via electronic excitations of the target and the ejection of electrons and x rays. For insulating or semi-conducting targets where such sudden perturbations of the electronic structure cannot be rapidly accommodated (like in metals) this can lead to the ejection of target atoms [42, 44–46].

For the metallic target materials studied throughout this thesis, the dominant sputtering process is physical sputtering. The process of physical sputtering, where kinetic energy/momentum is transferred from the projectile to the target atom is theoretically
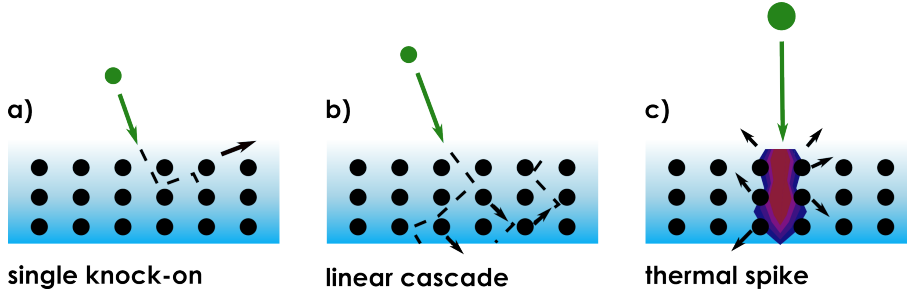
Figure 2.11: Different collision regimes depending on the projectiles size and kinetic energy . Figure taken from [53].

well understood and described [48–51]. The projectile's momentum is transferred in a series of elastic collisions to the target atoms in which the projectile is deflected by the screened Coulomb potential of the target atom. In addition electronic excitations can be induced by inelastic electronic collisions. The recoiling target atoms collide with further target atoms transferring energy and angular deflections and creating a so called collision cascade. An atom close enough to the surface is sputtered if the energy (actually the component normal to the surface) transferred to it is sufficient to overcome the surface binding energy *sbe*. Depending on the ion-target combination a certain threshold energy E_{th} (typically in the range of a few eV up to 400 eV) has to be reached in order to have a sputtering process. This can be analytically approximated by [52]:

$$E_{th} = \frac{(m_1 + m_2)^4}{4m_1 m_2 (m_1 - m_2)^2} sbe \tag{2.1}$$

where m_1, m_2 is the mass of the projectile and the target atom respectively. For projectile energies below this threshold no sputtering takes place. With increasing energy the penetration depth of the projectiles as well as the sputter rate increases until reaching a broad maximum at some 100 eV, as shown in figure 2.10 for some fusion relevant surfaces under D ion impact. At even greater energies, the sputtering yield and the energy transmitted to the surface decreases in conformity with the cross section for nuclear collisions.

Depending on the primary ion energy and the mass ratio between the target and the projectile three different types of collision cascades are formed, shown in figure 2.11. The single knock-on regime (figure 2.11, a) occurs when light or low energetic projectiles hit the target. The energy transferred is too low to initiate a collision cascade. Single collisions between two collision partners can lead to the sputtering of a near surface atoms. The sputtering rate in the single knock-on regime is proportional to the impact cross-section.
The linear collision cascade (figure 2.11, b) takes place at moderate ion energies from eV up to MeV. The energy transferred is high enough to produce higher order recoils.
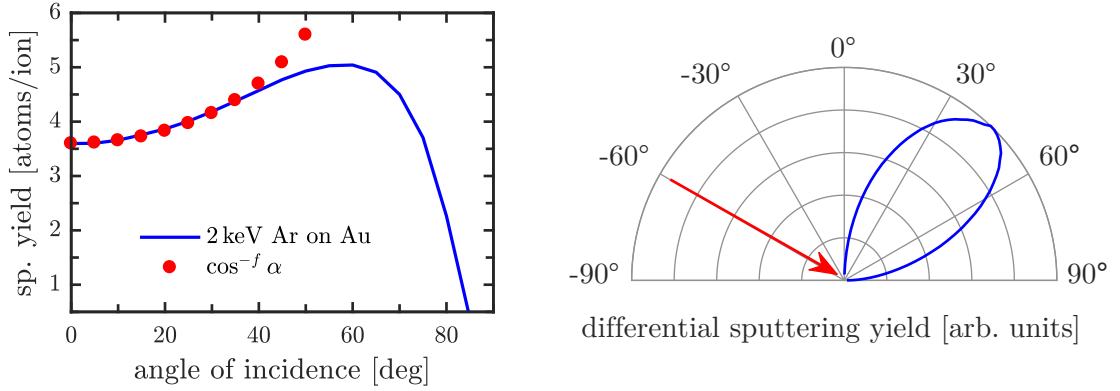
Figure 2.12: (left) SDTrimSP simulation of the Au sputtering yield under 2 keV Ar ion impact for different impact angles α (counted from the surface normal). (right) Polar distribution of the sputtered Au atoms, simulated with SDTrimSP. The red arrow indicates the incidence direction ($\alpha = 60°$) of the 2 keV Ar ion beam.

The collision cascade can be understood as a series of binary collisions (two body collisions). Some of the atoms near to the surface which have received sufficient energy to overcome the surface binding energy can leave the target. The sputtering rate is proportional to the energy deposition per depth unit.

Non-linear collision cascades (thermal spike) (figure 2.11, c) occur with the impact of molecules, clusters and swift heavy ions. The collision cascade here is so tight that all the atoms within a certain volume are set in motion. The sputtering rate is proportional to the energy deposition per unit volume.

For projectile energies in the MeV range additional electronic sputtering contributes to surface erosion. A large part of the impinging ions energy is transferred to the electrons along the ion track. Coupling between the electrons and the phonons result in a large local heating in a cylindrical volume. This leads to temperatures exceeding the melting temperature and surface atoms can be removed by evaporation of material.

2.2.2 Angular Dependence and Surface Roughness

Generally, in a nuclear fusion device the particles will not hit the surface under normal incidence, since the ions full fill a gyromotion around the magnetic field lines intersecting with the first wall at small angles. In addition the plasma facing components of the first wall of a fusion device are technically rough surfaces due to their manufacturing process and the plasma exposure.

Experimental and theoretical analysis of the sputtering process show a dependence of the sputtering yield, with the angle of incidence α (counted from the target surface normal) [48, 54]. This angular dependency is more pronounced for flat (polished) surfaces than for rough ones where generally a higher sputtering yield is measured at normal incidence. For impact angles of about 45° approximately the same value is measured for rough and flat surfaces [55, 56]. For small impact angles and flat surfaces this angular dependency can be described by a $\cos^{-f} \alpha$ behaviour, where f is a function of the ratio between the target and projectile mass. Also the sputtering yields and angular distributions of the sputtered and reflected particles simulated with programs like SDTrimSP are in a good agreement with the experimental data obtained for well polished surfaces.

In figure 2.12 the results obtained with the simulation program SDTrimSP for 2 keV Ar ions hitting a polycrystalline Au target are presented. The left figure shows the angular dependence of the sputtering yield. For low impact angles a $\cos^{-f} \alpha$ behaviour of the sputtering yield can be seen up to a maximum where the repulsive action of the surface atoms becomes strong enough to prevent the ions from penetrating into the target, resulting in a decreasing sputtering yield which approaches zero for $\alpha = 90°$ [48]. The polar distribution of sputtered Au particles is shown in the right figure, for a 2 keV Ar beam (red arrow) hitting the surface under $\alpha = 60°$. While the distribution of the sputtered particles for normal incidence (for amorphous and polycrystalline materials) can be described in a first approximation by a cosine distribution [57], the distribution for oblique ion impact often peaks at or near the specular direction [58].

However, with increasing surface roughness the experimental and simulated results differ increasingly. In addition the roughness of a surface is in general not constant during ion bombardment and will change with the ion fluence depending on the ion species, kinetic energy and the angle of incidence until a steady state condition is reached. Investigations by Küstner et al. showed that the distribution of the local angle of incidence is of major concern in order to describe the sputtering of rough surfaces [55, 56]. Figure 2.13 (left) shows the sputter geometry of a rough target surface. For a rough target surface, the local impact angle σ (angle between the local surface normal and the ion beam), generally differs from the nominal angle of ion incidence α (angle between the target normal and the ion beam). This results in a distribution of local impact angles which influences the total sputtering yield of the target.

It can also be seen that shadowing effects may occur for $\alpha \neq 0°$, resulting in some areas which are not hit at all by the ion beam. The second effect that has to be taken into account for rough surfaces is the redeposition of sputtered particles, schematically shown in figure 2.13 (right). The sputtered target atoms are emitted in a first approximation in form of a cosine distribution at the point P and leave the surface in
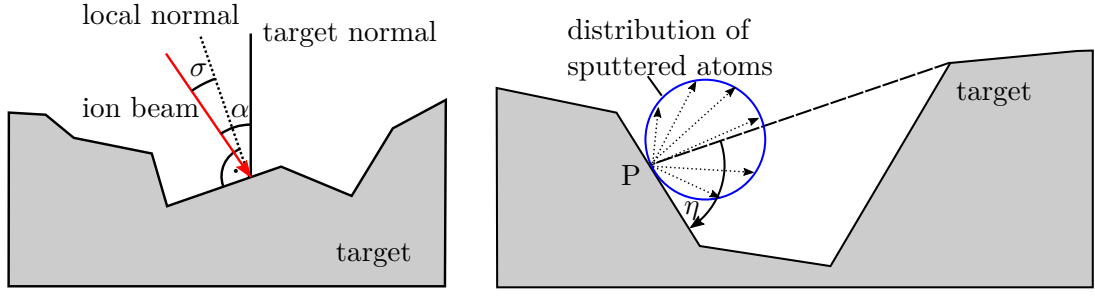
Figure 2.13: (left) The ion beam hits the target under the nominal angle of incidence α, the local angle of incidence σ usually differs from α for a rough surface. (right) sputtered target atoms emitted in a (cosine) distribution at the point P leave the surface. Depending on the local geometry, some of the sputtered atoms are redeposited on the surface nearby. The dashed line under the angle η between P and the edge cuts off a segment of the distribution which cannot leave the surface directly. Figure inspired by [55].

straight lines [48,52]. Depending on the local geometry, some trajectories of sputtered particles intersect with the surface nearby. The dashed line under the angle η between the point P and the edge cuts off a segment of the distribution which cannot leave the surface directly. The volume of this segment of the distribution divided by the volume of the whole distribution gives the redeposition fraction $R(\sigma)$. The particles intersecting with the surface stick there with a sticking probability C_{st}, which is for example for Au approximately 1 [59,60]. While sputtering by reflected particles has to be taken into account, further sputtering by sputtered particles can be neglected due to their low kinetic energy for certain projectile-target combinations [48,55,56,61].

2.2.3 Mixed Material Layers

For targets consisting of two ore more atomic species sputtering can become more complex, since the momentum transferred to the respective target species is different. This is not only the case for target materials which originally consist of several components, but also for pure elemental targets where projectiles are implanted and trapped. Also the surface binding energy for the individual target components as well as for the mixed material can be different from the pure elements. The different momentum transfer as well as the difference in the surface binding energy leads to preferential sputtering of a certain target component. Resulting in a change of the elemental target composition within the projectile range and a change in the partial sputtering yields Y_i and reflection coefficient with the ion fluence. Due to preferential sputtering typically one target species is depleted with increasing ion fluence until a steady state condition is reached where the target is sputtered stoichiometrically [57].

<div align="right">

3 Methods

</div>

This chapter introduces the experimental and numerical methods used throughout the thesis. Parts of the experimental setup designed for the irradiation of the fusion relevant surfaces have been published in [62] while parts of the newly developed quartz crystal microbalance catcher configuration have been published in [63].
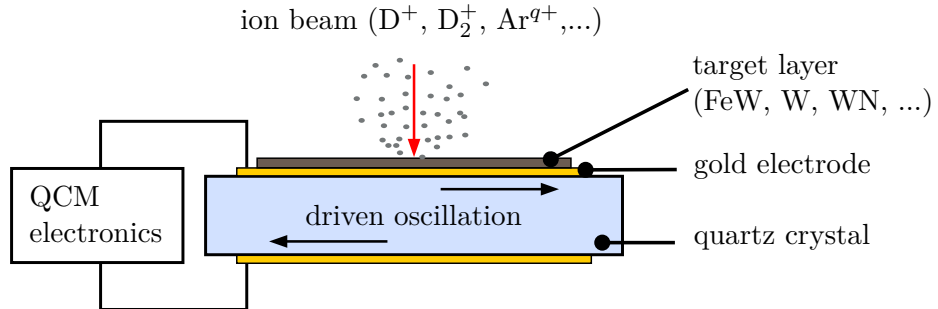
Contents

Table 3.1: Materials constants for the used SD-cut quartz crystal, taken from references [67, 68]

symbol	value	description
n	1	number of overtone
$C1$	$3.7\,[\text{fF}]$	motional capacitance for C-mode [68]
ϵ_{22}	$3.98 \cdot 10^{-11}\ [\text{Fm}^{-1}]$	dielectric constant for SC-quartz [68]
kp^2	0.0024	piezo electric coupling factor for C-mode [68]
d_Q	$0.302 \cdot 10^{-3}\,[\text{m}]$	quartz thickness [67]
ρ_Q	$2649\,[\text{kg/m}^3]$	quartz mass density [68]

3.1 Quartz Crystal Microbalance (QCM) Technique

Since the bombardment of a target with energetic particles is usually accompanied with small mass changes a quartz crystal microbalance (QCM) is an ideal tool to measure this in situ and in real time. In particular, a QCM technique, developed and optimised at the TU Wien [64–66], is used to determine the small mass change due to sputtered particles and/or implanted projectiles when the target layer is hit with energetic ions. A 6 MHz SC-cut plano-convex ($r = 300\,\text{mm}$) quartz crystal with a diameter of 14 mm is used. The quartz crystal is available from KVG Quartz Crystal Technology GmbH, Germany [67]. The material constants of the used quartz crystal are listed in table 3.1. The use of a stress compensated (SC) quartz crystal instead of the commonly used AT-cut has the advantage that the resonance frequency of the SC-cut quartz crystal is less sensitive to radial stress, caused by the ion bombardment or by mounting the quartz in the sample holder. Figure 3.1 shows the schematics of the QCM technique.

Figure 3.1: Schematics of the QCM technique. A thin target layer is directly deposited onto a gold electrode of the quartz crystal, which is then irradiated with ions. The quartz crystal is connected to the QCM electronics via the gold electrodes and operated in a driven thickness shear mode.

The quartz crystal is connected via the (140 nm thick) gold electrodes to the QCM electronics, which operates the quartz crystal in a driven thickness shear mode. This thickness shear mode represents a standing transversal wave. In the fundamental oscillation, the thickness of quartz d_Q is equal to half a wavelength and the resulting eigenfrequency can be written as [69]:

$$f = \frac{v_{tr}}{2 \cdot d_Q} \tag{3.1}$$

where v_{tr} is the phase velocity of the transversal wave. The target layer of interest is deposited on top of one of the gold electrodes, shown as black target layer in figure 3.1. If the foreign layer applied to the quartz is sufficiently thin, the resonance frequency of the quartz crystal is affected in the same way as a quartz layer of the same mass would. Assuming that the thickness/mass change of the target layer is homogeneous due to the ion bombardment. The relation between a relative mass change $\Delta m_Q/m_Q$ and a relative frequency change $\Delta f/f$ of the QCM can be described by using the Sauerbrey equation [69]:

$$\frac{\Delta f}{f} = -\frac{\Delta d_Q}{d_Q} = -\frac{\Delta m_Q}{m_Q} \tag{3.2}$$

By measuring the relative frequency change $\Delta f/f$, the mass change per unit area of the QCM can be determined directly by using the Sauerbrey equation 3.2:

$$\Delta m_Q \,[\text{amu/cm}^2] = -\frac{\rho_Q \cdot d_Q}{m_n} \cdot \frac{\Delta f}{f} \tag{3.3}$$

with m_n being the atomic mass unit and ρ_Q the mass density of the quartz crystal. With knowledge of the incident ion current per unit area I/A (measured with a Faraday cup with aperture opening area A) integrated over a measuring time Δt, the average mass change per impinging ion can be calculated as follows [64]:

$$y \,[\text{amu/ion}] = \frac{\rho_Q \cdot d_Q}{m_n} \frac{e_0 \cdot q \cdot A}{I \cdot f} \cdot \frac{\Delta f}{\Delta t} \tag{3.4}$$

with e_0 being the electron charge, q the charge state of the impacting ions. The total sputtering yield Y in sputtered atoms per impinging ion is then the average mass change per ion divided by the sputtered target particle mass m_t:

$$Y\,[\text{atoms/ion}] = \frac{y}{m_t} \qquad (3.5)$$

The QCM technique always determines the total mass change and does not give any information about the sputtered species. This means that the use of equation 3.5 implies that the mass increase due to the implantation of ions hitting the target layer can be neglected. Or a steady state condition is reached, where an equilibrium between re-sputtered and freshly implanted projectiles is realized. The fluence necessary for reaching steady state depends on the kinetic energy of the projectile as well as on the projectile target combination [64]. For targets consisting of several components, the ion bombardment may lead to a change in stoichiometry and the actual sputtered-target particle mass m_t is unknown. In this case, instead of the sputtering yield Y in atoms per impinging ion the mass removal rate y (equation 3.4) is used.

3.1.1 QCM Target Holder

To mount the QCM inside an ultra high vacuum chamber a specially designed QCM target holder is used. The concept of the target holder is based on an existing one [70], with some improvements to make angular dependent sputtering experiments possible. The target holder is now modularly constructed and consists of a Faraday cup for ion current density measurements and a quartz crystal holder, shown in figure 3.2. In order to be easily mounted inside the vacuum chamber the existing dovetail connection to the manipulator rod is used. The manipulator allows a positioning of the target holder in the spatial directions x, y, z and a rotation ϕ of the manipulator rod. To allow sputtering experiments under oblique ion impact (up to 70° from the surface normal) without having any shadowing problems, the quartz crystal is positioned directly behind the front plate of the quartz crystal holder. In addition, the quartz crystal is located on the rotation axis of the target holder which simplifies angle-resolved measurements. The exploded view in figure 3.2 shows the quartz crystal holder in detail. The quartz crystal (figure 3.2 ③) is clamped between the sample holder main part (figure 3.2 ①) and a tungsten spring (figure 3.2 ④). A thin gold ring (figure 3.2 ②) between the quartz and the sample holder main part is used to reduce mechanical stress caused by the clamping. In addition, to control the temperature of the QCM, the sample holder main part is equipped with a coaxial heating wire, red part in figure 3.2. For measuring the temperature a K-type thermocouple is used. The thermocouple is directly clamped with one of the screws used for fixing the quartz crystal holder at the target holder.

connection to
manipulator with
dovetail

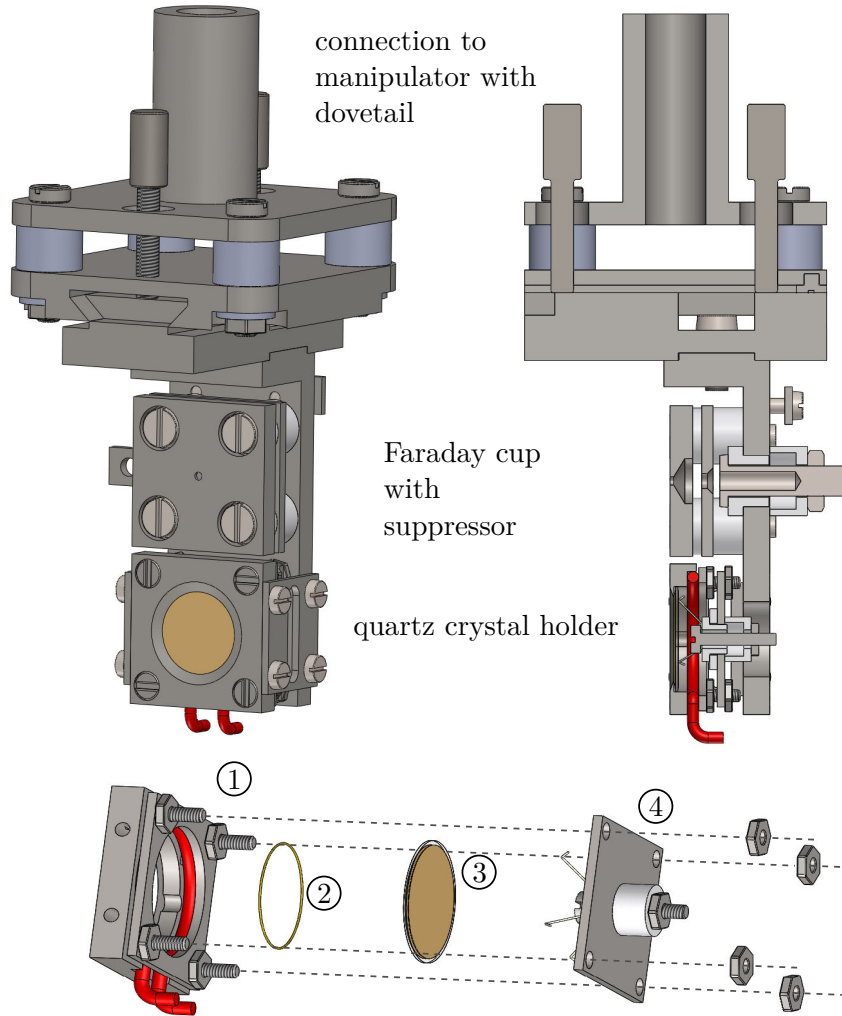Faraday cup
with
suppressor

quartz crystal holder

Figure 3.2: CAD model of the modular constructed QCM target holder, consisting
of a Faraday cup and a quartz crystal holder. The exploded view shows the quartz
crystal holder including the main part (1), the gold ring (2), the quartz crystal (3)
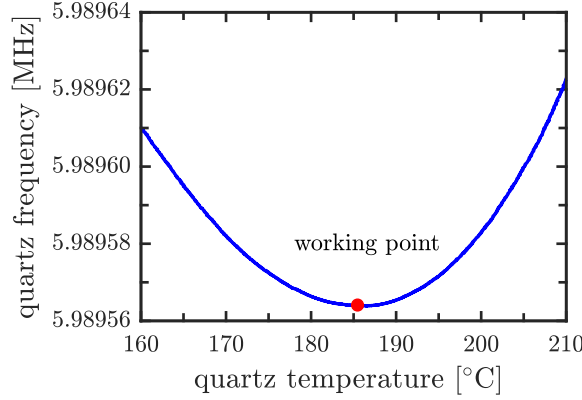and the tungsten spring (4) in detail.

Figure 3.3: Frequency over temperature behaviour of the QCM. The ideal working point, where small temperature changes hardly affect the resonance frequency, is marked with a red dot.

3.1.2 Temperature Dependence and Sensitivity of the QCM

The resonance frequency of the quartz depends not only on the layer thickness, but also on the quartz temperature. The frequency-temperature behaviour of the used SC-cut quartz can be described with a 3rd order parabola [67] with a minimum between 180 °C and 190 °C. Figure 3.3 shows the measured temperature dependence of the quartz crystal. To minimise the influence of temperature variations on the resonance frequency (e.g. caused by the energy of the impinging ions), the QCM can be operated at a working point at the minimum of the frequency-temperature curve. At this point, a temperature change caused by the ion bombardment is typically below any detectable limit and can be neglected. To keep the temperature stable ($\pm\ 0.1$ °C) at the desired working point it proved to be sufficient to operate the coaxial heater with a constant current source.

As mentioned in section 3.1, the use of the Sauerbrey equation 3.2 presupposes a homogeneous mass change of the target layer. If the mass change of the foreign layer does not cover the entire oscillating surface of the crystal then the occurring frequency change is smaller than by equation 3.2 described [69]. In order to ensure a homogeneous mass change of the target layer, the ion beam is scanned by using two sets of scanning plates. These scanning plates are operated with two different zigzag voltages at 50 Hz and 1.6 kHz and scan the ion beam over the whole oscillating quartz crystal area. Thereby it is assured that the variation of the ion current density is kept below $\approx\ 10\ \%$ across the oscillating surface of the quartz crystal, by adjusting the scanning voltage. The actual size of the irradiated area and the incident ion current density is determined with the Faraday cup also located at the QCM target holder. In
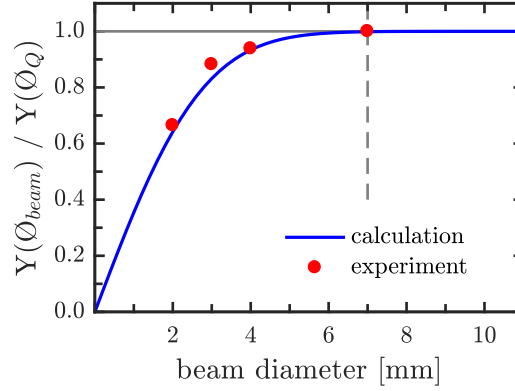
Figure 3.4: Ratio between the sputtering yield of a reduced beam diameter ($Y(\varnothing_{beam})$) and the sputtering yield obtained with an ion beam hitting the entire quartz surface ($Y(\varnothing_Q)$).

order to measure the ion current profile the Faraday cup is moved step-wise through the scanned beam in both transverse directions.

Figure 3.4 shows the ratio of the determined sputtering yield for a reduced ion beam diameter $Y(\varnothing_{beam})$ compared to the yield $Y(\varnothing_Q)$ obtained with an ion beam hitting the entire quartz surface. The red data points were determined by cutting the scanned ion beam with a set different apertures ($\varnothing = 2$, 3, 4 and 7 mm). To calculate the sensitivity of the QCM (figure 3.4, blue curve) the amplitude function $a(x, y)$ for a unloaded planoconvex quartz crystal is used [71]:

$$a(x,y) = e^{-\alpha_n x^2/2} e^{-\beta_n y^2/2} \tag{3.6}$$

where x and y are in-plane coordinates of the quartz crystal and α_n and β_n constants depending on elastic and geometric properties of the quartz as-well as on the number of overtone n. The formula for the motional capacitance of a planoconvex quartz crystal with full size electrodes is used to determine α_n and β_n [71]:

$$C1 = \frac{32\epsilon_{22} \cdot kp^2}{n^2 \pi d_Q \sqrt{\alpha_n \cdot \beta_n}} \tag{3.7}$$

with $C1$ being the motional capacitance, the dielectric constant ϵ_{22} and the piezo electric coupling factor kp^2. With this, the material parameter from table 3.1 and the ratio of $\alpha_n/\beta_n \approx 0.8$ (taken from reference [72], figure 3), the amplitude $a(x, y)$ of the quartz crystal can be calculated. The sensitivity $s(x, y)$ is then proportional to the square of the vibrational amplitude $a(x, y)$ [73]. This relation allows the QCM also to be used as a catcher for sputtered material where the mass change is not uniform, described in section 3.3. It can be seen in figure 3.4, that the experimentally obtained

sensitivity is in a very good agreement with the calculated data. For an ion beam diameter $\varnothing \geq 7\,\mathrm{mm}$, no change in the sensitivity is visible, which makes it sufficient to scan the ion beam $7 \times 7\,\mathrm{mm}$ to fulfil the Sauerbrey equation and to calculate the sputtering yield by the use of equation 3.4 respectively 3.5. Additionally it shows that the clamping of the quartz at its edge does not affect the resonance frequency.

3.1.3 Measurement Procedure

To determine the sputtering yield by using the QCM technique, first the ion current density is measured as described in section 3.1.2. Since the ion current cannot be measured simultaneously during the irradiation of the QCM target layer, it is important that the ion source supplies a constant current. In order to compensate small ion current fluctuations of the source, a second beam profile is measured after the irradiation of the QCM. The averaged ion current density of the two measured beam profiles is then used to calculate the sputtering yield. A typical QCM measurement is shown in figure 3.5. The measurement starts with a beam off phase where the ion beam is interrupted with a shutter in the beam path. During this beam off phase the correct operation of the QCM and the frequency drift of the quartz crystal is measured. This is followed by a homogeneous ion bombardment of the QCM target layer. At the end of the measurement the drift and the correct operation of the QCM is measured again. For measurements with a rather low total ion fluence, the target layer thickness can be considered as constant and the resulting constant frequency change is linearly fitted. The mass change per impinging ion is then evaluated by taking equation 3.4, the slope $\Delta f/\Delta t$ of the linear fit and the measured ion current density. Additionally to increase the accuracy of the QCM method the averaged quartz drift measured during the beam off phases can be subtracted from the frequency change during the ion irradiation. This method is only applicable for target surfaces which are not subjected to mass changes after the ion bombardment, like surface oxidation or outgassing of implanted projectiles. For measurements where the mass change is not constant during the measurement the derivative df/dt of the frequency vs time curve is used instead of the slope $\Delta f/\Delta t$ of the linear fit. Since the measured frequency curve is noisy, a smoothing of the curve with a Savitzky–Golay filter is necessary before calculating the derivative.

3.1.4 Accuracy and Limits

The accuracy of a mass change obtained by using the QCM technique depends on two crucial measured quantities, the ion current density and the frequency change.
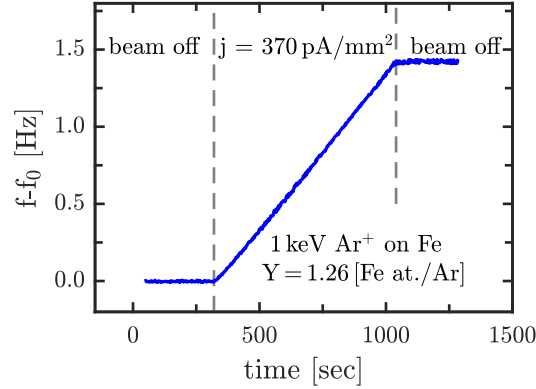
Figure 3.5: QCM measurement of an Fe coated quartz crystal irradiated with Ar^+ ions at $1\,keV$. During the beam off phases, the ion beam is interrupted with a shutter. The slope of the frequency curve during the irradiation (beam on phase) gives information about the mass change of the sample, while the slopes during the beam off phases can be used to evaluate any quartz frequency drift.

In order to minimise uncertainties of the ion current density a stable ion source and a precise measurement of the beam profile and the Faraday cup area is needed. The parameters of the ion source and ion optics (containing also the scanning plates) are optimised until a desired homogeneous beam profile with fluctuations $\leq\ 10\,\%$ are reached. The smallest measurable frequency change of the QCM is limited by the quartz drift $\approx\ 2\,mHz/min$ and the noise of the electronics $\approx\ 5\,mHz$. Since the quartz crystal is oscillating at $6\,MHz$ a relative frequency stability of 9 orders of magnitude can be achieved. By this, a mass change as small as $10^{-11}\,g/s$ (corresponding to $10^{-4}\,W$ monolayers/s) can be detected [64, 65].

3.1.5 Sample Preparation

The target layers investigated during this thesis were prepared by different collaboration partners. In the following section the used deposition technique and the resulting layer system are described:

WN and W target layers: $360\,nm$ thick WN films were prepared at the Jŏzef Stefan Institute in Ljubljana by using a Balzers Sputron triode sputter apparatus (base pressure $7 \cdot 10^{-6}\,mbar$). To improve the adhesion between the gold electrode and the WN layer a $20\,nm$ chromium and a $10\,nm$ tungsten interlayer were used. The elemental composition of the WN film was analysed by time-of-flight elastic recoil detection analysis (TOF-ERDA) using a ^{127}I beam at $20\,MeV$, showing a W/N ratio of 1/1 with $\approx\ 5\,at.\%$ of O and $3\,at.\%$ of Ar impurities [74]. In addition to do

comparison measurements, 300 nm thick pure W films were prepared at the Institute of Solid State Physics (TU Wien) by using a sputter deposition technique.

FeW and Fe target layer: 675 nm thick FeW films with a W concentration of 1.5 at% and 400 nm thick pure iron (Fe) films were prepared at the IPP in Garching. For the deposition a magnetron-sputter device with argon as working gas and multiple targets (Leybold, UNIVEX 450B) were used. By adjusting the input power for each target (Fe, W) the W concentration during the deposition was controlled. RBS with a 3 MeV ^{4}He$^+$ beam as a probe confirmed the W concentration of 1.5 at% and showed that the layer contains O impurities of 1.5 at% and was oxidised at the surface, the Ar impurities stayed below detection limit. Additional information about the deposition can be found in reference [38].

Au target layer: 450 nm thick gold (Au) films were deposited onto one of the gold electrodes of the quartz crystal by using a vapour deposition technique at the Institute of Solid State Physics (TU Wien).

3.1.6 Ion Sources

Two different ion sources were used to irradiate the samples. Depending on the flux or the total fluence needed, either a 14.5 GHz electron cyclotron resonance (ECR) ion source or a sputter gun is used for the production of ions. The two different experimental setups are described in the following section.

Electron Cyclotron Resonance (ECR) Ion Source

The ECR ions source is part of the ion beam facility AUGUSTIN at TU Wien and provides the ions for up to three different experiments. A sketch of the ion source and the beamline quipped with the QCM is shown in figure 3.6. The plasma inside the ECR ion source is confined by a minimum magnetic field configuration, generated by a combination of an axial magnetic mirror field and a radial hexapole field. The injected 14.5 GHz microwave is absorbed by electrons with a gyromotion at a matching frequency and heats the plasma. Via (sequential) electron impact ionisation processes single and multiple charged ions up to e.g. Ar^{14+} can be produced. A parallel and intense ion beam can then be extracted out of the positively biased source by the use of an "Accel-Decel" extraction system consisting of three electrodes [75, 76]. The extracted ion beam is then focused by a quadrupole focusing magnet (QP magnet) and mass over charge selected and directed into the relevant beamline by the sector magnet. Entering the beamline the ion beam passes two sets of aperture ($\varnothing = 5$ mm
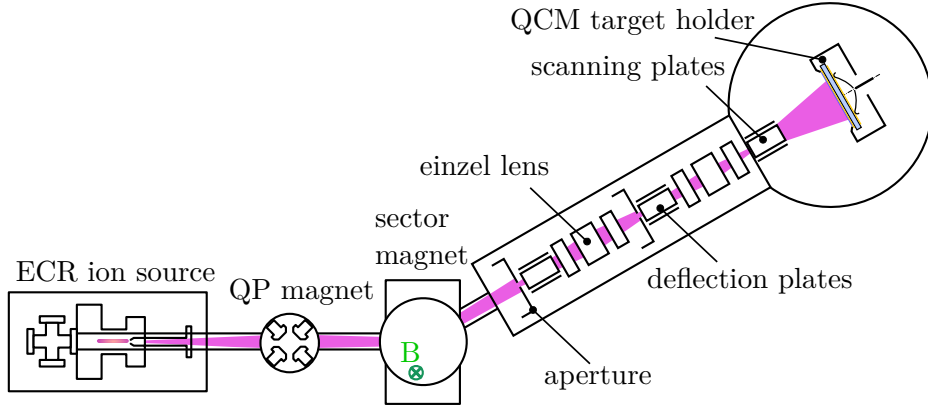
Figure 3.6: Schematics of the ECR ion source and the beamline equipped with the QCM. The ions generated in the ECR ion source are extracted and focused with the quadrupole focusing (QP) magnet and then mass over charge selected by the sector magnet. Entering the beamline the ion beam passes two sets of aperture ($\emptyset = 5$ mm and $\emptyset = 3$ mm), deflection plates and einzel lens. Before hitting the target holder the ion beam passes the scanning plates used for achieving a homogeneous ion beam profile.

and $\emptyset = 3$ mm), deflection plates and an einzel lens. To achieve a homogeneous ion beam profile at the target holder an additional set of deflection plates at the end of the ion optics can be used as scanning plates. The ion source is operated at a typical pressure of 10^{-5} mbar and pumped by a turbo molecular pump. By differentially pumping with a second turbo molecular pump at the sector magnet and two ion pumps at the beamline a low 10^{-10} mbar pressure can be achieved in the target chamber.

For the case of deuterium as working gas for the ion source a D_2^+ beam (scanned over the active area of the QCM) with a typical flux of 10^{16} D/m^2/s and a kinetic energy of 1 to 3 keV/D can be realized. However, the flux provided by the ECR ion source is too low to investigate transient erosions effects of WN and FeW under D ion impact in a reasonable time period (see details and results in section 4). Therefore another experimental setup with a sputter gun as ion source was designed.

Sputter Gun Ion Source

The schematics of the experimental setup is shown in figure 3.7. Singly charged ions are produced inside a Perkin Elmer, PHI Model 04-161 Sputter Ion Gun and extracted with voltages between 500 V and 2000 V in steps of 500 V. The ion beam is then focused with an einzel lens and selected according to their mass by a Colutron
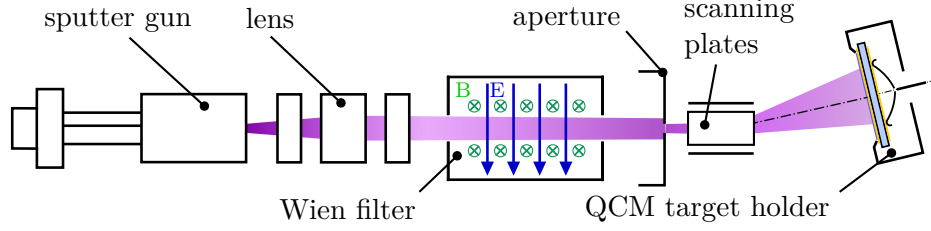
Figure 3.7: Schematics of the sputter gun setup. Ions are produced inside the Perkin Elmer sputter gun and selected according to their mass (velocity) in a Wien filter. To avoid neutrals hitting the target, the ion beam is bent by operating the scanning plates with an additional constant offset. To increase the ion flux this setup is sometimes also operated without the Wien filter, details see text.

Velocity Filter Model 600. In order to avoid neutral projectiles hitting the target, the ion beam is bent by applying an additional constant offset voltage at the scanning plates which are also used for the homogeneous irradiation of the target. The working gas pressure of the sputter gun is measured with a Balzers IKR 020 Penning gauge and controlled with a Balzers thermomechanical UDV 135 gas regulating valve. For deuterium as working gas a typical D_2^+ flux at the target in the order of $10^{17}\,\mathrm{D/m^2/s}$ can be achieved. By removing the Wien velocity filter the ion flux at the target increases roughly by a factor of 10 due to the reduced distance between the sputter gun and the target, with the drawback of having an unfiltered ion beam. Therefore the ion beam is first characterized using the Wien filter which is then removed to increase the ion flux. The characterization with the velocity filter shows that the sputter gun operated with deuterium almost exclusively produces D_2^+ (94.5 %) ions and a small amount of D^+ (1.7 %) and D_3^+ (2.6 %). Since the Wien filter is not bakeable and can not be pumped as well as a setup without the filter also a small amount of impurities H_2O^+ (0.7 %) and N_2^+ (0.5 %) is visible in the spectra. By removing the velocity filter and backing the chamber the background pressure can be reduced by one order of magnitude to a low $10^{-8}\,\mathrm{mbar}$ value. Resulting in a reduced amount of impurities, in detail H_2O^+ (0.11 %), N_2^+ (0.02 %) and $< 0.01\%$ others, checked with a quadrupole mass spectrometer mounted at the target chamber.

The influence on the sputtering yield of W/WN and Fe/FeW targets by treating the unfiltered ion beam as a pure D_2^+ beam is estimated to be below 5 %, by using the composition of the ion beam with the respective kinetic energy for each projectile. With the sputtering yield SPY_i taken form literature [57] for the certain particle the resulting sputtering SPY is calculated as follows,

$$SPY = \sum SPY_i \cdot c_i \tag{3.8}$$

with c_i being the quantity of each projectile in %. A comparison of the sputtering yield of the unfiltered beam to the sputtering yield obtained with a pure D_2^+ beam

results then in an error below 5 % for the used extraction voltages of 500 V for FeW /Fe and 1000 and 2000 V for W/WN .

3.2 Simulation Code - SDTrimSP

To simulate the interaction of ions bombarding a target, different Monte Carlo simulation programs are established. The most popular codes are "transport of ions in matter" (TRIM) [77], its dynamic version (TRIDYN) [78,79] , "stopping and range of ions in matter" (SRIM) [80], and SDTrimSP [81]. SD stands for static/dynamic and SP for sequential/parallel processing. SDTrimSP is a further development of TRIM and TRIDYN and combines the possibilities of both of them. All these simulation codes have different strengths and weaknesses. SRIM contains a huge database on experimental stopping powers and a comfortable user interface and convinces with the simulation of ion ranges, energy loss and damage profiles. However, a drawback of SRIM is the only rudimentary implemented sputtering of the target. The strength of SDTrimSP is the quantitative good agreement with experimental data in calculating the sputtering yield, as well as the respective angular distributions of the sputtered and reflected species. A detailed comparison of the simulation programs highlighting their strengths and weaknesses can be found in reference [82].

Since the work of this thesis focuses on sputtering, SDTrimSP is used for simulating the interaction of projectiles with a target. The basic physics of the Monte Carlo program SDTrimSP is the same as in the previous ones (TRIM, TRIDYN) and is well described in reference [52]. The name "Monte-Carlo" derives form the fact that the next collision partner is not deterministically resulting from the previous impact, but is chosen randomly. This approach restricts the program to the modelling of amorphous materials with randomly distributed atom positions. In SDTrimSP the nuclear collisions (collision cascade) generated by the impinging projectile is approximated by a sequence of independent elastic binary collisions described by an interaction potential. The trajectory of the projectile and the recoils are followed until their kinetic energy reaches a certain cut-off energy of a few eV. As interaction potential, different screened coulomb potentials can be selected in SDTrimSP. Reference [81] lists the supported interaction potentials and compares the impact on the results (default interaction potential - KrC [83]).

As mentioned above SDTrimSP is capable of performing dynamic and static simulations. While for the static mode the target does not change due to the particle impact, in the dynamic mode the target will change dynamically. To this purpose the target is divided into $i = 1 \ldots n_L$ layers of thickness Δx_i with the fractional composition q_{ij} of all $j = 1 \ldots n_c$ elements in the system. The so defined target is bombarded with

N_H particles, each carrying a fraction $\Delta\phi = \phi_0/N_H$ of the total simulated fluence ϕ_0. Due to implantation and/or sputtering the number of particles of the element j in the layer i is changed by Δn_{ij}. The resulting partial areal density v_{ij} can then be calculated as follows:

$$v_{ij} = q_{ij}n_i\Delta x_i + \Delta n_{ij}\Delta\phi \tag{3.9}$$

where n_i is total density in each layer i. The change in partial areal density v_{ij} due to the bombardment with the fractional fluence $\Delta\phi$ leads to a new concentration distribution q_{ij} and to a change in the layer thickness Δx_i. The new fractional composition q_{ij} of the element j and the new thickness Δx_i of the layer i is then calculated according to [79]:

$$
\begin{aligned}
q_{ij} &= \frac{v_{ij}}{\sum_{k=1}^{n_c} v_{ik}} \\
\Delta x_i &= \sum_{j=1}^{n_c} \frac{v_{ij}}{N_{0i}}
\end{aligned}
\tag{3.10}
$$

where $\sum_{k=1}^{n_c} q_{ik} = 1$ and $N_{0,j}$ is the density of the pure elements. Prior to the start of a new bombarded with N_H particles, the grid is converted into an equidistant one with the original thickens Δx by interpolation.

An atom at the surface is considered to be sputtered if its momentum $p_\perp$ normal to the surface is larger than the binding strength of the atom to the surface (surface binding energy sbe):

$$p_\perp^2/2m > sbe \tag{3.11}$$

The surface binding energy sbe of atoms in a target is therefore an important input parameter for the simulation and for pure elements this value is usually approximated by the heat of sublimation. For mixed materials SDTrimSP provides different models. In the following a composition dependent surface binding energy model is used for multi component systems, where E_s is the atomic surface binding energy for each species and c the atomic fraction. For the case of WN the surface binding energy sbe of N and W in WN is calculated as follows:

$$
\begin{aligned}
sbe_W &= c_N \cdot 0.5(E_{sW} + E_{sN}) + c_W \cdot E_{sW} \\
sbe_N &= c_W \cdot 0.5(E_{sW} + E_{sN}) + c_N \cdot E_{sN}
\end{aligned}
\tag{3.12}
$$

Using literature data for the atomic surface binding energy of W [84] and N [85,86]

$$
\begin{aligned}
E_{sW} &= 8.8\,\text{eV} \\
E_{sN} &= 4.6\,\text{eV}
\end{aligned}
\tag{3.13}
$$

Table 3.2: Input parameters that were used in the presented SDTrimSP simulations. The input parameters are derived from [84][1], [85][2], [86] [3].

target surface	element	atomic density [at. / Å^3]	surface binding energy [eV]
WN	W	0.06306	8.8[1]
	N	0.15750	4.6[2,3]
FeW	Fe	0.08491[1]	4.28[1]
	W	0.06306	8.8[1]
Au	Au	0.05907[1]	3.79

the binding energy varies for N from 5.65 eV (in W/N = 1/1) to 6.7 eV (in pure W) and for W from 7.75 eV (in W/N = 1/1) to 8.8 eV (in pure W). Table 3.2 lists the input parameters used for the performed SDTrimSP simulations.

For the sake of completeness, it should be mentioned that besides the simulation programs described above, others like molecular dynamics simulation programs are also used to describe sputtering. Molecular dynamics simulation are based on the simple strategy of following the particles and solving the Newton's equations of motion. A big disadvantage of these programs is the huge amount of computer power needed (they are four to five orders of magnitude slower than calculations based on binary collision approximations).

3.3 Quartz Crystal Microbalance Catcher Configuration

So far, sputtering experiments have been performed at the Institute of Applied Physics using the self-built and optimised highly sensitive QCM technique (described in section 3.1). However, the use of the existing QCM technique limits the possible sputter targets to materials which can be deployed as a thin film on top of the QCM. Furthermore the use of the coated quartz crystals as sputter target makes it difficult to vary parameters like the surface roughness or the target temperature, which would be of interest for example, for studies on fusion reactor wall materials.

To overcome these limitations for the existing QCM technique, a new setup was designed where a QCM placed next to the sputter target acts as a catcher for the sputtered material. The goal of this catcher setup is the determination of sputter yields without direct measurements at the target. It benefits from the precision of the QCM technique and the possibility of using almost any target. To realize this, it is necessary to know the setup geometry and the angular distributions of the sputtered
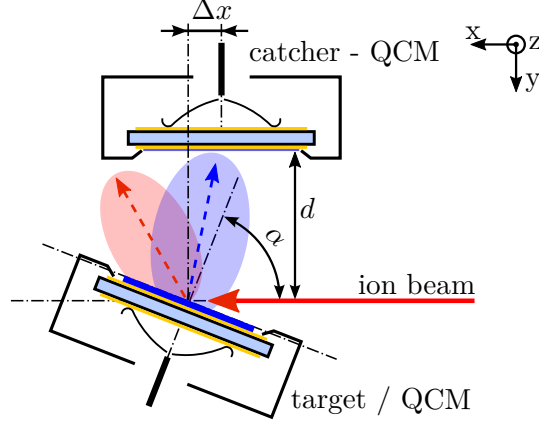
Figure 3.8: Schematics of the catcher setup. A sputter target (target-QCM) is hit under the angle α by the ion beam (red arrow). The shaded areas indicate the angular distributions of the sputtered target particles (blue) and reflected projectiles (red). A QCM placed next to the target, at a distance d parallel to the ion beam direction (with displacement Δx), acts as a catcher for the sputtered material (catcher-QCM). Figure adapted from [63].

and reflected particles, in order to reconstruct the sputtering yield of the target with the measured signal of the catcher-QCM [63].

3.3.1 Experimental Setup

The schematics of the catcher-QCM setup built during this thesis is shown in figure 3.8. A sputter target mounted on the x, y, z, ϕ manipulator is hit under an angle α with respect to the surface normal by the ion beam (red arrow). The ion beam is provided by the ECR ion source (described in section 3.1.6). Due to the ion impact at the target two angular distributions of sputtered particles (blue) and reflected projectiles (red) are emitted from the surface, indicated by the shaded areas in figure 3.8. A fraction of the sputtered target material is collected by a catcher-QCM mounted parallel to the ion beam at the distance d. Such a catcher-QCM has been added to the existing beamline equipped with the QCM described in section 3.1.6. The distance d between the centre of the ion beam and the catcher quartz surface can be adjusted by a linear manipulator. The angle of incidence α or the distance Δx between the centre of the catcher-QCM (selected to be the x-coordinate origin) and the central strike point of the ion beam can be modified with the 4-axis manipulator on which the (QCM) target holder is mounted. As target either a second (target-) QCM or any solid or even liquid material can be used. In contrast to direct QCM measurements where typically the frequency increases due to a mass decrease, now the resonance
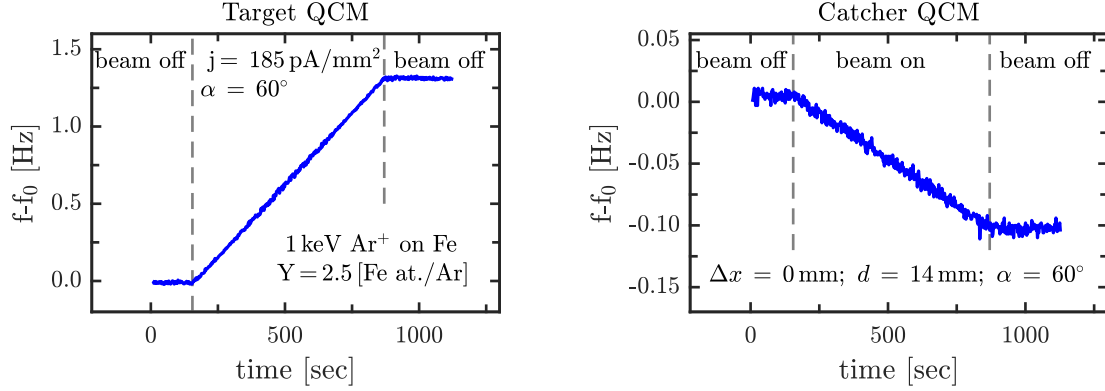
Figure 3.9: Typical frequency response of the target-QCM and the catcher-QCM to a $1\,keV\ Ar^+$ ion beam hitting the Fe target layer. The measurement starts with a beam-off period to check the frequency drift of the QCMs, followed by a beam on period, where the target-QCM is irradiated. During the beam-on period the target-QCM shows an increase of the resonance frequency due to sputtering (mass decrease), while the catcher-QCM shows a decrease of the resonance frequency due to collected particles (mass increase).

frequency of the catcher-QCM decreases due to the mass increase by the collected sputtered material.

Figure 3.9 shows the typical frequency response of such a configuration with two QCMs. The measurement starts with a beam off period where the ion beam is interrupted by a shutter to check the frequency drift and the correct operation of the QCMs. This is followed by a beam on period where a target layer (deposited onto the target-QCM) is homogeneously irradiated with an ion beam. In the current case, a Fe target layer is hit by a $1\,keV\ Ar^+$ ion beam with a current density of $j = 185\,pA/mm^2$. During this period, the target-QCM shows an increase of its resonance frequency due to the mass loss from sputtering, while the catcher-QCM shows a decrease of its resonance frequency due to the mass increase from collected sputtered material. At the end of the measurement the ion beam is again interrupted and the quartz drift checked.

In order to evaluate the signal obtained by the catcher-QCM, the knowledge of the total ion current hitting the target is necessary. Therefore the scanned ion beam is controlled with a set of multiple apertures (Ø 2, 3, 4, 7 mm) that can be moved into the beam's path directly in front of the target layer, shown in figure 3.10. The aperture with the Ø = 7 mm is also equipped with additional electrodes for secondary electron suppression and can be used as a real-time ion beam monitor, a detailed description of the design of the beam monitor is given in reference [87]. Figure 3.10 (right), shows an image of the catcher-QCM and the set of apertures with the wiring
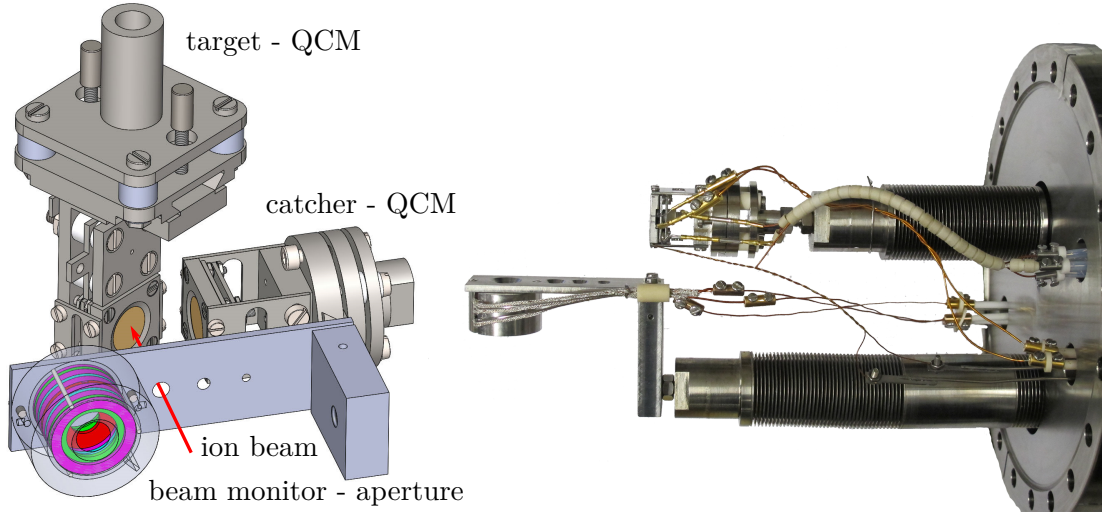
Figure 3.10: (left) CAD model of the QCM catcher configuration. To control the scanned ion beam a set of multiple apertures (Ø 2, 3, 4, 7 mm) can be moved into the beam's path directly in front of the target layer. (right) Image of the catcher-QCM together with the set of apertures mounted on a CF-160 flange. Both can be positioned with the respective linear manipulator.

and current feedtroughs needed mounted on a CF-160 flange. The whole setup is so designed that it can easily be attached to the existing QCM setup with the CF-160 flange.

3.3.2 Data Evaluation

In contrast to the target-QCM, where the mass change rate (sputtering yield) is directly determined by equation 3.4, as describes in section 3.1, the evaluation of the sputtering yield from the catcher-QCM signal is less straightforward. The yield obtained by the catcher-QCM is not only dependent on the sputtering yield of the target, but also on the angular distributions of the sputtered and reflected particles and some geometric parameters determining the solid angle covered by the catcher. Due to the incomplete collection of sputtered material, the frequency change of the catcher-QCM is roughly by a factor of 10 smaller than the frequency change of the target-QCM.

In order to describe the measured catcher yield, two contributions have to be taken into account. Firstly, the contribution $Y_{c,sp}$ of atoms sputtered from the target that will hit the catcher-QCM and stick to its surface. Secondly, the contribution $Y_{c,r}$ of projectiles reflected by the target surface hitting and eroding the catcher surface.

The erosion of the catcher surface by sputtered particles will be neglected due to their comparably low kinetic energy [48, 88]. The resulting measured yield Y_c at the catcher-QCM is thus the difference of the mass increase due to collected sputtered particles and the mass decrease due to erosion caused by reflected projectiles:

$$Y_c = Y_{c,sp} - Y_{c,r} \tag{3.14}$$

The yield of collected atoms is proportional to the target sputtering yield Y_{tar}, the probability that sputtered material reaching the catcher surface sticks there C_{st} and a parameter g_{sp}:

$$Y_{c,sp} = C_{st} \cdot g_{sp} \cdot Y_{tar} \tag{3.15}$$

The parameter g_{sp} comprises the (in section 3.1.2 described) quartz crystal's local sensitivity to a mass change $s(x, y)$, the spatial distribution of the sputtered target material $f_{sp}(\Omega)$ (with Ω being the solid angle), the ion current density profile $j(x_t, y_t)$ hitting the target and the relative position of the catcher and the target characterised by the parameters α, Δx and d. In order to specify the parameter g_{sp}, we first take a point shaped ion beam hitting the target and creating an angular distribution $f_{sp}(\Omega)$ of sputtered atoms with:

$$\int_{2\pi} f_{sp}(\Omega) = 1 \tag{3.16}$$

The number of atoms hitting the catcher is then given by the integration of $Y_{tar} \cdot f_{sp}$ over all the angles that represent directions intersecting with the catcher quartz surface. In order to determine the contribution of the integrand to the measured signal, the spatial distribution f_{sp} has to be weighted with the sensitivity $s(x_c(\Omega), y_c(\Omega))$ of the quartz to a mass change. With the local coordinates x_c and y_c in the plane of the catcher surface dependent on the polar angle θ and the azimuthal angle ϕ. The position and orientation of the surface results from the position of the catcher and therefore, all the necessary information is included in x_c and y_c. The limited size of the active area of the quartz crystal is included in the sensitivity $s(x_c(\Omega), y_c(\Omega))$ and for this reason, the integration can be performed over all angles.

For a finite ion beam the sputtered atoms do not originate at the same point, but across the area of the beam cross section, represented by the current density $j(x_t, y_t)$ with:

$$\int_A j(x_t, y_t) dA = I \tag{3.17}$$

were x_t and y_t are the in plane coordinates of the target surface and I the total ion current hitting the target. The spatial distribution of sputtered particles for an expanded ion beam hitting the target can then be written as:

$$\frac{1}{I} \int_A j(x_t, y_t) \cdot f_{sp}(\Omega, x_t, y_t) \, dA \tag{3.18}$$

with $f_{sp}(\Omega, x_t, y_t)$ being the spatial distribution created by a point shaped ion beam originating at the point (x_t, y_t). As a result, the parameter g_{sp} can then be written as:

$$g_{sp} = \frac{1}{I} \int_A \int_{2\pi} j(x_t, y_t) \cdot f_{sp}(\Omega, x_t, y_t) \cdot s(x_c(\Omega), y_c(\Omega)) \, d\Omega dA \qquad (3.19)$$

Similarly, the yield $Y_{c,r}$ of the projectiles reflected at the target, eroding the catcher surface can be described with the parameter g_r and the reflection probability P_r of the incoming ions at the target:

$$Y_{c,r} = g_r \cdot P_r \qquad (3.20)$$

Equivalent to f_{sp}, f_r is used to describe the distribution of the ions reflected at the target. But in contrast to before, the number of atoms sputtered from the catcher surface by the reflected projectiles is of importance, which depends both on the energy and angular distribution $f_r(\Omega, E)$ of the reflected projectiles. For this reason the sputtering yield $Y(\alpha_r, E)$ dependent on the reflected projectiles' angle of incidence α_r on the catcher surface and their energy E is required. Taking these aspects into account, an adaptation of equation 3.19 gives the parameter for the reflected ions:

$$g_r = \frac{1}{I} \int_A \int_0^\infty \int_{2\pi} j(x_t, y_t) \cdot f_r(\Omega, E, x_t, y_t) \cdot Y(\alpha_r, E) \cdot s(x_c(\Omega), y_c(\Omega)) \, d\Omega dE dA$$
$$(3.21)$$

The ratio g between the yield at the catcher Y_c and the yield at the target Y_{tar} can then be described:

$$Y_c = Y_{c,sp} - Y_{c,r} = C_{st} \cdot g_{sp} \cdot Y_{tar} - g_r \cdot P_r$$
$$= \left(C_{sp} \cdot g_{sp} - g_r \cdot \frac{P_r}{Y_{tar}} \right) Y_{tar} = g \cdot Y_{tar} \qquad (3.22)$$

$$\Rightarrow g = C_{st} \cdot g_{sp} - g_r \cdot \frac{P_r}{Y_{tar}} \qquad (3.23)$$

This combined parameter represents a possibility of comparison between experimental and theoretical results. On one hand, both Y_c and Y_{tar} can be measured simultaneously by using a QCM target. On the other hand, the sputtering yield Y_{tar}, the reflection probability of the projectile ions' P_r as well as their respective angular distributions f_{sp} and f_r can be calculated in SDTrimSP simulations. With these parameters, the quartz's sensitivity s, the measured current density j and the sticking coefficient C_{st}, the ratio g can be calculated.

As a result, it is possible to reconstruct the target yield Y_{tar} using the experimentally determined catcher yield Y_c and the calculated parameter g. The feasibility of determining sputtering yields by the catcher-QCM method, is shown with proof of principle measurements with the well-known projectile-target combination Ar^+ on Au and Ar^+ on Fe in section 4.3.

4 Results

The following chapter presents the results obtained for the fusion relevant surfaces [62, 89] and shows the proof of principle measurements which demonstrate the feasibility of the QCM catcher method [63].

Contents

4.1 Erosion of WN layers by D Ions

In today's tokamaks like ASDEX Upgrade and JET or a future fusion power plant with a full metal first wall, impurity seeding into the plasma is required to reduce the power flux to the divertor and to increase the overall plasma performance [30, 90, 91]. E.g. N_2 seeding with feedback control is now a standard operational scenario at ASDEX Upgrade and being an effective coolant at the plasma edge in the 10 eV temperature range [27, 28]. Studies on the erosion of W by N showed that the use of N in combination with W surfaces leads to the formation of tungsten-nitride (WN) surface layers within the ions penetration depth. The interaction of N with W and WN is now well investigated and processes like N retention, N co-deposition or the implantation of N are well described [31–33]. However, little is known about the interaction of WN with D.

Recently, the D retention and N removal as well as the penetration of D in WN surfaces was investigated under deuterium plasma exposure [92]. But still questions remain such as: "How does N change the erosion behaviour of W under D exposure?" To address these questions, the erosion of well prepared WN films by impact of mono-energetic deuterium projectiles is studied in this thesis under laboratory conditions.

The results presented in this section have been published in [62] and parts of this section are excerpts from this publication.

4.1.1 Experimental Results

Erosion rates of WN layers under D ion bombardment are investigated under controlled laboratory conditions using the QCM setup that was introduced in section 3.1. To operate the QCM under the best conditions the whole QCM target holder is heated to the frequency over temperature minimum of the quartz crystal at typically 465 K. The temperature of the QCM is measured and monitored during the whole measurement using a K-type thermocouple. As target layers, 360 nm thick WN films (prepared at the Jŏzef Stefan Institute) and 300 nm thick pure W films (prepared at the Institute of Solid State Physics, TU Wien) deposited onto the QCM were used (cf. section 3.1.5). Analysis of the elemental composition of the WN films showed a W/N ratio of 1/1 with $\approx$ 5 at.% of O and 3 at.% of Ar impurities [74]. To irradiate the target layers a D_2^+ ion beam produced by a Perkin Elmer sputter gun with a typical flux of $10^{18}\,\mathrm{m^{-2}s^{-1}}$ and kinetic energies between $500 - 1000\,\mathrm{eV/D}$ was used. A detailed description of the ion source is given in section 3.1.6. The total mass change of the
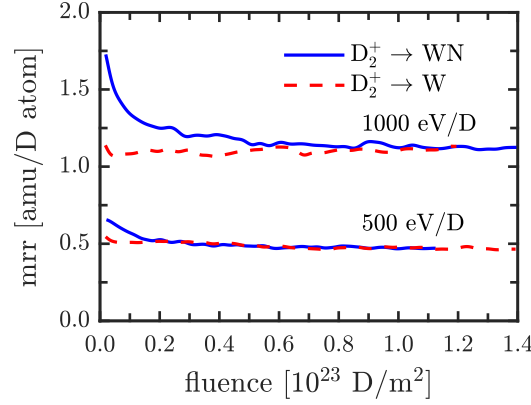
Figure 4.1: Evolution of the mass removal rate (mrr) of WN and W films as a function of the applied D fluence. For both kinetic energies, a transient enhancement in the mass removal rate is seen. Steady state conditions are obtained at fluences of about $0.2 \cdot 10^{23}\,\mathrm{D/m^2}$ and $0.6 \cdot 10^{23}\,\mathrm{D/m^2}$ for $500\,\mathrm{eV/D}$ and $1000\,\mathrm{eV/D}$ bombardment, respectively. Figure published in [62].

target film is determined from the change of the quartz crystal's resonance frequency according to equation 3.2. In order to investigate the transient erosion behaviour of the target layer, it is continuously bombarded with the ion beam and the resonance frequency of the QCM is recorded. As described in section 3.1.3 the derivative df/dt of the recorded frequency vs time curve is used to calculate the mass change of the target film. Thereby only the total mass change per impinging projectile can be determined in amu/ion and no information on the actually sputtered species is given.

Experimental results for D_2^+ ions bombarding freshly prepared WN and W layers under normal incidence at $500\,\mathrm{eV/D}$ and $1000\,\mathrm{eV/D}$ are shown in figure 4.1. For both kinetic energies, the measured mass removal rate for WN is higher for low fluences than for pure W. This enhancement decreases with increasing fluence, finally reaching (within the experimental uncertainties) the steady state value of pure W erosion. For the $1000\,\mathrm{eV/D}$ bombardment a fluence of about $0.6 \cdot 10^{23}\,\mathrm{D/m^2}$ is necessary to reach steady state conditions while for the $500\,\mathrm{eV/D}$ bombardment steady state conditions are reached at a fluence of about $0.2 \cdot 10^{23}\,\mathrm{D/m^2}$. For the pure W targets the measured mass removal rates stay constant within the applied ion bombardment and do not change with fluence, for both energies.

Figure 4.2 shows the measured steady state mass removal rates for W and WN (full symbols) as a function of the D energy. In order to compare the measured data to literature values, the mass removal rate (in amu/D atom) was converted to a sputtering yield (right y axis) assuming erosion of pure W ($184\,\mathrm{amu/D}$ atom is equivalent to $1\,\mathrm{W}$ atom/D atom). The open symbols in figure 4.2 are W sputtering yields measured by Sugiyama et al. [93] with Rutherford backscattering analysis (RBS) and
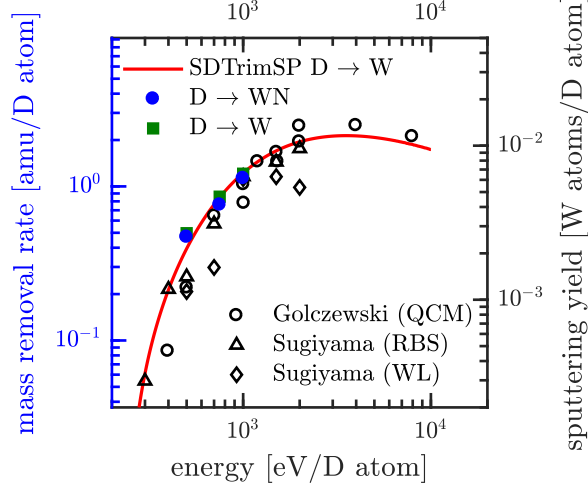
Figure 4.2: Measured mass removal rates for W and WN after reaching steady state conditions as a function of the D energy. In order to compare the measured data to literature data on W sputtering [66, 93] the sputtering yield (right y axis) is scaled to the mass removal rate of pure W. The red curve follows a SDTrimSP simulation for pure W under D bombardment. Figure published in [62].

weight loss (WL) technique and earlier QCM results by Golczewski et al. [66]. The red curve represents a SDTrimSP simulation for W under D bombardment. The literature data as well as the SDTrimSP calculation are in a good agreement with the obtained results.

4.1.2 Simulations and Discussion

The experimental results were simulated using the Monte Carlo code SDTrimSP introduced in section 3.2 [79, 81]. SDTrimSP can be used to simulate collision effects in (amorphous) solids like (preferential) sputtering, range profiles of implanted ions and dynamically changing composition profiles of the target using a binary-collision approximation. Since WN is a multi component system a composition dependent surface binding energy model is used were the N and W surface binding energies change with N concentration based on surface binding energy values taken from the literature; i.e. for N from $5.65\,\mathrm{eV}$ (in W/N $=1/1$) to $6.7\,\mathrm{eV}$ (in pure W) [85, 94] and for W from $7.75\,\mathrm{eV}$ (in W/N $=1/1$) to $8.8\,\mathrm{eV}$ (in pure W) [84] (cf. section 3.2).

The evolution of the simulated N surface concentration with increasing D fluence for a WN target with an initial composition of 50% N and 50% W is shown in figure 4.3. Comparing the trend of the simulated N surface concentration in figure 4.3 with
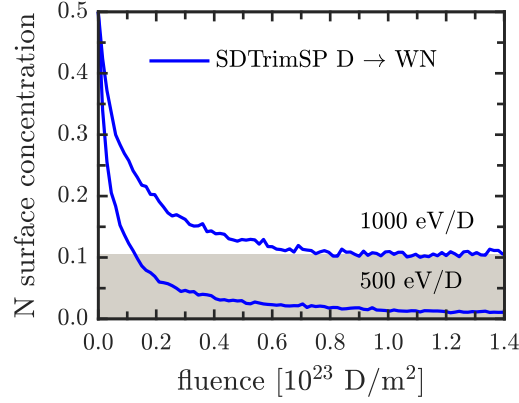
Figure 4.3: N surface concentration as a function of D fluence as calculated with SDTrimSP for a WN target with an initial composition of 50 % N and 50 % W. For 1000 eV/D the simulated N surface concentration reaches a steady state value at about 10 %, for 500 eV/D the N surface concentration drops to 1 % − 2 %. Figure published in [62].

the trend of the measured mass removal rate for WN from figure, 4.1, it seems likely that the decrease of the mass removal rate with increasing fluence is caused by the decreasing N surface concentration. In particular, for 1000 eV/D impact the surface concentration of N reaches a steady state value $(10\% - 11\%)$ at a very similar fluence $(0.6 \cdot 10^{23} \, \text{D/m}^2)$ as the corresponding mass removal rate.

Measuring the same steady state mass removal rate for WN and W can be explained as follows. During the transient initial phase N is preferentially sputtered and a N depleted surface layer is produced. This N depleted surface layer is maintained during further sputtering, because N is removed from the layer at the same rate as W is sputtered (steady state conditions). Due to the large difference in the mass of N (14 amu) and W (184 amu) the contribution of N to the measured mass removal rate is only $\approx 7\%$ (exactly $14/(184+14)$). Under the circumstance that the measured mass removal rate for WN is reaching the same value as the mass removal rate for W, it seems likely that the W sputtering yield for WN should actually be slightly lower. However, considering the experimental uncertainties this difference cannot be clearly shown.

Despite the qualitative agreement of the simulated surface concentration and the experimentally observed fluence dependence, the mass loss rates shown in figure 4.1 are not completely reproduced by SDTrimSP. In particular, the transient enhancement of the erosion yield at low fluences is suppressed in the simulation. This discrepancy could be fixed by an adjustment of the surface binding energy values to 4.7 eV for N and 6.75 eV for W in the SDTrimSP simulation, but such low values seem rather unphysical and don't agree with surface binding energy values in the literature. A more likely
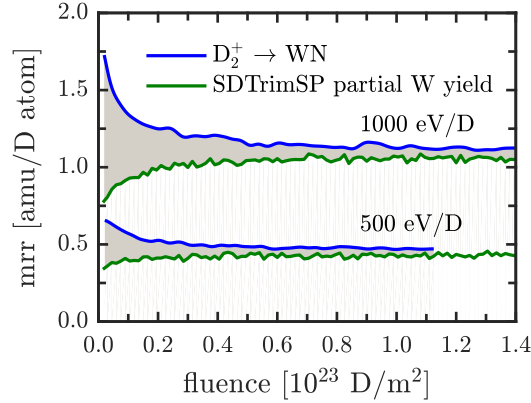
Figure 4.4: Comparison of the experimentally observed mass removal rate of WN (blue) as a function of the applied D fluence with the in SDTrimSP calculated partial W mass removal rate (green) for WN. Assuming that the later one is correct, the grey area represents the amount of nitrogen that needs to be removed in order to get perfect agreement between SDTrimSP simulation and experimental results. Figure published in [62].

explanation is that nitrogen diffusion, in particular irradiation-induced diffusion [95] of nitrogen, which is not yet implemented in the SDTrimSP code, increases the N loss and leads to the enhanced erosion yield at low fluences. Indications that such irradiation-induced N diffusion occurs, were already reported in [32]. In particular, an unexpected difference in the N content was observed when N is implanted before the W target is heated compared to a N implantation into the heated sample.

To determine the N amount that needs to be eroded in order to obtain a perfect agreement between experiment and simulation, figure 4.4 compares the experimentally measured WN mass removal rate with the partial tungsten mass removal rate simulated by SDTrimSP. Under the assumption that the partial tungsten yield is approximately correctly described by SDTrimSP, the difference between the two curves (grey area) represents the amount of N that was removed in the experiment. For a D impact energy of $1000 \, \mathrm{eV/D}$, the grey area corresponds to $\approx 1.4 \cdot 10^{21} \, \mathrm{N}$ atoms/m^2 equivalent to a 100% N removal over 12 nm. For $500 \, \mathrm{eV/D}$ a N loss of $\approx 5.9 \cdot 10^{20} \, \mathrm{N}$ atoms/m^2 would fit to the grey area which is equivalent to a 100% N removal over 5 nm assuming a density of 0.11 atoms/Å^3 for WN.

Figure 4.5 shows the simulated nitrogen depth distribution for different D fluences and a kinetic projectile energy of $1000 \, \mathrm{eV/D}$. In the simulation the N depletion in the near surface region is not only caused by sputtering of N atoms but is also due to a N concentration increase in deeper layers. This concentration increase has nothing to do with N diffusion (not included in the SDTrimSP code), but with implantation of

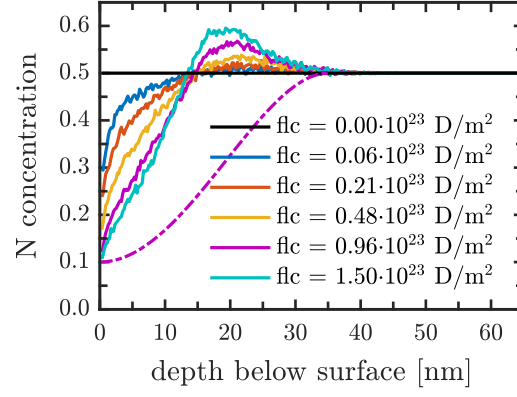**Figure 4.5:** Calculated N depth distributions for different D fluences (flc) and an impact energy of $1000\,\text{eV/D}$. The dash-dotted line shows an assumed N concentration profile, which would be consistent with the experimental results shown in figure 4.1. Figure published in [62].
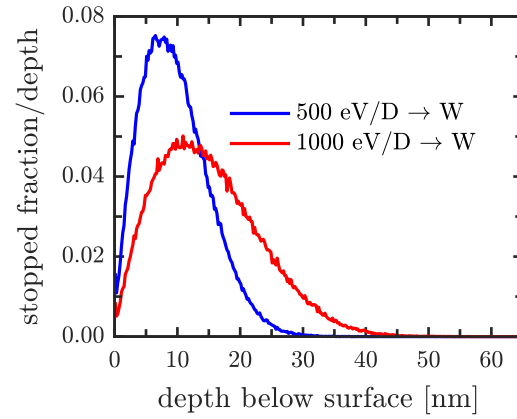
Figure 4.6: Simulated (SDTrimSP) range distribution for D bombarding W, at $500\,\text{eV/D}$ (blue) and $1000\,\text{eV/D}$ (red).

recoiling N atoms into deeper layers of the bulk. In order not to reach an unphysical high N concentration, an artificially N limit of 60% was set in SDTrimSP. N atoms exceeding this pre-set limit are removed from the calculation by the code and contribute to the sputtering yield. However, in order to be consistent with the experimentally obtained results, an amount of nitrogen would have to be removed that corresponds to the dash-dotted depth profile in figure 4.5. Taking into account the range distribution of D projectiles in W, shown in figure 4.6, it is in principle possible that irradiation-induced diffusion assists the N loss within the ions penetration depth. Another possible explanation for the experimentally observed enhanced mass removal rate would be chemical erosion, e.g. by the formation of ammonia [86], but since ND_3 will probably not be very mobile in W, this explanation would again require the diffusion of a comparable amount of N to the surface.

4.1.3 Summary

The erosion of well prepared WN and W films was studied under $500\,\mathrm{eV/D}$ and $1000\,\mathrm{eV/D}$ ion bombardment. The experiments were conducted under laboratory conditions using a highly sensitive QCM technique to determine the mass change in situ and in real time. As ion source a sputter gun was used providing a well pre-characterised molecular D_2^+ ion beam with a typical flux of $10^{18}\,\mathrm{m^{-2}s^{-1}}$. For W a constant mass removal rate was measured, while for WN an enhanced mass removal rate was observed up to a fluence of $0.2 \cdot 10^{23}\,\mathrm{D/m^2}$ for $500\,\mathrm{eV/D}$ and $0.6 \cdot 10^{23}\,\mathrm{D/m^2}$ for $1000\,\mathrm{eV/D}$. Under steady state conditions the mass removal rate of WN approaches that of pure W, within the experimental uncertainties.

Comparing the QCM results to SDTrimSP simulations indicate, that the N surface concentration follows the same trend with D fluence as the experimentally observed mass removal rate for WN. But simulations on the erosion rate for WN differ from the experimental data, indicating that not enough N is removed from the surface near regions. By comparing the experimental data with the simulated partial W yield, the amount of N was estimated that has to be eroded. In order to get a perfect agreement between experiment and simulation. In order to explain that enhanced N erosion, irradiation-induced diffusion was considered as a possible mechanism. This seems to be quite possible if one considers the range distribution of D in W.

4.2 Erosion of FeW Model System upon D Ion Irradiation

For future tokamaks like ITER the selection of plasma facing materials is complicated due to anticipated transient power loads caused by ELMs (edge localised mode) or plasma disruptions [16]. However, when one moves to a future power plant or DEMO, a stable and quiescent plasma is presumed, where the lifetime of the PFCs will be dominated by plasma induced erosion due to sputtering.

The erosion yield of high-Z materials like W is considerably lower than the erosion of low-Z materials or mid-Z materials like Fe, at the expected low ion energies in the near surface region [34]. Figure 4.7 shows the D sputtering yields for a pure W and Fe target as a function of the projectile energy. For projectile energies below $\approx 230\,\mathrm{eV/D}$ no W is sputtered, while for Fe, projectile energies larger than $40\,\mathrm{eV/D}$ are sufficient to trigger a sputter event [57]. Using a tungsten containing steel for recessed areas in a future fusion reactor, it is expected that preferential sputtering of medium-Z steel elements reduces the erosion yield and increases the lifetime considerably. Thereby tungsten containing steels (e.g. EUROFER [36]) could be an attractive alternative - both technologically and economically - to a full tungsten armour [34, 35] at least in less exposed areas.

Recent investigations by Roth et al [37] showed that the erosion rate of EUROFER decreases roughly by $1 - 2$ orders of magnitude under high flux low energy D plasma bombardment. Additional RBS investigations of the exposed surfaces showed a W surface enrichment correlating with the yield reduction (cf. section 2.2). Further investigations by Sugiyama et. al [38] using FeW model films with different W concentrations and a mass selected D_2^+ beam between 200 and $1000\,\mathrm{eV/D}$ confirmed this expected reduction of the erosion yield with D fluence and also found a strong surface enrichment of W with increasing fluence due to preferential sputtering of Fe. While these experiments indicate, that there is a strong correlation between the erosion yield and the W surface enrichment, there is still a quantitative discrepancy between experimental observations and simulation remaining [38]. In particular, SDTrimSP calculations predict a significantly higher W enrichment, than those found in the RBS measurements. This discrepancy could be explained by both experimental and simulation uncertainties. For the low energy D irradiation, the W accumulation takes place in a very thin layer, which is probably thinner than the resolution of the used depth profiling methods. In this case, the apparent W concentration at the surface is lower than the real W concentration at the top. Another possibility could be the presence of a nano scale surface roughness after the ion bombardment, since roughness generally broadens the by RBS measured W profile, resulting in an underestimation of the W concentration [38].
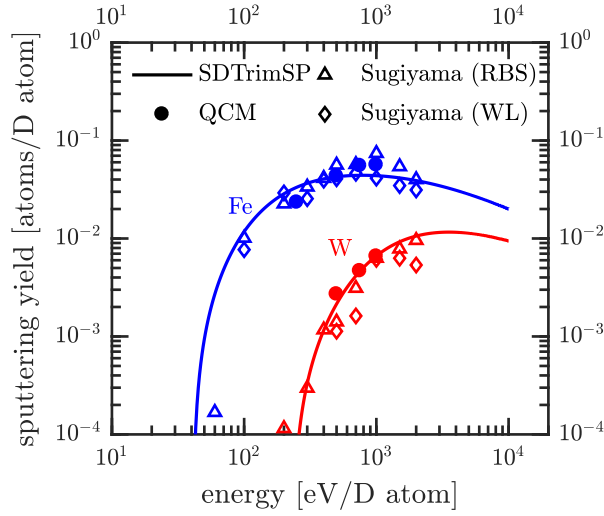
Figure 4.7: Comparison between W and Fe sputtering yields as a function of the D projectile energy. The full symbols (dots) are experimentally determined sputtering yields using the QCM technique, the open symbols are data from literature [93] using a weight loss (WL) and a Rutherford backscattering technique (RBS). The solid line is a SDTrimSP simulation.

In order to gain a profound understanding of this W surface enrichment process due to the interaction of D ions with W containing steels, experiments were carried out using a well-defined FeW model system (containing 1.5 at% W) instead of EUROFER or other reduced-activation ferritic martensitic steels.

The results presented in this section have been published in Nuclear Materials and Energy [89] and parts of this section are excerpts from this manuscript.

4.2.1 Experimental Results and Discussion

The evolution of the erosion yield of FeW (1.5 at% W) model films and pure Fe films with increasing D fluence is measured in-situ for impact of 1000 eV/D ions under normal incidence and for 250 eV/D ions under three different impact angles $\alpha = 0°$, 45° and 60° with respect to the surface normal. Similar to the experiments on WN the QCM technique (cf. section 3.1) is used to determine the erosion rates, with the consequence that the target holder is heated to 465 K. As target 675 nm thick iron-tungsten (FeW) films with a W concentration 1.5 at% W and pure iron (Fe) films for comparisons were used. After preparing the films at the IPP in Garching, RBS analysis confirmed the 1.5 at% W for the FeW films and showed an impurity content of 1.5 at% O and an oxide layer at the surface, the Ar impurities stayed below
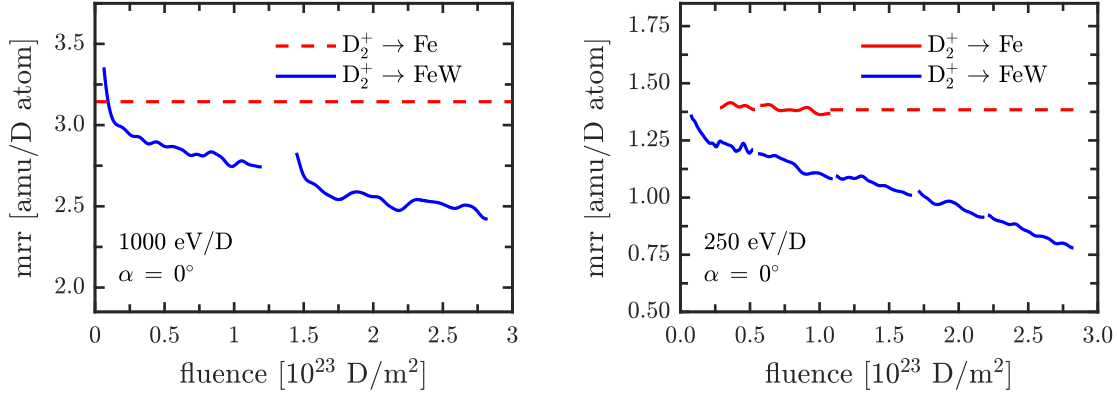
Figure 4.8: Evolution of the mass removal rate (mrr) of FeW (1.5 at% W) and pure Fe films as a function of the applied D fluence for irradiation with 1000 eV/D (left) and 250 eV/D (right) under normal impact ($\alpha = 0°$). For low fluences the mass removal rate for FeW is close to the value of pure Fe. With increasing fluence a significant reduction of the FeW mrr is observed. This decrease continues to high fluences without any sign for saturation. Data already published in [89].

detection limit (cf. section 3.1.5). To irradiate the targets the Perkin Elmer sputter gun producing a D_2^+ ion beam with a typical flux of $10^{18}\,\mathrm{m}^{-2}\mathrm{s}^{-1}$ was used. For a detailed description of the ion source see section 3.1.6.

Experimental results for irradiation under normal incidence ($\alpha = 0°$) at $250\,\mathrm{eV/D}$ and $1000\,\mathrm{eV/D}$ are shown in figure 4.8. For both measured energies, at the lowest D fluences the mass removal rate for FeW (blue curve) is comparable to the mass removal rate of pure Fe (red curve). With increasing fluence the mass removal rate for pure Fe (only measured at $250\,\mathrm{eV/D}$ as a function of the D fluence) does not change, but a significant reduction of the mass removal rate with fluence can be observed for FeW. The discontinuities notable in the curves correspond to scheduled interruptions, e.g. for monitoring the ion current, performing other check measurements and/or pausing the measurements during night. The observed reduction of the erosion yield is also consistent with results reported by Sugiyama et al. for the same FeW model films [38], where even at $1000\,\mathrm{eV/D}$ a clearly visible reduction of the sputtering yield was observed.

RBS analysis (performed by Oberkofler at the IPP in Garching) [96] of the samples before and after the ion bombarded with $1000\,\mathrm{eV/D}$ are in agreement with [38] and also show that the W surface concentration increases with the applied D fluence due to preferential sputtering of Fe.

Since in a fusion reactor normally the ions do not hit a surface under normal incidence, further measurements were performed at $250\,\mathrm{eV/D}$ for oblique incident ion impact
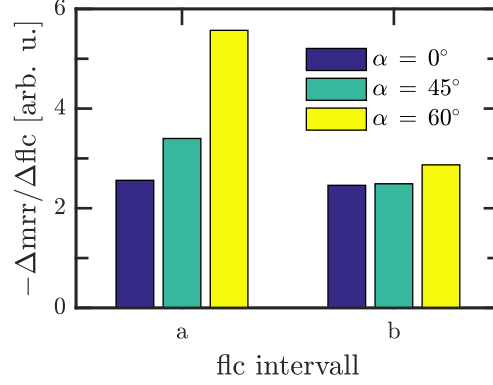
Figure 4.9: (a) and (b) are the mean slope of the mass removal rate (mrr)-curve measured at $250\,\text{eV/D}$ for 3 different impact angles ($0°$, $45°$ and $60°$) at fluences between 0 and $1 \cdot 10^{23}\,\text{D/m}^2$ (a) and at fluences between $2 \cdot 10^{23}\,\text{D/m}^2$ and $3 \cdot 10^{23}\,\text{D/m}^2$ (b). Data already published in [89].

($\alpha = 45°$ and $60°$). The influence of the incidence angle on the reduction of the erosion yield can be seen in figure 4.9, were the mean slope of the mass removal rate (mrr)-curve measured for fluences between 0 and $1 \cdot 10^{23}\,\text{D/m}^2$ (a) and fluences between 2 and $3 \cdot 10^{23}\,\text{D/m}^2$ (b) is shown for the respective impact angle. For the fluence interval between 0 and $1 \cdot 10^{23}\,\text{D/m}^2$ (a) the mean (negative) slope of the mrr-curve (i.e. its derivative) increases with incidence angle. This means that in this fluence range the reduction of the mass removal rate is more pronounced for $\alpha = 45°$ and $\alpha = 60°$ as compared to $\alpha = 0°$.

This behaviour can be explained by the general trend in sputtering, that yields tend to increase with ion angle of incidence up to a certain maximum (typically at around $60° - 85°$ depending on impact energy and surface flatness). This increase in (Fe) sputtering yield in turn accelerates the development of a W enriched surface. For rough surfaces, however, the dependence of the sputtering yield on ion impact angle is considerably reduced, since the yield has to be averaged over a distribution of local impact angles [55, 56]. For higher fluences between 2 and $3 \cdot 10^{23}\,\text{D/m}^2$ the mean slopes of the mrr-curves become nearly equal for the three different impact angles, shown in figure 4.9 (b).

To check, whether this is due to a change in surface topography (e. g. roughening/smoothening, ripple formation) the angular dependence of the sputtering yield was measured after certain fluence steps (1, 2 and $3 \cdot 10^{23}\,\text{D/m}^2$) applied at the respective nominal impact angle α. Furthermore investigation of the surface topography of the FeW films were done before and after irradiation using an atomic force microscope (AFM). Figure 4.10 shows the influence of the irradiated fluence on the angular dependence of the sputtering yield. For all three impact angles the angular dependence is very low, while SDTrimSP (assuming a perfectly flat surface) shows a

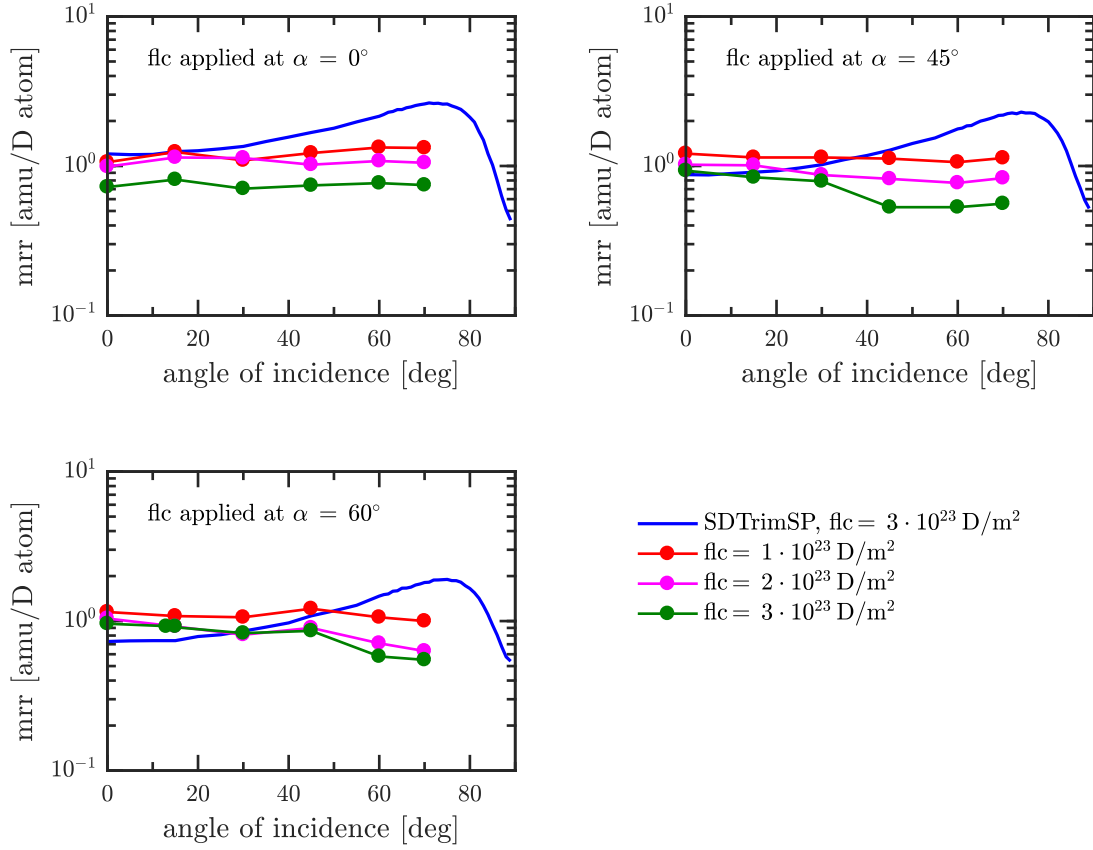**Figure 4.10:** Angular dependence of the D sputtering yield for $250\,\mathrm{eV/D}$ measured after the FeW target was irradiated with certain fluence (flc) steps (1, 2 and $3\cdot 10^{23}\,\mathrm{D/m^2}$) at the respective nominal impact angles $\alpha = 0°$, $45°$ and $60°$ (counted from the surface normal). The blue curve shows the simulated (SDTrimSP) angular dependence after a flc of $3\cdot 10^{23}\,\mathrm{D/m^2}$.

Figure 4.11: AFM images of the surface topography of FeW ($1.5\,\text{at}\%$ W) films, (a) as deposited, (b)-(d) eroded with $\approx 3 \cdot 10^{23}\,\text{D/m}^2$ at $250\,\text{eV/D}$ ions at different angles of incidence ($0°$, $45°$, $60°$). The arrow indicates the beam direction. Figure published in [89].

clear enhancement of the sputtering yield with a maximum around $70°$. Nevertheless for the highest applied fluence ($3 \cdot 10^{23}\,\text{D/m}^2$, green curve) one can see that the minimum of the angle dependence is reached for the nominal irradiation angle.

Investigations of the surface topography were done with a Cypher atomic force microscope (AFM) from Asylum Research in tapping mode under ambient conditions. As probes, silicon nanosensors SSS-FMR with a resonance frequency of $75\,\text{kHZ}$ and a spring constant of $2.8\,\text{N/m}$ were used. With a tip radius $< 5\,\text{nm}$ these super sharp tips are well able to resolve nanoscale features.

Typical AFM images of the FeW model films are displayed in figure 4.11. A freshly prepared FeW film (figure 4.11 (a)) shows a grain-like structure with a grain length of typically $150-200\,\text{nm}$ and a grain height of $10-15\,\text{nm}$. A root mean square roughness of typically $3.2\,\text{nm}$ can be derived (using Gwyddion [97]) from the AFM measurements (c.f. table 4.1). The images in figure 4.11 (b) – (d) are obtained after irradiating the FeW films at $250\,\text{eV/D}$ with a total D fluence of $3 \cdot 10^{23}\,\text{D/m}^2$ under the respective impact angle. The surface topography after normal incidence irradiation is shown in

Table 4.1: Root mean square roughness (RMS) of the corresponding AFM image in figure 4.11. Determined with Gwyddion 2.45 [97]

	as deposited	$\alpha = 0°$	$\alpha = 45°$	$\alpha = 60°$
RMS roughness	3.2 nm	8.6 nm	6.4 nm	10.5 nm

figure 4.11 (b). The surface still vaguely resembles the original grain-like structure, but the initially continuous grains are now broken up into individual nanodots and the root mean square roughness has more than doubled (c.f. table 4.1). For 45° impact angle (figure 4.11 (c)) the nanodots are slightly elongated in the direction of the incident ion beam and arranged quasi-periodically, while for 60° impact angle (figure 4.11 (d)) a ripple-like surface morphology develops. A comparison with relevant literature shows that in this case so-called perpendicular mode ripples (PeMR) are formed, where the ripples are oriented parallel to the ion beam direction, i.e. the wave vector of the ripples is perpendicular to the ion beam [98]. The formation mechanism of ripples and nanodots relies on a natural self-organization mechanism that occurs during the erosion of surfaces, which is based on the interplay between roughening induced by ion sputtering and smoothing due to surface diffusion (for details see e.g. [99–102]). All irradiated films (including the film irradiated under normal impact) show a root mean square roughness 2 to 3 times as high as the roughness of the originally prepared film. This nano-scale roughness, however, might have been too small to be resolvable in the SEM measurements presented in [38], which led to the conclusion, that no significant development of the surface topography takes place with fluence. Since surface roughening effects are not yet included in SDTrimSP simulations, this could at least in part explain the discrepancy between experiment and simulation reported in [38].

With the findings from the AFM investigations and recent SDTrimSP-2D[1] [103] simulations by von Toussaint et al. which have shown that the W surface distribution has a decisive influence on the sputter yield reduction as well as on the surface structure [104], a speculative explanation for nearly equal mrr-curve slopes for high fluence (c.f. figure 4.9 (b)) can be given. In the simulations it could be shown that for an initially flat target with a homogeneous W distribution (simulated with tungsten blocks of size 5×5 Å embedded in a Fe matrix) a flat surface layer with increased W concentration is formed, while for tungsten blocks with a size of 30×30 Å a strong built-up of surface morphology with increasing fluence is shown. The surface obtained by the simulation is very similar to the nanodot structure observed under normal ion impact. The individual dots are covered by tungsten layers and the gaps in between show a

---

[1]New program version based on SDTrimSP, were the target is resolved in two dimensions (SDTrimSP-2D), allowing to account for effects of roughness on the scattering and sputtering and to model dynamical morphological changes

significantly lower W surface concentration [104]. Considering that those parts of the surface are also preferably eroded, where the local impact angles were close to the maximum of the angular dependence of the sputtering yield, a surface can build up where these dots become elongated or form the observed ripple structures depending on the impact angle. After the structure of the surface morphology has been completed, the enrichment proceeds then at the same rate for the three different nominal impact angles. With the consequence that for all impact angles almost the same mrr-curve slope is measured at high fluences.

4.2.2 Summary

Erosion studies on FeW models systems (containing 1.5 at% W) for steels like EUROFER containing high-Z elements such as W, were performed under well defined conditions using a molecular D ion beam. For both, projectile energies of 1000 eV/D and 250 eV/D fluence dependent sputter experiments were carried out. While for the first one only normal impact angles were studied, the angle of incidence was varied ($\alpha = 0°$, $45°$ and $60°$) for 250 eV/D. The evolution of the erosion yield with D fluence was monitored by a quartz crystal microbalance up to a total fluence of $3 \cdot 10^{23}$ D/m^2. In addition the samples topography and roughness before and after irradiation were studied by using an AFM.

In conjunction with the findings reported in references [38] and [104] the following picture emerges. Prolonged irradiation changes the surface composition of the FeW targets due to preferential sputtering of Fe and leads to W enrichment at the surface. The W enrichment shown in [38] could be confirmed by the RBS analysis [96] of our target which was irradiated at 1000 eV/D. It can be correlated with the decreasing sputtering yield (mass removal rate) for increasing D fluence observed by the in-situ erosion monitoring during irradiation. For the 250 eV/D irradiation under oblique impact angles the reduction of the mass removal rate is initially more pronounced as compared to normal incidence, but the differences vanish for fluences $> 2 \cdot 10^{23}$ D/m^2. Looking for an explanation for this effect high resolution AFM images showed that also the surface morphology changes a lot during prolonged ion irradiation resulting in a significant surface roughening and (depending on ion impact angle) formation of nanodots or nano-ripples. This gives the conclusion that after the change of the surface morphology has been completed the W enrichment proceeds at the same rate for all impact angles.

4.3 Characterising the QCM Catcher Setup

So far, sputter experiments using the QCM technique have been carried out with thin target layers directly deposited onto the quartz crystal [62, 64–66, 105]. However, the use of thin layers limits the possible experiments, as some target materials cannot easily be deployed in such a form. For example, the stoichiometry of component targets may change when deposited as a thin layer by sputter deposition or evaporation. Also the surface roughness or the crystalline structure of the target layers can hardly be controlled. In order to overcome these limitations and to open the possibility of using any solid material or even liquids as a sputter target, a new experimental setup was designed and presented in section 3.3, in which the QCM acts as a catcher for sputtered material. The new QCM catcher setup benefits from the precision and experience of the QCM technique and the versatility of using almost any target.

As described in detail in section 3.3.2, the relation between the target yield Y_{tar} and the experimentally determined catcher yield Y_c can be expressed by the ratio g. The ratio g contains on the one hand the information about the setup geometry (characterised by the parameters α, Δx and d), the quartz's sensitivity s to a mass change, the impinging ion current density j, the sticking coefficient C_{st} of the sputtered particles at the catcher as well as the angular distributions of the sputtered f_{sp} and reflected particles f_r. While the former are known, assumptions about the angular distributions have to be made, one possibility to obtain them is to use the simulation code SDTrimSP. The sputtering yields and angular distributions simulated with SDTrimSP are in general in a very good quantitative agreement with experimental data [81, 82]. Nevertheless it should be noted that SDTrimSP assumes an amorphous, perfectly flat target, which however, does not generally agree with the actual experimental conditions.

In order to test the catcher-QCM configuration and the possibility of reconstructing the sputter yield by using the simulated angular distributions, proof of principle measurements were performed using a second QCM (target-QCM) instead of a regular sputter target. The use of two QCMs allows to measure the mass loss at the target and the mass increase at the catcher simultaneously and thus to compare the measured with the simulated ratio g. For this purpose, a well known projectile target combination Ar^+ on Au and Ar^+ on Fe was used, since for both combinations a large number of literature data is available.

The results presented in this section for Au have been published in [63] and parts of this section are excerpts from this publication.

4.3.1 Experimental Conditions

In order to carry out the proof of principle measurements, a quartz crystal coated with an Au or Fe layer was used for the catcher- as well as for the target-QCM in order to ensure consistent sticking conditions during the measurement. The 450 nm thick Au layers were prepared at the Institute of Solid State Physics (TU Wien) using a vapor deposition technique, while the 400 nm thick Fe layers were prepared at the IPP in Garching using a magnetron-sputter device (c.f. section 3.1.5). The ion beam for irradiating the target-QCM is produced in a 14.5 GHz all permanent magnet ECR ion source [75] and then mass over charge selected by a sector magnet. Deflection plates and lenses focus and guide the ion beam into the target chamber, where it is scanned over the quartz crystal's active area using two pairs of deflection plates (for details see section 3.1.6 and references [64, 65]). Additionally, in order to determine the total number of incoming ions the scanned ion beam is controlled with a set of multiple apertures (Ø 2, 3, 4, 7 mm) that can be moved into the beam's path, directly in front of the target layer. The ion current is then measured using a Faraday cup at the target's position (c.f. section 3.3) before and after the irradiation of the target. Similar to the previous QCM experiments with one QCM, the measurements start with a beam off phase to check the correct function of the QCM followed by a beam on phase where the slopes are determined and ends again with a beam off phase.

4.3.2 Sputtering Au by Ar$^+$ Ions

The first experiments where conducted with 2 keV Ar$^+$ ions, irradiating an Au target. For 2 keV Ar$^+$ impact under normal incidence on a polycrystalline Au surface a large compilation of literature data gives a sputtering yield of approximately 5 ± 2 atoms/ion [57], which is consistent with previous measurements using the standard QCM technique [65, 106]. For impact angles close to 60°, the sputtering yield increases approximately by a factor of 1.5 [48, 107]. The sputter threshold for self-sputtering of Au is close to 10 eV. Since the kinetic energy of the sputtered particles is well below 10 eV, with a maximum probability around 1 eV [48, 61, 88], self-sputtering of sputtered particles from the target at the catcher can be neglected. At this low kinetic impact energy (≈ 1 eV) at the catcher the sticking coefficient for Au atoms on a Au surface is very close to 1 [59, 60]. For this reason in the analysis no self-sputtering and a sticking coefficient of 1 can be assumed.

Figure 4.12 (a) – (c) shows the measured and simulated ratio $g = Y_c/Y_{tar}$ for a variety of different catcher positions (characterised by Δx and d) and ion impact angles α (c.f. figure 3.8). Figure 4.12 (d) – (f) compares the sputtering yield directly measured
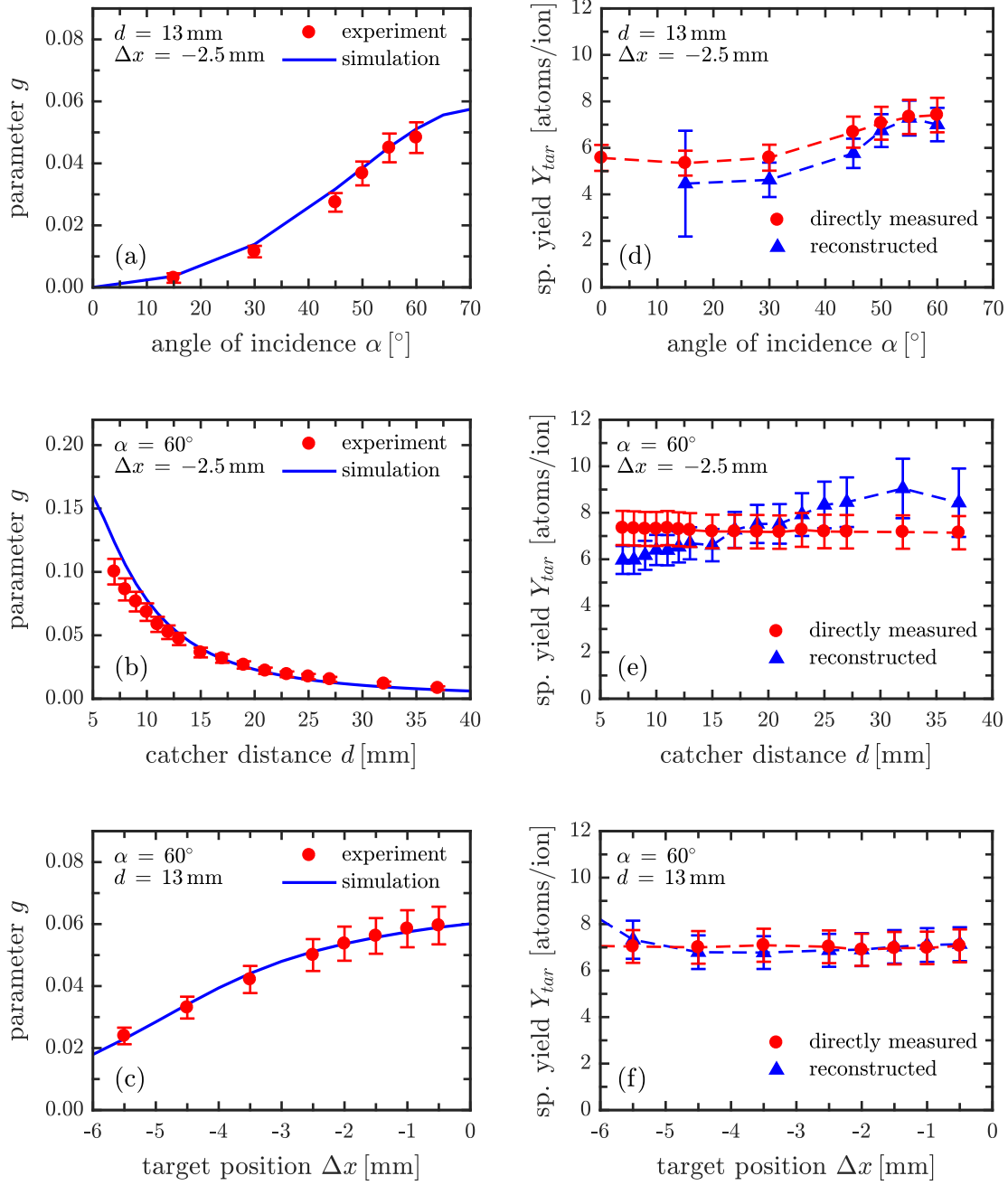
Figure 4.12: Au target-catcher yield comparison for $2\,\text{keV Ar}^+$ ions: The simulated (blue) and measured (red) ratio g (a-c) and the measured (Y_{tar}) and reconstructed ($Y_{tar} = Y_c/g$) target sputtering yield (d, e) is shown for a variety of different catcher positions (characterised by Δx and d) and ion impact angles α. Figure published in [63].

with the target-QCM (using equation 3.5) with the sputtering yield reconstructed from the data of the catcher-QCM using the simulated ratio g.

Figure 4.12 (a) shows the behaviour of the ratio g for different angles of incidence α on the target. In general, the total sputtering yield increases with the impact angle up to a maximum between 60° and 80°, since more energy is deposited in the vicinity of the surface. Thereby, the angular distribution of sputtered atoms shows a maximum in a cone at 45° to 60° [58], which is also reproduced by SDTrimSP simulations. As a result, hardly any particles are sputtered in the direction of the catcher at small incidence angles α (0° − 15°). This results in a large uncertainty for the reconstructed target sputtering yield presented in figure 4.12 (d). In figure 4.12 (b) the distance d between the catcher and the ion beam is varied. With increasing distances d the ratio g decreases steadily, since the catcher-QCM registers sputtered particles from a smaller solid angle, because it is further away from the target. This leads to an increasing error of the reconstructed yield for distances larger than 20 mm since less material is collected (see figure 4.12 (e)). In addition, for small distances (lower than 10 mm) a modest deviation between the simulated and measured values can be observed. Possible reasons for this behaviour are surface roughness or inhomogeneities in the ion current profile influencing the angular distributions of sputtered and reflected particles. The ratio g and the reconstructed target sputtering yield Y_{tar} for a variation of the target position Δx is shown in figure 4.12 (c) and (f), here for a wide range a good agreement between the simulation and the experiment can be seen. If the displacement Δx between catcher and target becomes larger more sputtered atoms miss the catcher resulting in a smaller signal, because the catcher-QCM is moved away from the maximum of the sputtered particle distribution.

Given that there is no free fitting parameter involved in this comparison, the agreement between the simulated and experimental data can be considered as excellent. For future measurements figure 4.12 provides the basis to optimise the ideal parameter combination of the catcher distance d, the displacement Δx and the angle of incidence α, where $d = 15$ mm, Δx close to 0 and $\alpha = 60°$ have been found to be a very good choice.

4.3.3 Sputtering Fe by Ar$^+$ Ions

Similar experiments as shown in section 4.3.2 were also carried out with Fe films, which were irradiated with 1 keV Ar$^+$ ions. For 1 keV Ar$^+$ impact under normal ion impact literature data give a sputtering yield of approximately 1 − 1.5 atoms/ion [57]. This is consistent with sputtering yield measurements conducted within this thesis (see figure 4.14) using the standard QCM technique. For oblique ion impact SDTrimSP and
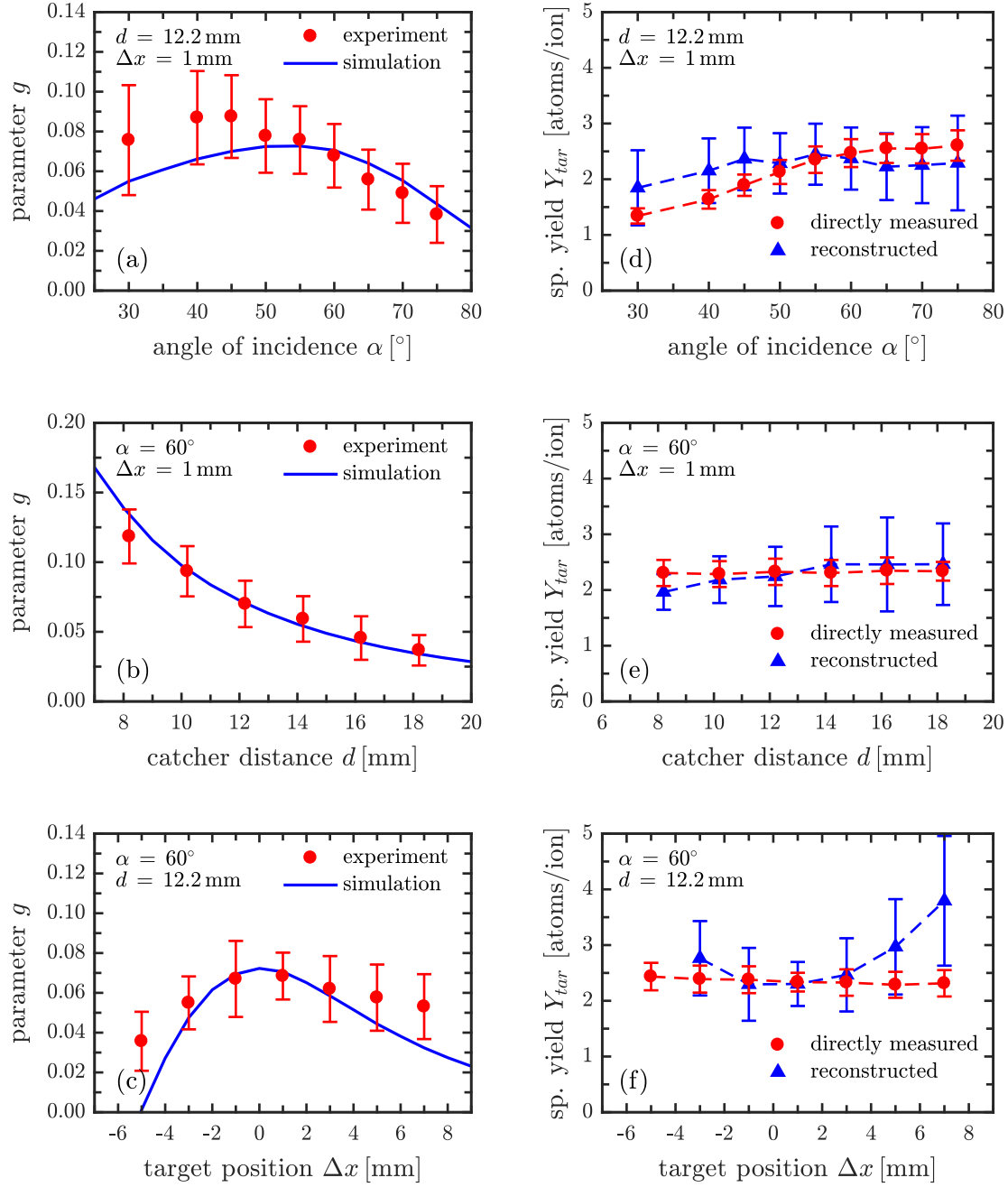
Figure 4.13: Fe target-catcher yield comparison for $1\,\mathrm{keV\,Ar^+}$ ions: The simulated (blue) and measured (red) ratio g (a-c) and the measured (Y_{tar}) and reconstructed ($Y_{tar} = Y_c/g$) target sputtering yield (d, e) is shown for a variety of different catcher positions (characterised by Δx and d) and ion impact angles α.
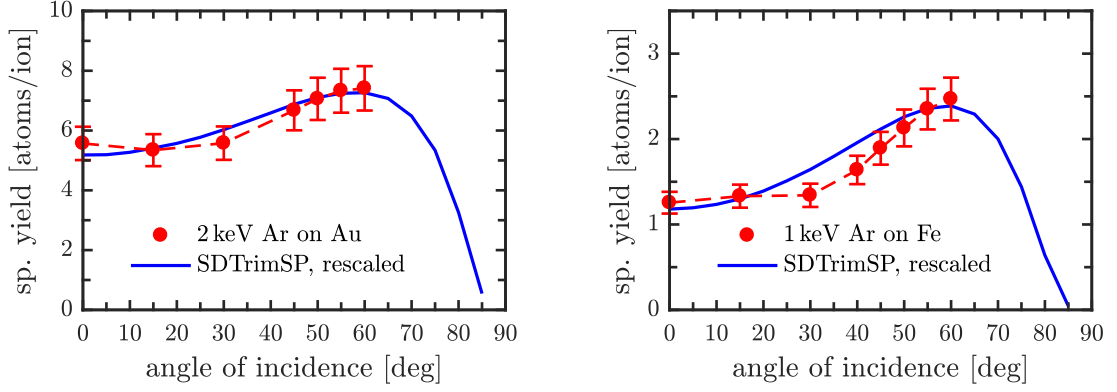
Figure 4.14: Measured and simulated (SDTrimSP) angular dependent sputtering yield for Au and Fe under 2 respectively 1 keV Ar^+ ion impact. The SDTrimSP values are rescaled to fit to the sputtering yields measured using the QCM technique.

experiments show an increase of the sputtering yield by a factor of approximately 2 at impact angles close to 60° [48]. Similar to Au, the sputter threshold for self-sputtering of Fe is close to 10 eV. Considering the kinetic energy of the sputtered particles around 1 eV [48], self-sputtering can be neglected. Since Fe has a metallic surface similar to Au, the sticking coefficient is assumed to be 1 for Fe atoms on a Fe surface.

Analogue to figure 4.12, figure 4.13 shows the measured and simulated ratio g and the directly measured with the reconstructed sputtering yield for the Fe films. The varied parameters are the catcher position (characterised by Δx and d) and the ion impact angle α.

Figure 4.13 (a) and (d) shows the ratio g and the reconstructed target sputtering yield Y_{tar} for different angles of incidence α on the target. While for Au the agreement between the simulated and experimental measured ratio g was excellent, for Fe a deviation between these two data sets is observed at impact angles below 50°. Experimentally more material is caught by the catcher than predicted by the simulation. Nevertheless, the simulated ratio g is still within the error bars of the experimental values. The distance d between the catcher and the ion beam is varied in figure 4.13 (b) and (e). Here, the experimental data agree nicely with the simulation. The ratio g follows a $\approx C/d^2$ behaviour. Similar to the Au results, the error bars of the reconstructed target sputtering yield Y_{tar} increases with distance d, since less material is collected by the catcher-QCM. For different target positions Δx the ratio g and the reconstructed target sputtering yield Y_{tar} is shown in figure 4.12 (c) and (f) . While the experiments with the Au film show a good agreement between the simulation and the experiment, a significant difference is visible for the Fe film. The measured ratio g is clearly above the simulated values for target positions Δx below ≈ -4 or above
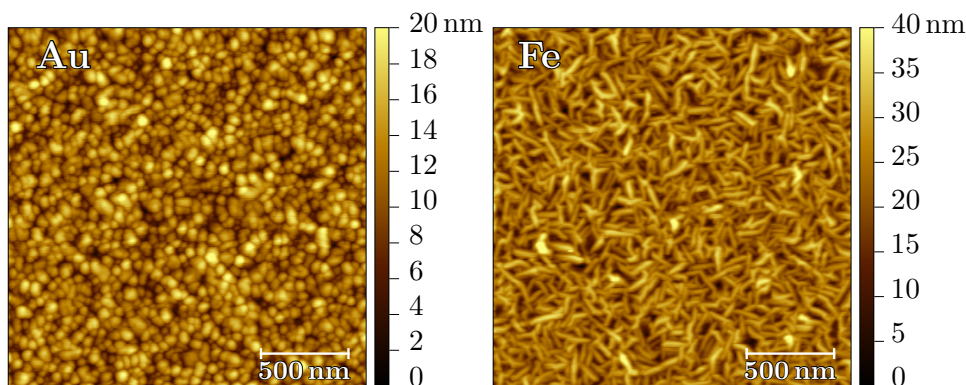
Figure 4.15: AFM images of the surface topography of the freshly prepared Au (left) and Fe (right) films.

$\approx 5\,\mathrm{mm}$. This means that more particles are actually caught by the catcher than expected by the simulated distributions. A possible interpretation of the described behaviour is that the angular distributions of the sputtered and reflected particles are in fact broader then in the simulation. A higher surface roughness in the experiment is likely the reason since SDTrimSP simulates a perfectly flat surface.

4.3.4 Discussion

When comparing the results for Au and Fe it is striking that the agreement between the simulations and the experimental data is excellent for Au, whereas for Fe deviations are found. To discuss this in more detail, figure 4.14 shows the measured and simulated angular dependence of the sputtering yield for Au and Fe under Ar^+ ion bombardment. For Au a quantitative agreement is given over the whole measured angular range. For Fe the measured sputtering yield is below the simulated one between 15° and 45°. A possible explanation for the observation could be a rougher surface topography of the Fe film.

AFM investigations of the surface topography of the Au and Fe films were done with a Cypher atomic force microscope (AFM) from Asylum Research in tapping mode. The vapour deposited Au surface, figure 4.15 (left), shows an island growth structure where the diameter of the certain islands is between $20 - 50\,\mathrm{nm}$. The root mean square (RMS) roughness of the in figure 4.15 shown Au surface is $2.9\,\mathrm{nm}$, determined with Gwyddion [97]. The surface topography of the sputter deposited Fe film is shown in figure 4.15 (right). Similar to the FeW films (c.f. section 4.2), a grain like structure with a typical grain length of $150-200\,\mathrm{nm}$ and a grain height of $10-15\,\mathrm{nm}$ is observed. As RMS roughness of the Fe film shown in figure 4.15 (right) a value of $5.2\,\mathrm{nm}$ was

evaluated, which is 1.8 times larger than the RMS roughness obtained for the gold film. This, however, represents a huge difference on surface structure.

Combining the angular dependent sputter yields (figure 4.14) and the AFM images (figure 4.15), the hypothesis is supported, that the observed difference in the ratio g for the Fe target is caused by the surface roughness. SDTrimSP simulates the sputtering yield as well as the angular distributions of sputtered and reflected particles for a perfectly flat surface. In the experiment, however, the target surface has a certain roughness which can lead to deviations from the simulated values. As discussed in section 2.2.2 both, the sputtering yield and the angular distribution of sputtered particles are influenced by the surface topography. The local angle of incidence can deviate from the nominal one and shadowing and redeposition can occur. The surface topography of the investigated Au target in not only flatter but also shows very different structure than the Fe film. The Au film is sufficiently flat to achieve a good agreement between the experiment and simulation, whereas the Fe surface is rather rough with the result that the observed deviations between experiment and simulation occur.

4.3.5 Summary

In section 3.3 a new experimental setup for the indirect determination of sputter yields was presented. In this setup a QCM is placed beside the sputter target acting as a catcher for sputtered material. In order to determine the target sputtering yield indirectly with the measured catcher yield, the actual geometry and all relevant processes have been taken into account. Thereby knowledge about the energy and angular distributions of sputtered and reflected particles are necessary which can be derived from the Monte Carlo code SDTrimSP. To validate this approach proof of principle measurements with the projectile-target combination Ar^+ on Au and Fe were performed, in which a second QCM with a Au/Fe layer on top acting as a target allows an independent measurement of the sputtering yield. The experiments with the two different targets proved the ability of the new setup to provide absolute sputtering yields. For the smooth Au surface the consistency with the simulations is excellent. Depending on surface roughness differences between experiment and simulation can occur as seen in the experiment with the Fe film. Here, a larger value g is measured for small impact angles α and larger displacements for the target position Δx, which is explained by broader angular distributions of the sputtered and reflected particles, caused by a higher surface roughness. Nevertheless, for the rough Fe surface still a good agreement with the simulation is given for impact angles $\alpha > 50°$ and target positions Δx between -2 and $3\,mm$.

Future sputter yield measurements at the Institute of Applied Physics will therefore no longer be limited to thin layer targets pre-deposited on a QCM [64]. Experiments with a wide variety of targets (single crystals, compounds and alloys, even liquids) under a range of experimental conditions (effect of temperature or surface morphology) not possible so far. The erosion of wall material for nuclear fusion devices or space weathering effects on lunar or planetary surfaces by ions typical for the solar wind can now be studied on real samples instead of model systems. Also the topography of the surface can be taken into account with SDTrimSP-2D simulations considering the experimental surface topography, which should improve the agreement for rough targets. When indirectly measuring the sputtering yield, knowledge of the angular distribution of the sputtered material is necessary to reconstruct the absolute sputtering yield. Compared to other methods used for determining sputtering yields like Rutherford backscattering analysis (RBS) or a weighing technique, the new method is not limited to thin layer targets and can obtain the sputtering yield in situ and in real time.

5 Conclusions and Outlook

When energetic particles impinge on surfaces a variety of interaction phenomena, like erosion (i.e. sputtering), roughening or smoothing of the surface, changing of the surface composition, reflection or implantation of the projectile, emission of electrons, photons and other secondary particles etc., occur. Sputtering of surfaces due to ion impact is not only important for multiple applications, like thin layer deposition, surface etching or surface analytic techniques. It is also of major concern regarding the erosion of wall material of nuclear fusion devices, or in space weathering where lunar or planetary surfaces get eroded by solar wind ion impact.

With regard to a future fusion power plant, the investigation of erosion processes by energetic particles is of great importance to realise a first wall, which can withstand particle bombardment long enough to operate such a fusion reactor economically [16]. Plasma-wall-interaction processes of fusion relevant projectile target combinations have therefore been studied under controlled laboratory conditions using a highly sensitive quartz crystal microbalance (QCM) technique. A film of fusion relevant target material is applied to one side of the QCM and bombarded with well defined projectiles. The mass change, caused by the ion impinging at the target layer, was determined by measuring the quartz crystal's resonance frequency in situ and in real time.

In a future fusion reactor impurity seeding into the plasma edge is required in order not the exceed the heat flux that can be managed by the divertor. The seeded impurities emit line radiation while being subsequently ionised, spreading the power flux onto a larger area of the vessel surface [26]. N seeding with feedback control is now a standard operational scenario at ASDEX Upgrade and being an effective coolant at the plasma edge in the 10 eV rage [27, 28]. However, for the use of N in combination with a W divertor, the formation of WN surface layers is observed. While the interaction between N and W surfaces is well investigated [31–33], little is known about the interaction of WN with D plasmas. Therefore, the erosion of well prepared WN and W (for comparison) films was studied under D ion bombardment with a typical flux of $10^{18}\,\mathrm{m^{-2}s^{-1}}$ at 500 and 1000 eV/D. For both kinetic energies, the erosion rate for

WN was initially higher than for pure W. This enhancement decreased with increasing fluence, reaching the steady state erosion yield of pure W, which does not change with fluence. For $1000\,\text{eV/D}$ bombardment, steady state conditions are reached at a fluence of about $0.6 \cdot 10^{23}\,\text{D/m}^2$. For the $500\,\text{eV/D}$ bombardment, $0.2 \cdot 10^{23}\,\text{D/m}^2$ were sufficient to reach steady state conditions. Comparisons to SDTrimSP simulations [81] showed that the measured mass removal rate for WN follows the same trend as the N surface concentration with D fluence. However, the transient enhanced erosion rate for WN could not be completely reproduced by simulation, indicating that not enough N is removed from the surface near regions in the simulation. As possible mechanism for the enhanced N loss in the experiment, irradiation-induced diffusion was suggested.

In future fusion power plants, a stable and quiescent plasma is assumed, where the lifetime of the plasma facing components (PFCs) is dominated by plasma induced erosion due to sputtering. The erosion yield of high-Z materials like W is considerable lower than the erosion yield of low- or mid-Z materials like Fe, at the expected reactor conditions [34]. W containing steel e.g. EUROFER [36], make use of this difference in the sputtering yield, because preferential sputtering leads to a W surface enrichment [38]. This surface enrichment is accompanied by a reduction of the erosion yield [37], which makes these steels a (technologically and economically) promising alternatives to a full W armour for recessed areas in a future fusion reactor [34,35]. This behaviour was demonstrated in recent erosion studies on heavy element containing steels and iron-tungsten (FeW) model films with different W concentrations, where the erosion rate decreased roughly by $1-2$ orders of magnitude with increasing fluence [37,38]. While these experiments showed a strong correlation between erosion yield and W surface enrichment, there is still a quantitative discrepancy between experimental observations and simulation remaining, where a significantly higher W enrichment is predicted than found in RBS measurements. A possible explanation are experimental and simulation uncertainties [38]. To gain a better understanding of this W surface enrichment process, fluence dependent sputter experiments were carried out using well-defined FeW films containing $1.5\,\text{at\%}$ W, as model system for EUROFER and Fe films for comparison. The erosion yield of these films was measured for D ion impact with a typical flux of $10^{18}\,\text{m}^{-2}\text{s}^{-1}$, at $1000\,\text{eV/D}$ under normal incidence and $250\,\text{eV/D}$ for three different impact angles $\alpha = 0°$, $45°$ and $60°$ with respect to the surface normal. The evolution of the erosion yield with D fluence was monitored by a QCM up to a total fluence of $3 \cdot 10^{23}\,\text{D/m}^2$. In addition, the samples topography and roughness of the FeW films bombarded at $250\,\text{eV/D}$ were studied before and after irradiation by an AFM. For both kinetic energies a decreasing sputtering yield with increasing D fluence was observed, which can be correlated to a W surface enrichment measured with Rutherford backscattering analysis (RBS). For the FeW films irradiated at $250\,\text{eV/D}$, an initially more pronounced reduction of the erosion yield was measured for oblique ion impact $\alpha = 45°$ and $60°$. But the differences

vanished for fluences $> 2 \cdot 10^{23}\,\text{D/m}^2$ reaching the value for normal incidence. To explain this effect high resolution AFM images were recorded, which showed that also the surface morphology changed due to the ion irradiation resulting in a significant surface roughening and depending on ion impact angle, formation of nanodots or nanoripples. This gives the conclusion that when the change of the surface morphology has been completed, the W enrichment proceeds at the same rate for all impact angles. In order to disentangle the effect of surface roughness / ripple formation on the dynamic erosion behaviour and the effect of W surface enrichment follow up measurements are planned using pure Fe films deposited on super-polished SC cut quartz crystals. The comparison between the Fe and FeW investigations should then clarify the influence of the surface topography on the erosion yield.

In addition to the studies on fusion-relevant surfaces, a new experimental setup based on a QCM for indirect determination of sputter yields was developed. In the new setup a QCM is placed beside the target holder acting as a catcher for material sputtered from the target surface. In the existing QCM method [64, 65], the material to be examined has to be applied to the QCM in form of a thin layer. Thereby, the use of thin films limits the possible experiments, as some target materials cannot easily be deployed in such a form. The new setup is supposed to overcome the restrictions of the existing QCM technique, while benefiting from the precision of the QCM and the possibility to determine erosion yields in situ and in real time. All relevant processes and parameters to determine the target sputtering yield indirectly with the measured catcher yield were taken into account and expressed with the ratio $g = Y_c/Y_{tar}$ between the measured catcher yield and the target yield. The ratio g contains on the one hand all the informations about the experimental setup (geometry and QCM) as well as the angular distributions of the sputtered and reflected particles. While the informations about the experimental setup are known, assumptions about the angular distributions of sputtered and reflected particles have to be made. One possibility to obtain them is to use the simulation code SDTrimSP. In order to validate the new catcher-QCM configuration and the possibility of indirectly measuring absolute sputter yields by using simulated angular distributions, proof of principle measurements were performed using a second QCM (target-QCM) instead of a regular sputter target. The use of two QCMs allowed a direct comparison between the reconstructed sputtering yield using the signal form the catcher-QCM and the directly at the target-QCM measured sputter yield. The result obtained by these measurements using a well known projectile target combination Ar^+ on Au and Ar^+ on Fe could demonstrate the feasibility of determining absolute sputtering yield with the new catcher-QCM setup.

From now on sputter yield measurements at the Institute of Applied Physics will therefore no longer be limited to thin layer targets pre-deposited on a QCM [64], making a variety of new targets available. Currently new experiments using Mercury and Moon analogues as target are planed, to enhance the understanding of surface

sputtering by solar wind ions. This will be used to improve theoretical models of the Mercury's and Moon's exosphere formation so that more insight about their surface composition can be obtained.

Acronyms

AFM atomic force microscope

ASDEX Upgrade axial symmetric divertor experiment upgrade

AUGUSTIN Atom- und Grenzflächenphysikalische Untersuchungen bei STößen mit Ionen und Neutralteilchen; laboratory at the TU Wien

CFC carbon fiber-reinforced composites

DEMO DEMOnstration power station

ECR electron cyclotron resonance

ELM edge localised mode

FeW iron-tungesten

flc fluence

IEA International Energy Agency

IPP Max Planck Institute for Plasma Physics

ITER A large tokamak constructed in Cadarache, France. Former abbrivation for: international thermonuclear experimental reactor , now just the Latin word for 'the way' (to fusion)

JET joint European torus

mrr mass removal rate

PeMR perpendicular mode ripples

PFC plasma facing component

PWI plasma wall interaction

QCM quartz crystal microbalance

RBS Rutherford backscattering analysis

RMS root mean square

SC stress compensated

SDTrimSP further development of TRIM and TRIDYN where SD stands for static/dynamic and SP for sequential/parallel processing

SRIM stopping and range of ions in matter

stellarator derived form the possibility of harnessing the power source of the sun, a stellar object

TRIDYN on TRIM based dynamic version

TRIM transport of ions in matter

TOF-ERDA time-of-flight elastic recoil detection analysis

tokamak derived from the Russian words for toroidal chamber with magnetic field

W7-X Wendelstein 7-X , an experimental stellarator built in Greifswald, Germany

WEST tungsten (W) environment in steady-state tokamak

WN tungsten-nitride

Danksagung

*Ich bin dankbar, nicht, weil es vorteilhaft ist, sondern
weil es Freude macht.*
— Lucius Annaeus Seneca d.Ä. (55 v. - 40 n.Chr.),
röm. Schriftsteller u. Rhetoriker

Mit diesen letzten Zeilen in dieser Dissertation möchte ich mich noch bei all jenen
bedanken, die maßgeblich zum Erfolg dieser Arbeit und meinen Studienabschluss bei-
getragen haben. In den letzten Jahren habe ich viel erlebt und durfte eine Vielzahl
an neuen und spannenden Erfahrungen machen, die ich stets in guter Erinnerung
behalten werde.

Zuallererst geht mein Dank an meinen Betreuer und baldigen Doktorvater Friedrich
Aumayr. Danke Fritz, dafür, dass du neben deinen anderen Verpflichtungen jederzeit
ein offenes Ohr für etwaige Problemchen, sei es physikalischer oder allgemeiner Natur,
hattest. Du hast stets für ein angenehmes Arbeitsklima gesorgt und viel Verständnis
für diverse Späße und Blödeleien von uns gezeigt. Dank dir durfte ich auch Erfah-
rungen bei diversen Konferenzen sammeln und die dort zum Teil beinahe familiäre
Atmosphäre kennenlernen. Dabei hatte ich nicht nur die Möglichkeit, meine skifahre-
rischen Fähigkeiten zu verbessern, sondern auch meine Ergebnisse unter anderem in
Form eines eingeladenen Vortrags vor internationalem Publikum zu präsentieren.

Als nächstes möchte ich mich bei den Mitgliedern der Arbeitsgruppe Atom- und Plas-
maphysik bedanken. In den $3^1/2$ Jahren, die ich mittlerweile Teil dieser Arbeitsgruppe
bin, durfte ich mehrere Bachelor,- Projekt- und Diplomarbeiten betreuen. Ganz be-
sonders möchte ich dabei Reinhard Stadlmayr und Paul Szabo danken, ihr wart mir
beide eine große Hilfe bei diversen Messungen, Auswertungen und beim Rumschrau-
ben am Experiment.
Schmu, du warst stets hilfsbereit, großzügig und hast viel Geschick beim Arbeiten
mit der QCM an den Tag gelegt. Gemeinsam durften wir auf mehrere Messaufenthal-
te und Konferenzen fahren, wo du meistens schon ein tolles Freizeitprogramm, wie die
Wanderung in Aix en Provence, fürs Wochenende geplant hast. Da du nun ebenfalls

Dissertant bist und zum Teil meine Arbeit fortführen wirst, wünsche ich dir alles Gute und viel Spaß damit.

Paul, du hast schon bei deiner Bachelorarbeit sehr viel Selbstständigkeit und Geschick an den Tag gelegt. Du warst mir eine große Hilfe bei den ersten Messungen mit dem neuen Catcher-Setup und hast mit deiner Begeisterung fürs Programmieren der Python-Auswerteroutinen maßgeblich zu den schönen Ergebnissen beigetragen. Du bist nicht nur „godlike", sondern deine Diplomarbeit ist jetzt dann auch bald abgeschlossen und du wirst voraussichtlich den Weg eines Dissertanten einschlagen. Daher wünsche ich dir viel Spaß und Erfolg mit den Catcher-Setup und weiß, dass die Experimente bei euch in guten Händen sind. Weiters möchte ich mich bei meinen Kolleginnen Elisabeth Gruber und Janine Schwestka bedanken.

Elisabeth, du hast die Späße und Kindereien von Florian und mir von jeher mit Humor genommen und viel Geduld uns gegenüber gezeigt. Sehr hilfreich waren auch deine Messungen mit dem AFM, welche auch zu unserer gemeinsamen Publikation geführt haben.

Du, Zwetschke, warst stets hilfsbereit und hast fast jedem ein Lächeln geschenkt ☺ . Auch habe ich den morgendlichen Kaffee und das Tratschen mit dir sehr genossen. Seit kurzem gibt es auch noch einen neuen Dissertant in der Runde, Georg Harrer. Du, Georg, hast in der kurzen Zeit, seit wir uns kennen, stets dafür gesorgt, dass wir nicht verhungern und uns mit Essen versorgt, egal wie lange die Schlange auch war. Du hast dich auch sehr schnell in der Arbeitsgruppe eingefunden und uns regelmäßig mit den neuesten Youtube-Videos versorgt. Weiters möchte ich noch allen anderen Arbeitsgruppenmitgliedern danken, welche ich aufgrund ihrer Vielzahl leider nicht alle erwähnen kann. Ihr alle zusammen habt dieses nette Umfeld geschaffen, in dem ich mich von jeher wohl gefühlt habe.

Als letztes Mitglied der Arbeitsgruppe möchte ich mich noch bei dem ehemaligen österreichischen Handballstar ☺ (siehe Wikipedia Artikel [108]) Florian Laggner bedanken. Flo, danke dafür, dass du mich vor $3^1/2$ Jahren auf die offene Dissertationsstelle aufmerksam gemacht hast. Gemeinsam mit Roland Bliem, Thomas Hausmaninger und Anna Galler haben wir vor mittlerweile schon fast 10 Jahren mit dem Studieren begonnen und zusammen die eine oder andere Hürde bewältigt. Unsere gemeinsame Zeit in der Arbeitsgruppe hat sehr viel Spaß gemacht und wir haben neben der Arbeit auch das eine oder andere Projekt gestartet. Das vermutlich neben unseren wissenschaftlichen Arbeiten größte Vermächtnis für das IAP ist unser Weihnachtsfeierfilm „The World of IAP Intelligent Awesome Physicists". Neben unserer Zeit als Arbeitskollegen haben wir auch privat vieles erlebt, wie zum Beispiel meinen Polterabend, den du als mein Trauzeuge organisiert hast, oder diverse gemeinsame Urlaube. Ich hoffe, dass wir auch in Zukunft im engen Kontakt bleiben und weitere lustige Abenteuer erleben dürfen. Mein Dank gilt auch meinen Kommilitonen Roli, Anna und Thomas. Wir haben in den ersten Semestern unzählige Physikbeispiele gemeinsam gelöst und uns tatsächlich alle eines Doktoratsstudiums als würdig erwiesen.

Zum Abschluss möchte ich noch dem Dank an meiner Familie Ausdruck verleihen. Liebe Eltern, danke dafür, dass ich fortdauernd mit eurer Unterstützung rechnen kann und ihr mir Halt gebt. Ich konnte mich stets frei entfalten, und ihr habt meine Entscheidung zu studieren gefördert und unterstützt.

Liebe Ingeborg, dir möchte ich ganz besonders danken, durch dich habe ich Wien besser kennengelernt, und es wurde dadurch und mit deiner Anwesenheit mit der Zeit zu meinem Zuhause. Du hast mich jetzt schon fast durch das ganze Studium begleitet und mich ausgehalten, wenn ich viel gearbeitet habe oder vor Prüfungen unausgeglichen war. Wenn ich mit dem Flo wieder einmal zu ausgiebig über die Uni gequatscht habe, hast du Nachsicht gezeigt. Du hast mich auch immer wieder auf den Boden der Realität zurückgeholt und wieder aufgebaut, wenn ich meine Motivation verloren habe. Eine ganz besondere Freude hast du mir nicht nur bereitet, als du zu meiner Frau sondern auch als du die Mutter von unserem wunderbaren Sohn Ferdinand wurdest. Auch bei dir, Ferdi, möchte ich mich herzlich bedanken. Du hast oft für den nötigen Ausgleich zur Arbeit an der Uni gesorgt und dafür, dass ich schon seit längerem keinen Wecker mehr brauche ☺ .

Bernhard Maximilian Berger

Wien, Österreich, März 2017

Bibliography

[1] IEA, 'World Energy Outlook 2014', *OECD Publishing* (2014)

[2] Iter Organization, 'Iter', (2017), URL `https://www.iter.org/`

[3] EUROfusion, 'EUROfusion', (2017), URL `www.euro-fusion.org`

[4] Romeiras F.J., 'Plasma Physics and Nuclear Fusion Research Edited by R. D. Gill. Academic Press, 1981. 688 pp. £27.60', *Journal of Plasma Physics*, **26**, 585 (2009), URL `http://dx.doi.org/10.1017/s0022377800010916`

[5] Kikuchi M., *Hydrogen Fusion: Light Nuclei and Theory of Fusion Reactions*, 15–32, Springer London, London (2011)

[6] de Laeter J.R., Böhlke J.K., Bièvre P.D., Hidaka H., Peiser H.S., Rosman K.J.R. and Taylor P.D.P., 'Atomic weights of the elements. Review 2000 (IUPAC Technical Report)', *Pure and Applied Chemistry*, **75**, 683 (2003), URL `http://dx.doi.org/10.1351/pac200375060683`

[7] Bosch H.S. and Hale G.M., 'Improved Formulas for Fusion Cross-Sections and Thermal Reactivities', *Nuclear Fusion*, **32**, 611 (1992), URL `http://dx.doi.org/10.1088/0029-5515/32/4/I07`

[8] Lawson J.D., 'Some Criteria for a Power Producing Thermonuclear Reactor', *Proceedings of the Physical Society of London Section B*, **70**, 6 (1957), URL `http://dx.doi.org/Doi10.1088/0370-1301/70/1/303`

[9] Miyamoto K., *Development of Fusion Research*, 259–267, Springer Berlin Heidelberg, Berlin, Heidelberg (2005)

[10] Clery D., 'Feature: Germany fires up bizarre new fusion reactor', *Science* (2015), URL `http://dx.doi.org/10.1126/science.aad4746`

[11] Pedersen T.S., Otte M., Lazerson S., Helander P., Bozhenkov S., Biedermann C., Klinger T., Wolf R.C., Bosch H.S. and the Wendelstein 7-X Team, 'Confirmation of the topology of the Wendelstein 7-X magnetic field to better than 1:100,000', *Nat Commun*, **7**, 13493 (2016), URL `http://dx.doi.org/10.1038/ncomms13493`

[12] 'Max-Planck-Institut für Plasmaphysik', (2017), URL `http://www.ipp.mpg.de/`

[13] Jacquinot J. and JET Team, 'Deuterium-tritium operation in magnetic confinement experiments: results and underlying physics', *Plasma Physics and Controlled Fusion*, **41**, A13 (1999), URL `http://dx.doi.org/Doi10.1088/0741-3335/41/3a/002`

[14] Maisonnier D., Campbell D., Cook I., Pace L.D., Giancarli L., Hayward J., Puma A.L., Medrano M., Norajitra P., Roccella M., Sardain P., Tran M.Q. and Ward D., 'Power plant conceptual studies in Europe', *Nuclear Fusion*, **47**, 1524 (2007), URL `http://dx.doi.org/10.1088/0029-5515/47/11/014`

[15] Roth J., Tsitrone E., Loarte A., Loarer T., Counsell G., Neu R., Philipps V., Brezinsek S., Lehnen M., Coad P., Grisolia C., Schmid K., Krieger K., Kallenbach A., Lipschultz B., Doerner R., Causey R., Alimov V., Shu W., Ogorodnikova O., Kirschner A., Federici G. and Kukushkin A., 'Recent analysis of key plasma wall interactions issues for ITER', *Journal of Nuclear Materials*, **390-391**, 1 (2009), URL `http://dx.doi.org/10.1016/j.jnucmat.2009.01.037`

[16] Federici G., Skinner C.H., Brooks J.N., Coad J.P., Grisolia C., Haasz A.A., Hassanein A., Philipps V., Pitcher C.S., Roth J., Wampler W.R. and Whyte D.G., 'Plasma-material interactions in current tokamaks and their implications for next step fusion reactors', *Nuclear Fusion*, **41**, 1967 (2001), URL `http://dx.doi.org/10.1088/0029-5515/41/12/218`

[17] Roth J., Tsitrone E., Loarer T., Philipps V., Brezinsek S., Loarte A., Counsell G.F., Doerner R.P., Schmid K., Ogorodnikova O.V. and Causey R.A., 'Tritium inventory in ITER plasma-facing materials and tritium removal procedures', *Plasma Physics and Controlled Fusion*, **50**, 103001 (2008), URL `http://dx.doi.org/10.1088/0741-3335/50/10/103001`

[18] Pitts R.A., 'Physics Basis and Design of the ITER Full Tungsten Divertor', *55th APS Meeting, Denver, CO, USA, paper WE1.00001* (2014)

[19] Brezinsek S., 'Plasma-surface interaction in the Be/W environment: Conclusions drawn from the JET-ILW for ITER', *Journal of Nuclear Materials*, **463**, 11 (2015), URL `http://dx.doi.org/10.1016/j.jnucmat.2014.12.007`

[20] Hirai T., Escourbiac F., Carpentier-Chouchana S., Durocher A., Fedosov A., Ferrand L., Jokinen T., Komarov V., Merola M., Mitteau R., Pitts R.A., Shu W., Sugihara M., Barabash V., Kuznetsov V., Riccardi B. and Suzuki S., 'ITER full tungsten divertor qualification program and progress', *Physica Scripta*, **T159**, 014006 (2014), URL `http://dx.doi.org/10.1088/0031-8949/2014/t159/014006`

[21] Merola M., Escourbiac F., Raffray A.R., Chappuis P., Hirai T. and Gicquel S., 'Engineering challenges and development of the ITER Blanket System and Divertor', *Fusion Engineering and Design*, **96-97**, 34 (2015), URL `http://dx.doi.org/10.1016/j.fusengdes.2015.06.045`

[22] Hirai T., Panayotis S., Barabash V., Amzallag C., Escourbiac F., Durocher A., Merola M., Linke J., Loewenhoff T., Pintsuk G., Wirtz M. and Uytdenhouwen I., 'Use of tungsten material for the ITER divertor', *Nuclear Materials and Energy* (2016), URL `http://dx.doi.org/10.1016/j.nme.2016.07.003`

[23] Raffray A.R. and Merola M., 'Overview of the design and R&D of the ITER blanket system', *Fusion Engineering and Design*, **87**, 769 (2012), URL `http://dx.doi.org/10.1016/j.fusengdes.2012.02.013`

[24] Pitts R.A., Carpentier S., Escourbiac F., Hirai T., Komarov V., Lisgo S., Kukushkin A.S., Loarte A., Merola M., Naik A.S., Mitteau R., Sugihara M., Bazylev B. and Stangeby P.C., 'A full tungsten divertor for ITER: Physics issues and design status', *Journal of Nuclear Materials*, **438**, S48 (2013), URL `http://dx.doi.org/10.1016/j.jnucmat.2013.01.008`

[25] Tobita K., Nishio S., Enoeda M., Kawashima H., Kurita G., Tanigawa H., Nakamura H., Honda M., Saito A., Sato S., Hayashi T., Asakura N., Sakurai S., Nishitani T., Ozeki T., Ando M., Ezato K., Hamamatsu K., Hirose T., Hoshino T., Ide S., Inoue T., Isono T., Liu C., Kakudate S., Kawamura Y., Mori S., Nakamichi M., Nishi H., Nozawa T., Ochiai K., Ogiwara H., Oyama N., Sakamoto K., Sakamoto Y., Seki Y., Shibama Y., Shimizu K., Suzuki S., Takahashi K., Tanigawa H., Tsuru D., Yamanishi T. and Yoshida T., 'Compact DEMO, SlimCS: design progress and issues', *Nuclear Fusion*, **49**, 075029 (2009), URL `http://dx.doi.org/10.1088/0029-5515/49/7/075029`

[26] Neu R., Kallenbach A., Sertoli M., Dux R., Fischer R., Fuchs J.C., Janzer A., Müller H.W., Potzel S., Pütterich T. and van Rooij G., 'Tungsten behaviour in radiatively cooled plasma discharges in ASDEX Upgrade', *Journal of Nuclear Materials*, **415**, S322 (2011), URL `http://dx.doi.org/10.1016/j.jnucmat.2010.09.036`

[27] Nakano T., Kubo H., Asakura N., Shimizu K., Kawashima H. and Higashijima S., 'Radiation process of carbon ions in JT-60U detached divertor plasmas', *Journal of Nuclear Materials*, **390-391**, 255 (2009), URL `http://dx.doi.org/10.1016/j.jnucmat.2009.01.085`

[28] Kallenbach A., Balden M., Dux R., Eich T., Giroud C., Huber A., Maddison G.P., Mayer M., McCormick K., Neu R., Petrie T.W., Putterich T., Rapp J., Reinke M.L., Schmid K., Schweinzer J., Wolfe S., ASDEX Upgrade Team, DIII-D Team, Alcator Team and JET-EFDA Contributors, 'Plasma surface interactions in impurity seeded plasmas', *Journal of Nuclear Materials*, **415**, S19 (2011), URL `http://dx.doi.org/10.1016/j.jnucmat.2010.11.105`

[29] Dux R., Bobkov V., Herrmann A., Janzer A., Kallenbach A., Neu R., Mayer M., Müller H.W., Pugno R., Pütterich T., Rohde V. and Sips A.C.C., 'Plasma-wall interaction and plasma behaviour in the non-boronised all tungsten ASDEX Upgrade', *Journal of Nuclear Materials*, **390-391**, 858 (2009), URL `http://dx.doi.org/10.1016/j.jnucmat.2009.01.225`

[30] Kallenbach A., Dux R., Fuchs J.C., Fischer R., Geiger B., Giannone L., Herrmann A., Lunt T., Mertens V., McDermott R., Neu R., Pütterich T., Rathgeber S., Rohde V., Schmid K., Schweinzer J. and Treutterer W., 'Divertor power load feedback with nitrogen seeding in ASDEX Upgrade', *Plasma Physics and Controlled Fusion*, **52**, 055002 (2010), URL `http://dx.doi.org/10.1088/0741-3335/52/5/055002`

[31] Dobes K., Naderer P., Lachaud N., Eisenmenger-Sittner C. and Aumayr F., 'Sputtering of tungsten by N+ and N2+ ions: investigations of molecular effects', *Physica Scripta*, **T145**, 014017 (2011), URL `http://dx.doi.org/10.1088/0031-8949/2011/t145/014017`

[32] Meisl G., Schmid K., Encke O., Höschen T., Gao L. and Linsmeier C., 'Implantation and erosion of nitrogen in tungsten', *New Journal of Physics*, **16**, 093018 (2014), URL `http://dx.doi.org/Artn09301810.1088/1367-2630/16/9/093018`

[33] Schmid K., Manhard A., Linsmeier C., Wiltner A., Schwarz-Selinger T., Jacob W. and Mandl S., 'Interaction of nitrogen plasmas with tungsten', *Nuclear Fusion*, **50**, 025006 (2010), URL `http://dx.doi.org/10.1088/0029-5515/50/2/025006`

[34] Bolt H., Barabash V., Federici G., Linke J., Loarte A., Roth J. and Sato K., 'Plasma facing and high heat flux materials - needs for ITER and beyond', *Journal of Nuclear Materials*, **307–311, Part 1**, 43 (2002), URL `http://dx.doi.org/10.1016/S0022-3115(02)01175-3`

[35] Maisonnier D., Cook I., Pierre S., Lorenzo B., Edgar B., Karin B., Luigi D.P., Robin F., Luciano G., Stephan H., Claudio N., Prachai N., Aldo P., Neill T. and David W., 'The European power plant conceptual study', *Fusion Engineering and Design*, **75-79**, 1173 (2005), URL `http://dx.doi.org/10.1016/j.fusengdes.2005.06.095`

[36] Lindau R., Moslang A., Rieth M., Klimiankou M., Materna-Morris E., Alamo A., Tavassoli A.A.F., Cayron C., Lancha A.M., Fernandez P., Baluc N., Schaublin R., Diegele E., Filacchioni G., Rensman J.W., van der Schaaf B., Lucon E. and Dietz W., 'Present development status of EUROFER and ODS-EUROFER for application in blanket concepts', *Fusion Engineering and Design*, **75-79**, 989 (2005), URL `http://dx.doi.org/10.1016/j.fusengdes.2005.06.186`

[37] Roth J., Sugiyama K., Alimov V., Höschen T., Baldwin M. and Doerner R., 'EUROFER as wall material: Reduced sputtering yields due to W surface enrichment', *Journal of Nuclear Materials*, **454**, 1 (2014), URL `http://dx.doi.org/10.1016/j.jnucmat.2014.07.042`

[38] Sugiyama K., Roth J., Alimov V.K., Schmid K., Balden M., Elgeti S., Koch F., Höschen T., Baldwin M.J., Doerner R.P., Maier H. and Jacob W., 'Erosion study of Fe-W binary mixed layer prepared as model system for RAFM steel', *Journal of Nuclear Materials*, **463**, 272 (2015), URL `http://dx.doi.org/10.1016/j.jnucmat.2014.11.044`

[39] Jacob W. and Roth J., *Chemical sputtering*, 329–400, Springer (2007)

[40] Horn A., Schenk A., Biener J., Winter B., Lutterloh C., Wittmann M. and Kuppers J., 'H-Atom Impact-Induced Chemical Erosion Reaction at C-H Film Surfaces', *Chemical Physics Letters*, **231**, 193 (1994), URL `http://dx.doi.org/10.1016/0009-2614(94)01233-4`

[41] Keim A., Rasul B., Endstrasser N., Scheier P., Märk T.D. and Herman Z., 'Interaction of small hydrocarbon ions and Ar+ with carbon-fibre-composite surfaces at room temperature', *International Journal of Mass Spectrometry*, **306**, 204 (2011), URL `http://dx.doi.org/10.1016/j.ijms.2010.11.002`

[42] Aumayr F. and Winter H., 'Potential sputtering', *Philos Trans A Math Phys Eng Sci*, **362**, 77 (2004), URL `http://dx.doi.org/10.1098/rsta.2003.1300`

[43] Schneider D.H.G. and Briere M.A., 'Investigations of the interactions of highest charge state ions with surfaces', *Physica Scripta*, **53**, 228 (1996), URL `http://dx.doi.org/10.1088/0031-8949/53/2/013`

[44] Aumayr F., Varga P. and Winter H.P., 'Potential sputtering: desorption from insulator surfaces by impact of slow multicharged ions', *International Journal of Mass Spectrometry*, **192**, 415 (1999), URL `http://dx.doi.org/10.1016/S1387-3806(99)00075-5`

[45] Hayderer G., Schmid M., Varga P., Winter H.P., Aumayr F., Wirtz L., Lemell C., Burgdorfer J., Hagg L. and Reinhold C.O., 'Threshold for potential sputtering of LiF', *Physical Review Letters*, **83**, 3948 (1999), URL `http://dx.doi.org/10.1103/PhysRevLett.83.3948`

[46] Hayderer G., Cernusca S., Schmid M., Varga P., Winter H., Aumayr F., Niemann D., Hoffmann V., Stolterfoht N., Lemell C., Wirtz L. and Burgdorfer J., 'Kinetically assisted potential sputtering of insulators by highly charged ions', *Phys Rev Lett*, **86**, 3530 (2001), URL `http://dx.doi.org/10.1103/PhysRevLett.86.3530`

[47] Pitts R.A., Coad J.P., Coster D.P., Federici G., Fundamenski W., Horacek J., Krieger K., Kukushkin A., Likonen J., Matthews G.F., Rubel M., Strachan J.D. and JET-EFDA Csontributors, 'Material erosion and migration in tokamaks', *Plasma Physics and Controlled Fusion*, **47**, B303 (2005), URL `http://dx.doi.org/10.1088/0741-3335/47/12b/s22`

[48] Sigmund P., 'Theory of Sputtering. I. Sputtering Yield of Amorphous and Polycrystalline Targets', *Physical Review*, **184**, 383 (1969), URL `http://dx.doi.org/10.1103/PhysRev.184.383`

[49] Eckstein W. and Preuss R., 'New fit formulae for the sputtering yield', *Journal of Nuclear Materials*, **320**, 209 (2003), URL `http://dx.doi.org/10.1016/S0022-3115(03)00192-2`

[50] Sigmund P., 'Recollections of fifty years with sputtering', *Thin Solid Films*, **520**, 6031 (2012), URL `http://dx.doi.org/10.1016/j.tsf.2012.06.003`

[51] Sigmund P., 'Six decades of atomic collisions in solids', *Nuclear Instruments and Methods in Physics Research Section B: Beam Interactions with Materials and Atoms* (2016), URL `http://dx.doi.org/10.1016/j.nimb.2016.12.004`

[52] Eckstein W., *The Binary Collision Model*, 4–32, Springer Berlin Heidelberg, Berlin, Heidelberg (1991)

[53] Dobes K., 'Erosion of Fusion Relevant Surfaces under Ion Impact', Dissertation, Technischen Universität Wien (2014)

[54] Yamamura Y., Itikawa Y. and Itoh N., 'Report IPPJ-AM-26', *Institute of Plasma Physics, Nagoya University* (1983)

[55] Küstner M., Eckstein W., Dose V. and Roth J., 'The influence of surface roughness on the angular dependence of the sputter yield', *Nuclear Instruments & Methods in Physics Research Section B-Beam Interactions with Materials and Atoms*, **145**, 320 (1998), URL `http://dx.doi.org/10.1016/S0168-583x(98)00399-1`

[56] Küstner M., Eckstein W., Hechtl E. and Roth J., 'Angular dependence of the sputtering yield of rough beryllium surfaces', *Journal of Nuclear Materials*, **265**, 22 (1999), URL `http://dx.doi.org/10.1016/S0022-3115(98)00648-5`

[57] Behrisch R. and Eckstein W., *Sputtering by Particle Bombardment*, volume 110 of *Topics in Applied Physics*, Springer Berlin Heidelberg (2007)

[58] Gnaser H., *Energy and angular distributions of sputtered species*, 231–328, Springer (2007)

[59] Ikuse K., Yoshimura S., Kiuchi M., Hine K. and Hamaguchi S., 'Measurement of Sticking Probability and Sputtering Yield of Au by Low-Energy Mass Selected Ion Beams with a Quartz Crystal Microbalance - art. no. 012016', *Journal of Physics: Conference Series*, **106**, 12016 (2008), URL `http://dx.doi.org/10.1088/1742-6596/106/1/012016`

[60] Bachmann L. and Shin J.J., 'Measurement of the Sticking Coefficients of Silver and Gold in an Ultrahigh Vacuum', *Journal of Applied Physics*, **37**, 242 (1966), URL `http://dx.doi.org/10.1063/1.1707818`

[61] Chapman G.E., Farmery B.W., Thompson M.W. and Wilson I.H., 'The energy distribution of sputtered atoms from gold', *Radiation Effects*, **13**, 121 (2006), URL `http://dx.doi.org/10.1080/00337577208231169`

[62] Berger B.M., Stadlmayr R., Meisl G., Čekada M., Eisenmenger-Sittner C., Schwarz-Selinger T. and Aumayr F., 'Transient effects during erosion of WN by deuterium ions studied with the quartz crystal microbalance technique', *Nuclear Instruments and Methods in Physics Research Section B: Beam Interactions with Materials and Atoms*, **382**, 82 (2016), URL `http://dx.doi.org/10.1016/j.nimb.2016.04.060`

[63] Berger B.M., Szabo P.S., Stadlmayr R. and Aumayr F., 'Sputtering measurements using a quartz crystal microbalance as a catcher', *Nuclear Instruments and Methods in Physics Research Section B: Beam Interactions with Materials and Atoms* (2016), URL `http://dx.doi.org/10.1016/j.nimb.2016.11.039`

[64] Hayderer G., Schmid M., Varga P., Winter H.P. and Aumayr F., 'A highly sensitive quartz-crystal microbalance for sputtering investigations in slow ion-surface collisions', *Review of Scientific Instruments*, **70**, 3696 (1999), URL `http://dx.doi.org/10.1063/1.1149979`

[65] Golczewski A., Dobes K., Wachter G., Schmid M. and Aumayr F., 'A quartz-crystal-microbalance technique to investigate ion-induced erosion of fusion relevant surfaces', *Nuclear Instruments & Methods in Physics Research Section B-Beam Interactions with Materials and Atoms*, **267**, 695 (2009), URL `http://dx.doi.org/10.1016/j.nimb.2008.10.088`

[66] Golczewski A., Kuzucan A., Schmid K., Roth J., Schmid M. and Aumayr F., 'Ion-induced erosion of tungsten surfaces studied by a sensitive quartz-crystal-microbalance technique', *Journal of Nuclear Materials*, **390-91**, 1102 (2009), URL `http://dx.doi.org/10.1016/j.jnucmat.2009.01.279`

[67] KVG Quartz Crystal Technology GmbH, 'Data Sheet for Quartz Crystal Resonators', (2006)

[68] Schmid M., 'Möglichkeiten und Grenzen der Schwingquarz-Schichtdickenmessung', Dissertation, Technischen Universität Wien (1989)

[69] Sauerbrey G., 'Verwendung von Schwingquarzen zur Wägung dünner Schichten und zur Mikrowägung', *Zeitschrift für Physik*, **155**, 206 (1959), URL http://dx.doi.org/10.1007/bf01337937

[70] Dobes K., Köppen M., Oberkofler M., Lungu C.P., Porosnicu C., Höschen T., Meisl G., Linsmeier C. and Aumayr F., 'Interaction of nitrogen ions with beryllium surfaces', *Nuclear Instruments & Methods in Physics Research Section B-Beam Interactions with Materials and Atoms*, **340**, 34 (2014), URL http://dx.doi.org/10.1016/j.nimb.2014.06.025

[71] Schmid M., Benes E., Burger W. and Kravchenko V., 'Motional capacitance of layered piezoelectric thickness-mode resonators', *IEEE Trans Ultrason Ferroelectr Freq Control*, **38**, 199 (1991), URL http://dx.doi.org/10.1109/58.79604

[72] Benes E., Groschl M., Burger W. and Schmid M., 'Sensors Based on Piezoelectric Resonators', *Sensors and Actuators a-Physical*, **48**, 1 (1995), URL http://dx.doi.org/10.1016/0924-4247(95)00846-2

[73] Cumpson P.J. and Seah M.P., 'The quartz crystal microbalance; radial/polar dependence of mass sensitivity both on and off the electrodes', *Measurement Science and Technology*, **1**, 544 (1990), URL http://dx.doi.org/10.1088/0957-0233/1/7/002

[74] Radović I.B., *private communication* (2015)

[75] Galutschek E., 'Development of a 14.5 GHz All-Permanent Magnet Multicharged ECR Ion Source for Remote Operation', Dissertation, Technischen Universität Wien (2005)

[76] Galutschek E., Trassl R., Salzborn E., Aumayr F. and Winter H.P., 'Compact 14.5 GHz all-permanent magnet ECRIS for experiments with slow multicharged ions', *Journal of Physics: Conference Series*, **58**, 395 (2007), URL http://dx.doi.org/10.1088/1742-6596/58/1/090

[77] Biersack J.P. and Eckstein W., 'Sputtering studies with the Monte Carlo Program TRIM.SP', *Applied Physics A*, **34**, 73 (1984), URL http://dx.doi.org/10.1007/bf00614759

[78] Möller W. and Eckstein W., 'Tridyn - a Trim Simulation Code Including Dynamic Composition Changes', *Nuclear Instruments & Methods in Physics Research Section B-Beam Interactions with Materials and Atoms*, **2**, 814 (1984), URL http://dx.doi.org/10.1016/0168-583x(84)90321-5

[79] Möller W., Eckstein W. and Biersack J.P., 'Tridyn - Binary Collision Simulation of Atomic-Collisions and Dynamic Composition Changes in Solids', *Computer Physics Communications*, **51**, 355 (1988), URL http://dx.doi.org/10.1016/0010-4655(88)90148-8

[80] Ziegler J.F., Ziegler M.D. and Biersack J.P., 'SRIM - The stopping and range of ions in matter (2010)', *Nuclear Instruments & Methods in Physics Research Section B-Beam Interactions with Materials and Atoms*, **268**, 1818 (2010), URL http://dx.doi.org/10.1016/j.nimb.2010.02.091

[81] Mutzke A., Schneider R., Eckstein W. and Dohmen R., 'SDTrimSP Version 5.00', Technical report, Max-Planck-Institut für Plasmaphysik (2011)

[82] Hofsäss H., Zhang K. and Mutzke A., 'Simulation of ion beam sputtering with SDTrimSP, TRIDYN and SRIM', *Applied Surface Science*, **310**, 134 (2014), URL `http://dx.doi.org/10.1016/j.apsusc.2014.03.152`

[83] Wilson W.D., Haggmark L.G. and Biersack J.P., 'Calculations of nuclear stopping, ranges, and straggling in the low-energy region', *Physical Review B*, **15**, 2458 (1977), URL `http://dx.doi.org/10.1103/PhysRevB.15.2458`

[84] Company C.R., *CRC Handbook of Chemistry and Physics*, Crc Handbook of Chemistry and Physics, CRC Press (1997)

[85] Allouche A., 'First principles calculations on nitrogen reactivity on tungsten surfaces', *J Phys Condens Matter*, **28**, 015001 (2016), URL `http://dx.doi.org/10.1088/0953-8984/28/1/015001`

[86] Oberkofler M., Alegre D., Aumayr F., Brezinsek S., Dittmar T., Dobes K., Douai D., Drenik A., Koppen M., Kruezi U., Linsmeier C., Lungu C.P., Meisl G., Mozetic M., Porosnicu C., Rohde V., Romanelli S.G., ASDEX Upgrade Team and JET EFDA Contributors, 'Plasma-wall interactions with nitrogen seeding in all-metal fusion devices: Formation of nitrides and ammonia', *Fusion Engineering and Design*, **98-99**, 1371 (2015), URL `http://dx.doi.org/10.1016/j.fusengdes.2015.01.044`

[87] Liu J., Yu D., Ruan F., Xue Y. and Wang W., 'Note: a real-time beam current density meter', *Rev Sci Instrum*, **84**, 036107 (2013), URL `http://dx.doi.org/10.1063/1.4795400`

[88] Thompson M.W., 'II. The energy spectrum of ejected atoms during the high energy sputtering of gold', *Philosophical Magazine*, **18**, 377 (1967), URL `http://dx.doi.org/10.1080/14786436808227358`

[89] Berger B.M., Stadlmayr R., Blöch D., Gruber E., Sugiyama K., Schwarz-Selinger T. and Aumayr F., 'Erosion of Fe-W model system under normal and oblige D ion irradiation', *Nuclear Materials and Energy* (2017), URL `http://dx.doi.org/10.1016/j.nme.2017.03.030`

[90] Neu R., Balden M., Bobkov V., Dux R., Gruber O., Herrmann A., Kallenbach A., Kaufmann M., Maggi C.F., Maier H., Müller H.W., Pütterich T., Pugno R., Rohde V., Sips A.C.C., Stober J., Suttrop W., Angioni C., Atanasiu C.V., Becker W., Behler K., Behringer K., Bergmann A., Bertoncelli T., Bilato R., Bottino A., Brambilla M., Braun F., Buhler A., Chankin A., Conway G., Coster D.P., de Marné P., Dietrich S., Dimova K., Drube R., Eich T., Engelhardt K., Fahrbach H.U., Fantz U., Fattorini L., Fink J., Fischer R., Flaws A., Franzen P., Fuchs J.C., Gál K., Muñoz M.G., Gemisic-Adamov M., Giannone L., Gori S., da Graca S., Greuner H., Gude A., Günter S., Haas G., Harhausen J., Heinemann B., Hicks N., Hobirk J., Holtum D., Hopf C., Horton L., Huart M., Igochine V., Kálvin S., Kardaun O., Kick M., Kocsis G., Kollotzek H., Konz C., Krieger K., Kurki-Suonio T., Kurzan B., Lackner K., Lang P.T., Lauber P., Laux M., Likonen J., Liu L., Lohs A., Mank K., Manini A., Manso M.E., Maraschek M., Martin P., Martin Y., Mayer M., McCarthy P., McCormick K., Meister H., Meo F., Merkel P., Merkel R., Mertens V., Merz F., Meyer H., Mlynek M., Monaco F., Murmann H., Neu G., Neuhauser J., Nold B., Noterdaeme J.M., Pautasso G., Pereverzev G., Poli E., Püschel M., Raupp G., Reich M., Reiter B., Ribeiro T., Riedl R., Roth J., Rott M., Ryter F., Sandmann W., Santos J., Sassenberg K., Scarabosio A., Schall G., Schirmer J., Schmid A., Schneider W., Schramm G., Schrittwieser R., Schustereder W., Schweinzer J., Schweizer S., Scott B., Seidel

U., Serra F., Sertoli M., Sigalov A., Silva A., Speth E., Stäbler A., Steuer K.H., Strumberger E., Tardini G., Tichmann C., Treutterer W., Tröster C., Urso L., Vainonen-Ahlgren E., Varela P., Vermare L., Wagner D., Wischmeier M., Wolfrum E., Würsching E., Yadikin D., Yu Q., Zasche D., Zehetbauer T., Zilker M. and Zohm H., 'Plasma wall interaction and its implication in an all tungsten divertor tokamak', *Plasma Physics and Controlled Fusion*, **49**, B59 (2007), URL `http://dx.doi.org/10.1088/0741-3335/49/12b/S04`

[91] Philipps V., Mertens P., Matthews G.F., Maier H. and JET-EFDA Contributors, 'Overview of the JET ITER-like Wall Project', *Fusion Engineering and Design*, **85**, 1581 (2010), URL `http://dx.doi.org/10.1016/j.fusengdes.2010.04.048`

[92] Gao L., Jacob W., Meisl G., Schwarz-Selinger T., Hoschen T., von Toussaint U. and Durbeck T., 'Interaction of deuterium plasma with sputter-deposited tungsten nitride films', *Nuclear Fusion*, **56**, 016004 (2016), URL `http://dx.doi.org/10.1088/0029-5515/56/1/016004`

[93] Sugiyama K., Schmid K. and Jacob W., 'Sputtering of iron, chromium and tungsten by energetic deuterium ion bombardment', *Nuclear Materials and Energy*, **8**, 1 (2016), URL `http://dx.doi.org/10.1016/j.nme.2016.05.016`

[94] Winters H.F. and Sigmund P., 'Sputtering of chemisorbed gas (nitrogen on tungsten) by low-energy ions', *Journal of Applied Physics*, **45**, 4760 (1974), URL `http://dx.doi.org/10.1063/1.1663131`

[95] Lam N.Q., 'Ion bombardment effects on the near-surface composition during sputter profiling', *Surface and Interface Analysis*, **12**, 65 (1988), URL `http://dx.doi.org/10.1002/sia.740120202`

[96] Oberkofler M., *private communication* (2016)

[97] Necas D. and Klapetek P., 'Gwyddion: an open-source software for SPM data analysis', *Central European Journal of Physics*, **10**, 181 (2012), URL `http://dx.doi.org/10.2478/s11534-011-0096-2`

[98] Škereň T., Temst K., Vandervorst W. and Vantomme A., 'Ion-induced roughening and ripple formation on polycrystalline metallic films', *New Journal of Physics*, **15**, 093047 (2013), URL `http://dx.doi.org/10.1088/1367-2630/15/9/093047`

[99] Mishra P. and Ghose D., 'Formation of nanoripples in Al films duringO2+sputtering', *Physical Review B*, **74** (2006), URL `http://dx.doi.org/10.1103/PhysRevB.74.155427`

[100] Karmakar P. and Ghose D., 'Ion beam sputtering induced ripple formation in thin metal films', *Surface Science*, **554**, L101 (2004), URL `http://dx.doi.org/10.1016/j.susc.2004.02.020`

[101] Ghose D., 'Ion beam sputtering induced nanostructuring of polycrystalline metal films', *J Phys Condens Matter*, **21**, 224001 (2009), URL `http://dx.doi.org/10.1088/0953-8984/21/22/224001`

[102] Keller A. and Facsko S., 'Ion-Induced Nanoscale Ripple Patterns on Si Surfaces: Theory and Experiment', *Materials*, **3**, 4811 (2010), URL `http://dx.doi.org/10.3390/ma3104811`

[103] Mutzke A., Schneider R. and Bandelow G., 'SDTrimSP-2D: Simulation of Particles Bombarding on a Two Dimensional Target-Version 2.0', (2013)

[104] von Toussaint U. and Mutzke A., 'Fluence dependent changes of erosion yields and surface morphology of the iron-tungsten model system: SDTrimSP-2D simulation studies', *Nuclear Materials and Energy* (2016), URL `http://dx.doi.org/10.1016/j.nme.2016.09.005`

[105] Dobes K., Smejkal V., Schafer T. and Aumayr F., 'Interaction between seeding gas ions and nitrogen saturated tungsten surfaces', *International Journal of Mass Spectrometry*, **365**, 64 (2014), URL `http://dx.doi.org/10.1016/j.ijms.2013.11.015`

[106] Hayderer G., Cernusca S., Hoffmann V., Niemann D., Stolterfoht N., Schmid M., Varga P., Winter H.P. and Aumayr F., 'Sputtering of Au and Al2O3 surfaces by slow highly charged ions', *Nuclear Instruments & Methods in Physics Research Section B-Beam Interactions with Materials and Atoms*, **182**, 143 (2001), URL `http://dx.doi.org/10.1016/S0168-583x(01)00668-1`

[107] Oliva-Florio A., Baragiola R.A., Jakas M.M., Alonso E.V. and Ferron J., 'Noble-gas ion sputtering yield of gold and copper: Dependence on the energy and angle of incidence of the projectiles', *Phys Rev B Condens Matter*, **35**, 2198 (1987), URL `http://dx.doi.org/10.1103/PhysRevB.35.2198`

[108] Wikipedia, 'Florian Laggner', (2017), URL `https://de.wikipedia.org/wiki/Florian_Laggner`

Curriculum Vitae

Personal Data

NAME:	Bernhard Maximilian BERGER
PLACE AND DATE OF BIRTH:	Vöcklabruck, Austria | 1. Feb. 1988
ADDRESS:	Barichgasse 5a/2, 1030, Wien, Austira
EMAIL:	berger@iap.tuwien.ac.at

Education

2013 - 2017   **PhD in Technical Physics** at the Institute of Applied Physics, TU Wien, (Vienna)
PhD Thesis:" *Laboratory work on plasma-wall-interaction processes relevant for fusion experiments*"
Supervisor: Univ. Prof. Dr. Friedrich AUMAYR

2011 - 2013   **Master studies in Physical Energy and Measurement Engineering**, TU Wien, (Vienna)
Master Thesis:" *Experimental realization of velocity selection by means of spin resonance of very cold neutrons (VCN)*"
Supervisor: Prof. Dr. Gerald BADUREK and Ass. Prof. Dr. Erwin JERICHA
(Graduated with distinction)

2007 - 2011   **Bachelor studies in Technical Physics**, TU Wien, (Vienna)
Bachelor Thesis:" *Faserbeton mit Naturfasern*"
Supervisor: Prof. Dr. Elmar TSCHEGG

2002 - 2007   **Higher Technical Education Institute**, HTL Vöcklabruck, mechanical engineering (Upper Austria)

1998 - 2002   **Secondary School**, Hauptschule Vöcklabruck (Upper Austria)

1994 - 1998   **Elementary School**, Volksschule Vöcklabruck (Upper Austria)